Application of the seeding approach to nucleation in a CaO-SiO_2 system for obtaining the parameters for the Classical Nucleation Theory

A valuable numerical tool for screening potential glassmaking recipes

W. J. B. Nederstigt

Delft University of Technology

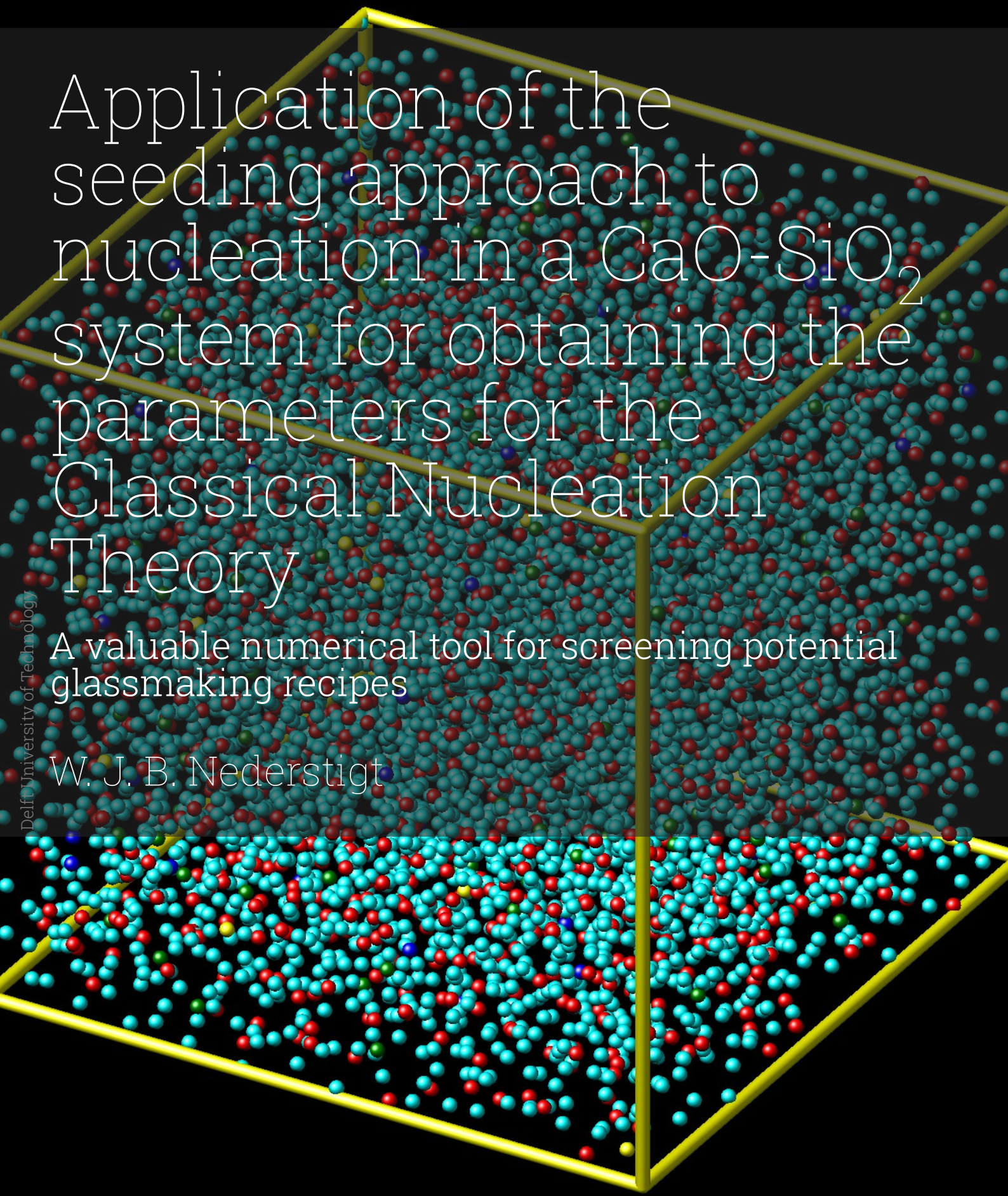

TU Delft

Application of the seeding approach to nucleation in a $CaO\text{-}SiO_2$ system for obtaining the parameters for the Classical Nucleation Theory

A valuable numerical tool for screening potential glassmaking recipes

by

W. J. B. Nederstigt

to obtain the degree of Master of Science

at the Delft University of Technology,

to be defended publicly on Friday June 30, 2023 at 10:00 AM.

Student number:	4204344	
Project duration:	May 16, 2022 – June 30, 2023	
Thesis committee:	Dr. ir. M. J. M. Hermans,	TU Delft, supervisor
	Dr. ir. F. A. Veer,	TU Delft, supervisor
	Dr. M. H. F. Sluiter,	TU Delft
	Ir. J. A. Minkels,	Maana Electric, daily supervisor

Ruud Hendrikx at the Department of Materials Science and Engineering of the Delft University of Technology is acknowledged for the X-ray analysis

TU Delft

Abstract

For the use of screening potential glassmaking recipes the seeding method has been applied to a Molecular Dynamics simulated CaO-SiO_2 system in order to attain the parameters for the Classical Nucleation Theory and construct a Time-Temperature-Transformation (TTT) diagram. Using this TTT diagram, the non-crystallisation temperature and the critical cooling rate of the material was determined, two quantities important for the prevention of crystallisation during the glassmaking process. The implementation of the seeding method on the CaO-SiO_2 system involved creating a novel local bond order based detection method for distinguishing the crystalline structure of Wollastonite-1A from the glass melt. Regrettably this method had less than desirable precision which resulted in results for the nucleation rate that can only be used qualitatively. In contrast the results for the crystalline growth rate can be used quantitatively, while the resulting TTT diagram again can only be used qualitatively.

Contents

Nomenclature

Acronyms

BO Bridging Oxygen

DIT diffuse interface theory

DSC differential scanning calorimetry

GFA glass forming ability

MD Molecular Dynamics

NBO Non Bridging Oxygen

STM Scanning Tunneling Microscopy

TTT Time-Temperature-Transformation

VFT Vogel-Fulcher-Tammann

XRD X-Ray Diffraction

1

Introduction

The company Maana Electric has as a goal to power the world with electricity. To attain this goal, they aim to produce a manufacturing plant that creates solar panels out of nothing but desert sands. A section of this manufacturing plant will be creating glass panels out of the desert sands to encapsulate and protect the manufactured solar cells. There are still challenges in tweaking the optimal composition for this glass, especially when starting with a diverse feedstock such as desert sands. One important factor in this process is the selection of a location which can supply a feedstock that can be beneficiated into a composition that is feasible for glass production. Information on the full range of compositions where glassmaking is feasible is highly valuable to the company, and this work aims to explore one of the steps towards that goal.

Especially of concern to the company is the temperature at which the molten glass will, over time, crystallize. Another attribute of interest to the company is the minimum cooling rate of the glass in order to prevent crystallisation. Therefore the goal of this work is to answer the following research question:

> **What is the non-crystallisation temperature and minimum non-crystallisation cooling rate for an arbitrary CaO-SiO_2 glass composition.**

There are many roads which lead towards this goal. The most apparent route might be to gather a large amount of samples and subject them to a variety of process conditions in order to discover which conditions are beneficial or detrimental to the goal of manufacturing satisfactory glass panels. However in order to gain insight into the process conditions a large number of variables must be controlled for. Additionally, only access to equipment that is only available at a handful of research institutions in the world might be enough to achieve a full understanding of the conditions of the glass during the glassmaking process. An alternative is the numerical simulation of the glass, which would allow for intimate insight into the material during the glassmaking process which is not possible during physical experiments in ovens at temperatures in excess of 1400 °C.

A large concern of the glassmaker for the making of glass from desert sands is the unintended crystallisation of the glass during the production process. This can be remedied by a thorough understanding of the crystallisation behavior of the material. Recent works have shown a promising technique to gain an understanding of the crystallisation behavior of glassforming materials. This technique is designated as the method of 'seeding' and it involves the insertion of a nucleus of a crystal in a Molecular Dynamics simulation of a glass melt, after which the nucleus is observed for growth or shrinkage. The results of this observation, in addition to other information from the simulation, allows the experimenter

to construct a Time-Temperature-Transformation diagram using the Classical Nucleation Theory. It has previously been applied to select metallic glasses in order to determine their minimum cooling rate, however it should be possible to apply to the varied compositions of desert sands.

Therefore this work aims to apply the seeding method towards a select composition of desert sand in order to determine if the method is feasible for use in predicting the boundary processing conditions which would prevent crystallisation of the produced glass panels. If it were to be validated it would be a valuable tool in the selection of promising locations for the production of solar panels out of desert sands for the company Maana Electric.

This work will start with giving background information into glass itself, what it is and what happens during crystallisation. Additionally, the current state of the art is explored for methods that result into the solution of the research question. The implementation of the seeding method chosen for this work is described, after which the results of this method are presented. These results are discussed, after which the work is concluded.

2

Literature review

In this section, first the background on glass and its composition dependent properties during the liquid phase will be discussed. Then the nucleation behavior will be discussed where the theories behind glass nucleation and crystal growth will be introduced. The theory behind the creation of Time-Temperature-Transformation diagrams will be discussed, as they are helpful for calculating the required cooling rate and non-crystallisation temperature. Lastly the use of computer simulations for the calculation of the parameters to describe the nucleation behavior and crystal growth will be discussed.

2.1. What is glass?

According to the literature, glass is; *an amorphous solid completely lacking in long range, periodic atomic structure, and exhibiting a region of glass transformation behavior* [1]. And while this is a thorough definition, a more exhaustive explanation is in order. Therefore a start is made by discussing the structure of glasses, since while it is true that there is no long range order to be found in glasses, there is a definite short range order to be defined [2]. This will also lead to knowledge on what materials are able to be formed into glasses, and which cannot. In addition to that, the glass transformation behavior will be discussed. This behavior occurs during the transformation of liquid to solid, and of course from solid to liquid. However for the stated application only the liquid to solid glass transformation is of interest, which will be discussed.

2.1.1. The structure of glasses

The scientific community has spent over 300 years studying glass and it uses. The early efforts focused on the uses of glass [3], but the accepted start of glass science [4] began in the 1880s at the hands of Otto Schott working for the Carl Zeis' Optische Werkstaette [5]. This lead to the work of Zachariasen where the atomic arrangement of glasses was proposed, which is a good step in the investigation of what glass is.

In Zachariasen's work, it was attempted to explain the results of the X-Ray Diffraction (XRD) studies of glasses. The leading theory at the time was that the structure of glass must be microcrystalline in order to produce the result of the XRD studies [6], as it cannot be classified as simply frozen liquid [7]. It was pointed out by Zachariasen that there were some flaws with this theory, and an alternative theory was introduced [8], which was subsequently corroborated by other studies [9, 10].

The theory of Zachariasen consists of the assertion that vitreous silica consist of a three-dimensional

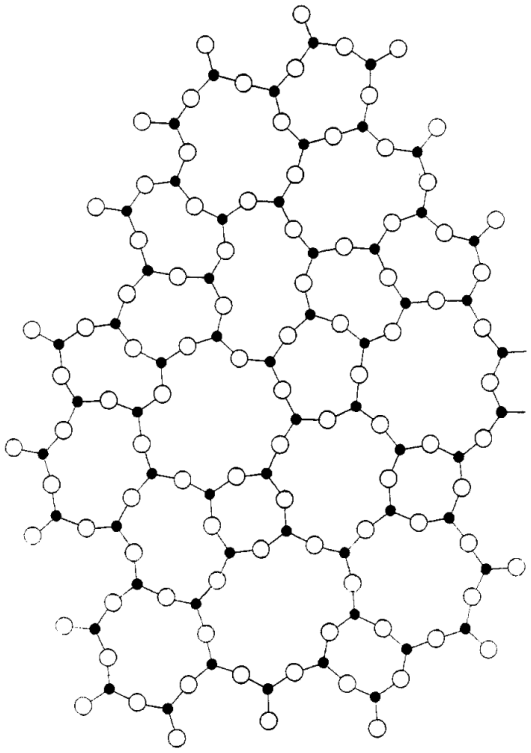

(a) An illustration of the structure of the two-dimensional glass network of the compound A_2O_3, analogous to the three-dimensional structure of vitreous silica. Reproduced from [8]

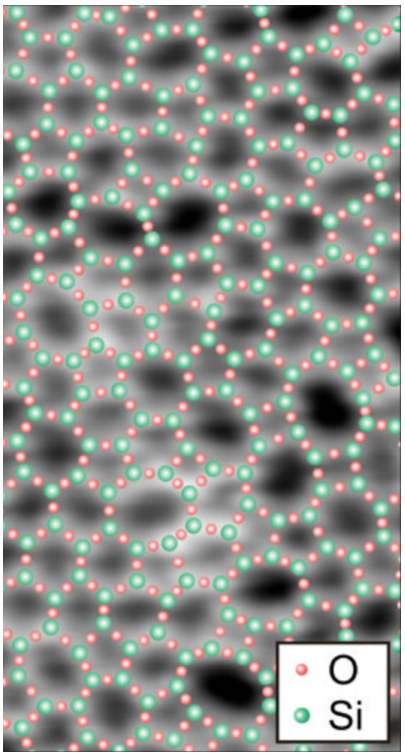

(b) An STM image of a two-dimensional layer of a thin vitreous bilayer silica film. Adapted from [12]

Figure 2.1: Two-dimensional representations of the atomic structure of vitreous silica

random network of oxygen tetrahedra surrounding silicon atoms, where the oxygen tetrahedra share the corners in such a way that the oxygen atoms neighbour two silicon atoms [8]. As there is no long range order in vitreous silica, the bond angles between the oxygen tetrahedra vary. It is difficult to properly portray the three-dimensional structure of vitreous silica, so Zachariasen opted to portray an analogous two-dimensional structure to support his theory, as seen in figure 2.1a. This structure has been validated [11], and in figure 2.1b a Scanning Tunneling Microscopy (STM) image with the superimposed atomic structure can be seen.

The three-dimensional structure has also been validated [13], and it is found that in three dimensions the rings as seen in figures 2.1a and 2.1b also occur, however they do not share the same plane and are thus rotated with respect to each other. The three dimensional structure of rings of different sizes can be seen in figure 2.2. The relative abundance of the different size rings has been investigated through the use of Molecular Dynamics (MD) simulations [14], and the results can be viewed in table 2.1 for vitreous silica (a-SiO_2), as well as for quartz and cristobalite, which are crystalline polymorphs of silica.

Table 2.1: Statistics of n-fold rings per $Si(O_{1/2})_4$ tetrahedron in a-SiO_2 at 310 K. Adapted from [14]

Ring size (n)	3	4	5	6	7	8	9	10
α- and β-cristobalite				6				
α- and β-quartz				4		2		
a-SiO_2	0.06	0.52	1.40	2.11	1.18	0.40	0.06	0.01

Not all glasses consist of only SiO_2, the widely used soda-lime glass has additions of Na_2O and CaO, for example. So this theory has to be expanded upon. It was theorized by Zachariasen that these additional ions interrupt the network, and then sit in the cavity left by the opened rings, as can be seen

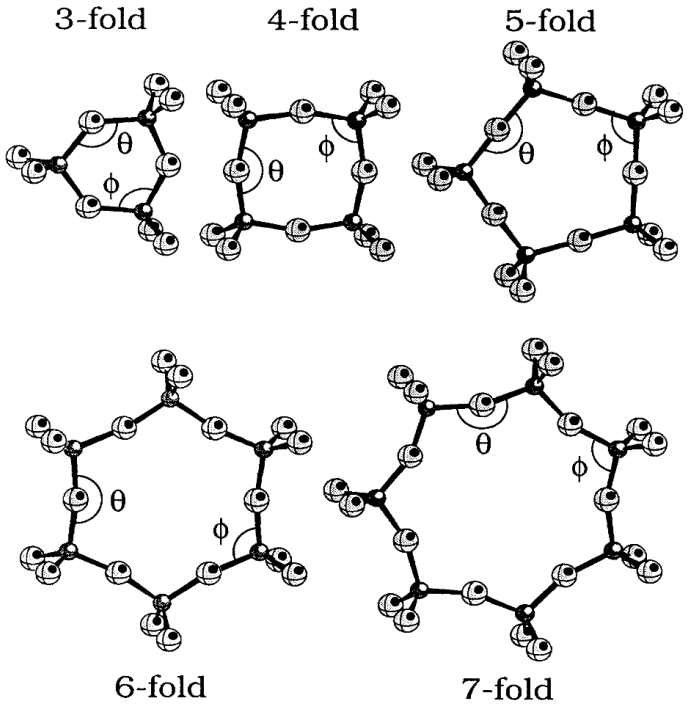

Figure 2.2: The three-dimensional structure of the rings found in vitreous silica. Reproduced from [14]

in figure 2.3. This theory has subsequently been validated [15, 16].

Around the time that Zachariasen and Warren published their research, a rival theory was developed by Lebedev to explain the results of the XRD studies. This theory stated that glass had to consist out of small crystalline phases, connected by an amorphous structure that was described as deformed crystals [18]. The size of these crystalline phases was later to be determined to be on the scale of 0.8-1.5 nm [19]. This theory is the opposite of that of Zachariasen in terms of whether the structure is ordered or unordered. There have been other theories on the structure of glasses, that lie in between ordered such as Lebedev's theory, and the unordered theory of Zachariasen. Recent work suggest that both models are not an universal predictor of the structure of glass, and the conclusion is that in reality the structure lies somewhere in between, depending on thermal history of the glass. It also concludes that the vitreous state is in a thermodynamic metastable state, which means that the previous theories on glass structure that assume an equilibrium state do not fully describe all glass structures [20].

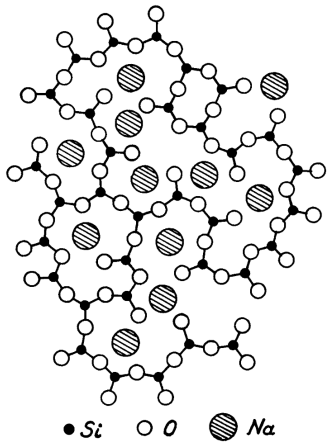

Figure 2.3: A two-dimensional representation of the arrangement of ions in a sodium silicate glass. Reproduced from [17]

Not only the structure of glass was of import to early glass researchers, the role of different components and additives was also of interest, as only specific combinations of ions will form a glass network. Zachariasen and Warren explained this using Goldschmidt's work on geochemistry [21], which focused on the ionic field strength with relation to the radii of the differing ionic species. This led to the declaration of the distinct categories of network formers, intermediate oxides, and network modifiers, which specified the location where the ions would settle in a glass network. Network formers are named as such since they form the glass network. These are atomic species like Si and B, and will sit in the center of the oxygen tetrahedra. Network modifiers would open up the oxygen bridges between SiO_4 tetrahedra, and sit in the resulting cavity in the network. Na and Ca are species

Table 2.2: An overview of the field strength of different species of cations. Reproduced from [23]

Element	Valency	Ionic radius (for coord. no. 6)	The most common coordination no.	Interval between the oxide ions	Field strength of the O^2-ions across the interval	
	Z	r(Å)	$Z = 6$	a(Å)	Z/a^2	
K	1	1·33	8	2·77	0·13	
Na	1	0·98	6	2·30	0·19	
Li	1	0·78	6	2·10	0·23	
Ba	2	1·43	8	2·86	0·24	Network
Pb	2	1·32	8	2·74	0·27	modifier
Sr	2	1·27	8	2·69	0·28	$Z/a^2 \approx$ 0·1–0·4
Ca	2	1·06	8	2·48	0·33	
Mn	2	0·91	6	2·23	0·40	
Fe	2	0·83	6	2·15	0·43	
Mn	2	0·83	4	2·03	0·49	
Mg	2	0·78	6	2·10	0·45	
			4	1·96	0·53	
Zr	4	0·87	8	2·28	0·77	
Be	2	0·34	4	1·53	0·86	Intermediate
Fe	3	0·67	6	1·99	0·76	oxides
			4	1·88	0·85	$Z/a^2 \approx$ 0·5–1·0
Al	3	0·57	6	1·89	0·84	
			4	1·77	0·96	
Ti	4	0·64	6	1·96	1·04	
B	3	0·20	4	1·50	1·34	Network
			3	1·36	1·63	formers
Si	4	0·39	4	1·60	1·57	$Z/a^2 \approx$ 1·4–2·0
P	5	0·34	4	1·55	2·1	

that are classified as such. Intermediate oxides such as Al could end up in both positions, depending on the concentration of the ions, but these cannot form a glass on their own.

There were some flaws with the sole focus on ionic radii, and the later work of Dietzel improved on this classification [22]. Dietzel introduced the notion of ionic field strength with relation to the distance between the anions in glasses, which was a better predictor of the role of these ionic species in the formation of glasses than the method used by Goldschmidt and Zachariasen. The formula used by Dietzel to calculate the ionic field strength with relation to the distance between anions is the following:

$$F = \frac{Z}{a^2} \tag{2.1}$$

,where Z is the valency of the ion, a is the interval between the anions, most commonly oxygen, in ångström (Å), and F is thus the ionic field strength in $Å^{-2}$. It has been found that the field strength of network modifiers lie in the range of (0.1 - 0.4 $Å^{-2}$), the field strength of intermediate ions lie in the range of (0.5 - 1.0 $Å^{-2}$), and the field strength of network formers lie in the range of (1.4 - 2.0 $Å^{-2}$). An overview of the field strength of different species of cations can be found in table 2.2.

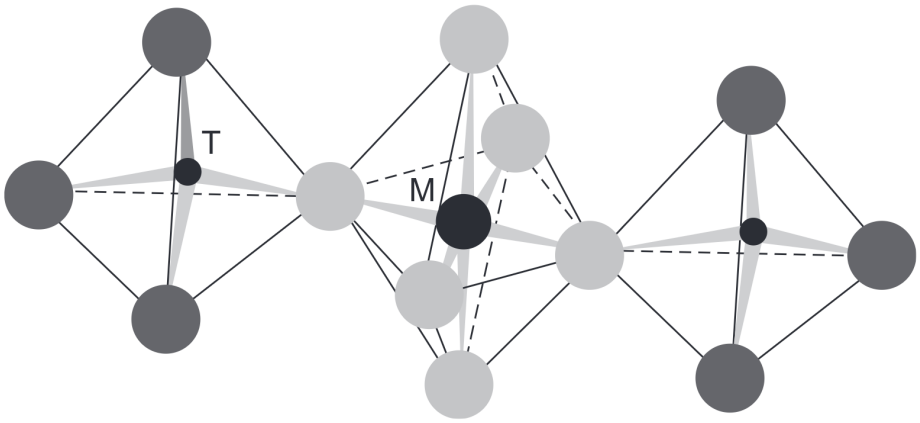

Figure 2.4: A schematic overview of the atomic structure of glass with network modifiers. Shown are the network formers (T), a network modifying ion (M), and the binding oxygen ions in dark grey, and the non binding oxygen ions in light grey. Reproduced from [24]

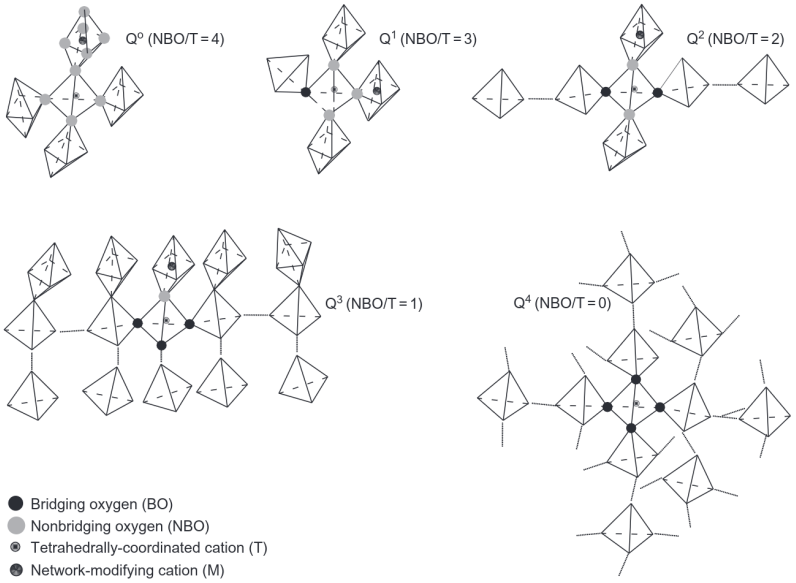

Figure 2.5: A schematic representation of the connection between SiO_4 tetrahedra in materials with of Q_n structural units. The small dotted lines represent the continuation of this structure ad infinitum. Reproduced from [24]

As stated previously, the ions that act as network modifiers will open up the oxygen bridges between the SiO_4 tetrahedra. Where previously that SiO_4 tetrahedron would be connected to four other SiO_4 tetrahedra through the four oxygen ions acting as a bridge, if a network modifying ion is situated next to a corner of the SiO_4 tetrahedron then that oxygen ion does not bridge tetrahedra and we can classify them as Non Bridging Oxygen (NBO). Conversely, oxygen ions that do bridge SiO_4 tetrahedra can be classified as Bridging Oxygen (BO). A schematic representation of this can be seen in figure 2.4. A helpful quantity to visualize the amount of NBO per SiO_4 tetrahedron is the measure of Q_n, where Q_0 signifies zero NBO per SiO_4 tetrahedron, while Q_4 signifies four NBO per SiO_4 tetrahedron [25]. This measure of Q_n was introduced since it is a good predictor of certain process properties such as the viscosity. A schematic representation of the structure of materials with different Q-species can be seen in figure 2.5.

2.1.2. Glass transformation behavior

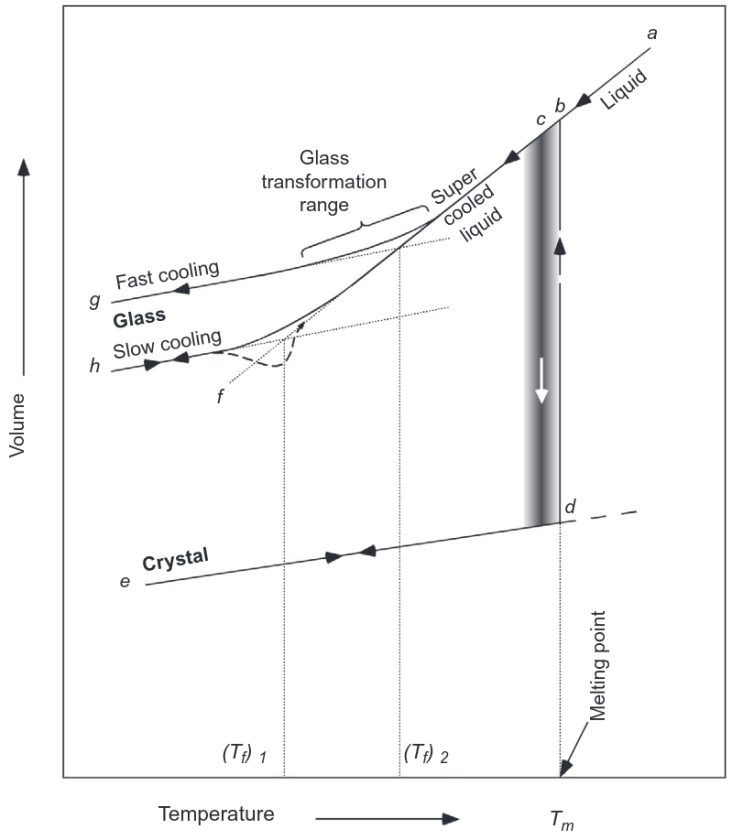

Figure 2.6: The volume-temperature diagram for a glass-forming liquid. Reproduced from [26]

While this structure can be confused to be classified as supercooled liquids, there are some material characteristics that sets this structure apart from supercooled liquids. This is mainly the temperature dependence of the volume of the material, which can be seen in figure 2.6. This places the material in their own category, namely glass.

What has been found is that the material does not have a discontinuity below the melting point in the volume-temperature relation, as is common for other materials which crystallize during solidification. Instead the line representing the volume/temperature relation continues below the melting point b following the same relation as in the liquid, after which the volume/temperature relation gradually curves off in order to end up parallel to the volume/temperature relation as seen in the solidified crystal.

The region in which the volume/temperature relation curves off of the line abf in figure 2.6 and becomes parallel to the line de of the crystal is called the glass transformation range. The intersection between the liquid relation abf and the line through g and parallel to ed is defined as the glass transformation temperature, which is used to define the onset of the glass transformation.

The begin of the glass transformation range is also dependent on the speed in which the material is cooled. A slower cooling rate allows for the material to conform to a more energetically favourable structure before being kinetically limited, resulting in a higher density material. This thus means that the glass transformation range and the glass transition temperature is dependent on the cooling rate [26]. This energetically favourable structure could also be a crystalline structure, making this of interest for the research question as the crystallisation temperature is thus dependent on the cooling rate, which presents challenges with the experimental determination of the crystallisation temperature.

2.2. Crystallisation behavior

The goal of the glassmaker is to turn the raw ingredients into glass. This glass is required for the application to be transparent in the range of the silicon photovoltaic cell, and thus any crystalline structures in the glass must smaller than around 300nm in order to be transparent in this range. This is since electromagnetic radiation will diffract at the grain boundaries of the crystal if the grain size of the crystal is larger than the wavelength of the light, which would decrease the transmittance of the glass. This means that in order to attain a glass panel transparent in the relevant range, the processing steps must be aimed at preventing the crystalline structures from nucleating and growing.

In this section, it will be discussed how to achieve this. First the step of nucleation will be discussed, after which the physics of crystal growth are explored. Together these two concepts determine the conditions under which crystalline structures will form in the material. Next the behavior of nucleation and crystal growth is explored. Additionally phase diagrams will be discussed, which give a graphical representation of the regions of temperature/composition where crystalline structures will form. Together these represent the static thermodynamic concepts behind the growth of crystalline structures, however kinetics are also an important part in the formation and growth of these structures.

A major factor in the kinetics of the formation and growth of crystalline structures is the viscosity of the glass. This viscosity determines in part how fast ions can move inside of the glass during the formation of these structures, and thus directly influences the growth rate of these structures. While other materials have a viscosity that is linearly dependent on the temperature, this is not the case with glasses. This non-linear dependence on temperature of the viscosity will be investigated next.

This temperature dependence of the viscosity of the glass, together with the thermodynamics of the creation and growth of crystalline structures, result in the concept of glass forming ability (GFA), which specifies how easily a glass is formed out of a glass melt. There are different ways to quantify this, but recent approaches use the critical cooling rate, calculated from the Time-Temperature-Transformation (TTT) diagram of the glass [27]. Attention will be given to this TTT diagram, what it is and how it is calculated, as it is a major help in the determination of the GFA of the glass melt.

Lastly the effect of the variation of the composition on these processing properties is explored, in particular the impact of compositional variation around the composition of the CaO rich deserts sand that is the subject of this review. This exploration will be done through the lens of the atomic structure, which can explain the change in viscosity, as well as the differing thermodynamics of nucleation and crystal growth of these varied compositions.

2.2.1. Nucleation and crystal growth

The process of devitrification starts with nucleation, after which this seed of a crystal can grow, depending on the conditions. The classical nucleation theory, which is most commonly used to describe the process of nucleation, states that nucleation and crystal growth are two distinct processes. As such they will be discussed separately, however they together determine the final volume fraction of crystalline structures in a glass after a specific heat treatment. Most texts regard a crystalline volume fraction of 10^{-6} as the border between glasses and glass ceramics, as that is the limit of most diagnostic equipment [1, 26].

Nucleation is in part a thermodynamic process. The change from a disordered state to an ordered state is driven by the ordered state having a lower Gibbs free energy. Simultaneously this change creates an interface layer between the crystal and the surrounding material, which is associated with a higher Gibbs free energy. These two terms together determine the Gibbs free energy of the nucleation process, or the work required to create a nucleus out of the liquid. The work necessary to create a nucleus of a certain size is the following [1, 26],

$$W = \frac{4}{3}\pi r^3 \Delta G_x + 4\pi r^2 \sigma, \tag{2.2}$$

where ΔG_x is the term for the per volume change in free energy between a melt and a crystal, sometimes called the "free energy of crystallisation", σ is the per unit area surface energy of the interface, and r is the radius of a spherical nucleus. The free energy of crystallisation ΔG_x is defined as negative, thus releasing energy and making the first term negative, while the second term is positive due to the melt-crystal interfacial free energy σ costing energy and thus being positive. These two terms oppose another, with the second, per area, term being dominant at small values of r, and the first, volumetric, term being dominant at large values of r. This can be seen in figure 2.7. In this figure the positive line for the $4\pi r^2\sigma$ term, the negative line for the $\frac{4}{3}\pi r^3 \Delta G_x$ term, and the combination of both can be seen. This combination has a peak at $r = r^*$, corresponding to the work of $W = W^*$. A nucleus of this size can both grow and shrink in size in order to lower its free energy, and thus a nucleus with this size has a 50% chance of becoming stable, with nuclei of a larger size being stable, and nuclei of a smaller size being unstable.

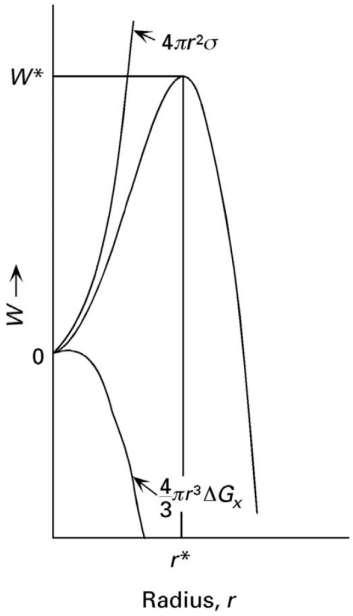

Figure 2.7: Change in free energy of a spherical nucleus as a function of radius. Reproduced from [26]

The work W^* required to create a nucleus of a critical size r^* from a glass melt can be seen as the activation energy to create a stable nucleus. The energy to surpass this barrier is gained from the thermal energy of the melt, and thus it is a stochastic process to form a nucleus. This means that the rate of nucleus formation is dependent on the temperature of the melt, where at lower temperatures the activation energy is less likely to be surpassed than at higher temperatures.

In order to calculate the formula for W^*, which is alternatively designated as ΔG^* in some publications, the value for r^* is calculated by differentiating equation 2.2 with respect to the nucleus radius, and subsequently equalizing this to 0. This gives:

$$r^* = \frac{2\sigma}{|\Delta G_x|}, \tag{2.3}$$

which when inserted into equation 2.2 gives:

$$W^* \,(= \Delta G^*) = \frac{16\pi\sigma^3}{3\,|\Delta G_x|^2} = \frac{4}{3}\pi\sigma r^{*2}. \tag{2.4}$$

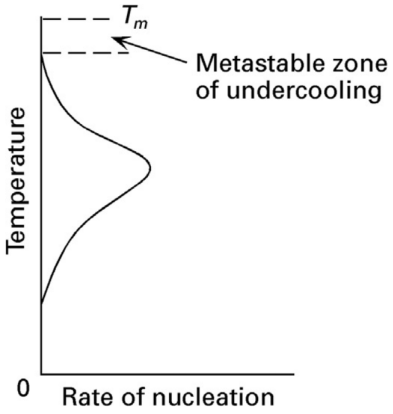

Figure 2.8: The rate of nucleation depending on the temperature. Reproduced from [26]

Do note that this activation energy W^* is defined for nucleation in the bulk material, also called homogeneous nucleation. Nucleation at a foreign surface, for example the container walls or impurities in the bulk, will result in a lowered melt-crystal interfacial free energy and thus a lower W^*. This is called heterogeneous nucleation, and the magnitude of this is dependent on the contact angle between the liquid, the crystal, and the substrate θ, as defined by equation 2.5 [26]:

$$W^*_{hetero} = W^*_{homo} * \left[(1 - \cos\theta)^2(2 + \cos\theta)/4\right]. \tag{2.5}$$

The magnitude of the activation energy W^* is also dependent on the temperature, with the dependence of the component ΔG_x being [1, 26]:

$$\Delta G_x = \frac{\Delta T \Delta H_f}{T_m},$$

with $\Delta T = T - T_m$ being is the temperature below the melting point T_m, otherwise called the amount of undercooling, and ΔH_f representing the heat of fusion. This means that $\Delta G_x = 0$ at $T = T_m$, and the value of ΔG_x only increases linearly with ΔT. Thus the activation energy W^* is very high for small values of ΔT, resulting in a region just below the melting temperature where there is no nucleus formation despite the high temperature.

This results in a nucleation rate which is low for temperatures close to the melting temperatures, and which is also low for low temperatures, which will result in the skewed bell curve as seen in figure 2.8. The rate of nucleation I can be expressed in the following formula [1, 26]:

$$I = n\nu \exp\left[-\left(\frac{N_a}{RT}\right)\left(\frac{16\pi\sigma^3}{3\Delta H_f^2}\right)\left(\frac{T_m}{\Delta T}\right)^2\right] \exp\left[\frac{\Delta E_D}{RT}\right], \tag{2.6}$$

where n is the number of atoms per unit volume, ν is the atomic vibration frequency, N_a is Avogadro's number, R is the gas constant, and ΔE_D is the activation energy for an atom to cross the liquid-nucleus barrier. Or alternatively the nucleation rate can be expressed as following [28]:

$$I = p_0 \nu n \exp\left[-\left(\frac{W^*}{k_B T}\right)\right], \tag{2.7}$$

where p_0 is the probability of capturing an atom at the surface of the nucleus.

After a nucleus of stable size has been formed, the process of crystal growth can take place. As this process is the growth of the crystal layers by atomic deposition, one important factor in the rate of crystal growth is the rate at which the atoms can cross the liquid-crystal interface layer. At this interface there is again an activation energy $\Delta E^{'}$ which has to be surpassed in order for the atom to cross this boundary. This is represented in figure 2.9, where the interfacial activation energy $\Delta E^{'}$ in relation to the free energy of crystallisation ΔG_x can be seen. This interfacial activation energy $\Delta E^{'}$ resembles the interfacial activation energy ΔE_D that was used in the calculation of the nucleation rate in equation 2.6, but due to differences in the size of the nucleus and thus the shape of the interface layer these two activation energies are different.

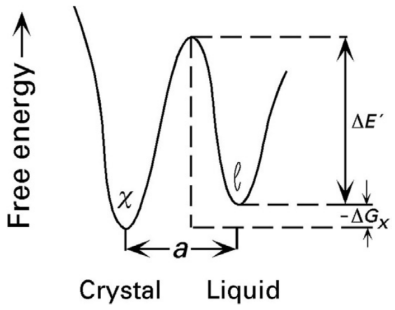

Figure 2.9: The free energy between a liquid and a crystal. Reproduced from [26]

The crystal growth rate has been derived to amount to the following equation [1, 26]:

$$u = a\nu \exp\left(-\frac{\Delta E^{'}}{RT}\right)\left[1 - \exp\left(\frac{\Delta G_x}{RT}\right)\right], \tag{2.8}$$

where a is the distance between the two positions. It was theorised [29] that the mechanisms controlling the activation energy for the growth of the crystal must be the same as those controlling viscous flow, which gives the following formula, where D is the diffusion coefficient:

$$u = \frac{D}{a}\left[1 - \exp\left(\frac{\Delta G_x}{RT}\right)\right]. \tag{2.9}$$

This can be related to the viscosity η by assuming the Stokes-Einstein relation $D = RT/3N\pi a\eta$ and assuming the average jump distance a to be roughly equivalent to the atomic diameter, which results in:

$$u = \frac{fRT}{3N_a\pi a^2\eta}\left[1 - \exp\left(\frac{\Delta G_x}{RT}\right)\right], \tag{2.10}$$

where f is the fraction of the surface where crystal growth sites are available.

When these equations with regards to the temperature are evaluated, it can be seen, as was the case with the nucleation rate, that close to the melting temperature ΔG_x is small, leading to a small growth rate of u. Again, at low temperatures the growth rate of u will also be small due to the low viscosity and the corresponding diffusion coefficient. Plotting this on a graph, together with the nucleation rate, the graph as shown in figure 2.10 is created. Here it can be seen that the peaks of the nucleation rate I and the crystal growth rate u do not coincide, and as the nucleation of a crystal must precede the growth of that crystal, the area of the shaded section thus is an important measure in the capability of this liquid to form a glass upon cooling. A smaller area of overlap signifies a higher ease of glass formation, since crystal formation is stunted.

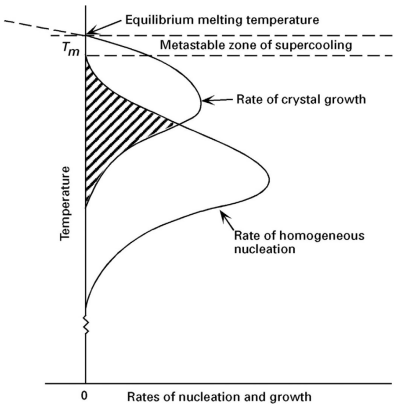

Figure 2.10: Variation of the crystal growth rate, u, and nucleation rate, I, with temperature, T. Reproduced from [26]

This concludes the description of the classical nucleation theory, however over the years since its inception several other theories were proposed which either expanded on the classical nucleation theory, or aimed to replace it. Of these different theories, the diffuse interface theory (DIT) has been found to be a better predictor for the CaO-SiO_2 glass-forming liquids than the classical nucleation theory [30, 31]. This theory regards the interface between the liquid and the crystal nucleus not as a sharp discontinuity, but as diffuse. This results in the interfacial free energy being dependant on the temperature, as opposed to a constant value as assumed in the classical nucleation theory. Otherwise the DIT is equivalent to the classical nucleation theory.

2.2.2. Phase diagram

A result of the thermodynamic considerations of nucleation and crystal growth is the phase diagram. For a chosen composition there are distinct temperature ranges where a specific crystalline structure, or phase, has the lowest free energy, and thus is most thermodynamically favourable to form. The temperatures and the specific phases change when the composition is varied, and this can be plotted in a phase diagram such as can be seen in figure 2.11. As the goal of glassmaking is to prevent the growth of crystalline structures, phase diagrams are of limited use for the glassmaker. However the line separating the liquid phase from the crystalline phases, often called the liquidus line, is of use for determining the temperature of the onset of crystallisation in the process of glass formation.

In figure 2.11 the phase diagram for the binary $CaO - SiO_2$ system is shown. One can see that the eutectic line signifying the border between the liquid phase, designated by the letter L in the diagram, and the crystalline phases is heavily dependant on the composition. That is, the temperature above which the glass in equilibrium contains purely liquid material varies significantly with the composition. It ranges from above 2600 °C at its upper limit to around 1436 °C at 63 mass % SiO_2. This variance is quite large, and thus for the production of glass this is a fairly important property to take into account, as together with the viscosity this plays a large part in the GFA of the mixtures.

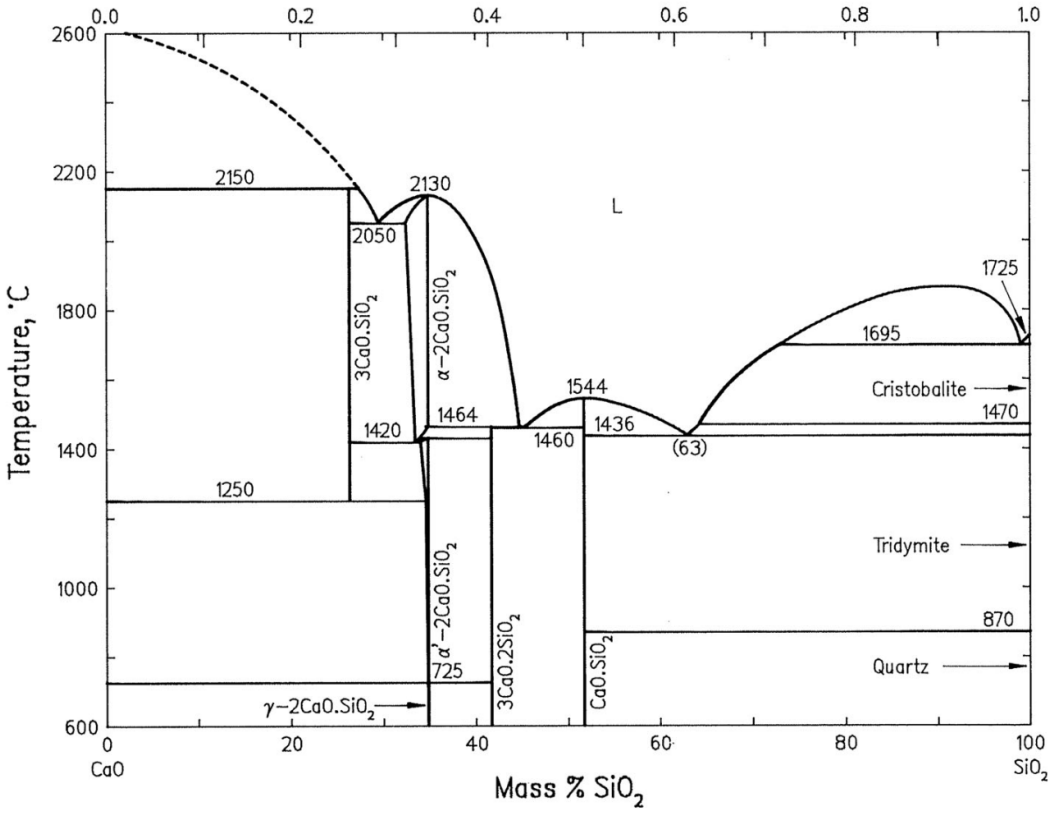

Figure 2.11: The phase diagram for the binary $CaO - SiO_2$ system. Reproduced from [32]

2.2.3. Viscosity curves

The viscosity is one of the terms in equation 2.10, which describes the crystal growth rate in terms of temperature, viscosity, and the heat of fusion. As the viscosity is also dependent on the temperature, it is of importance to have an accurate description of the temperature dependance of the viscosity. Other liquid materials such as lead and mercury have a viscosity that can be accurately described as being exponentially dependent on the temperature such as in equation 2.11 [33, 34]. Glass melts can, for a limited temperature range, be accurately described by an Arrhenius equation that is quite similar to equation 2.11, namely equation 2.12 [1, 35–37]. A better fit to the entire viscosity range is equation 2.13, which is a modification of equation 2.12 and is essentially identical to equation 2.11 [1, 38–41].

$$\eta = A \exp\left(\frac{B}{T-C}\right) \tag{2.11}$$

$$\eta = \eta_0 \exp\left(\frac{H_\eta}{RT}\right) \tag{2.12}$$

$$\eta = \eta_0 \exp\left(\frac{B}{T-T_0}\right) \tag{2.13}$$

One problem with the Vogel-Fulcher-Tammann (VFT) equation, which is what equation 2.13 is named, is that it is not accurate in the low temperature regions where T approaches T_0. In this region the viscosity is overestimated, leading to higher viscosity values. This is of particular detriment to the glassmaker if this region coincides with the glass transformation temperature, which would result in the rate of crystallisation to be underestimated when using this equation for the viscosity of glass melts.

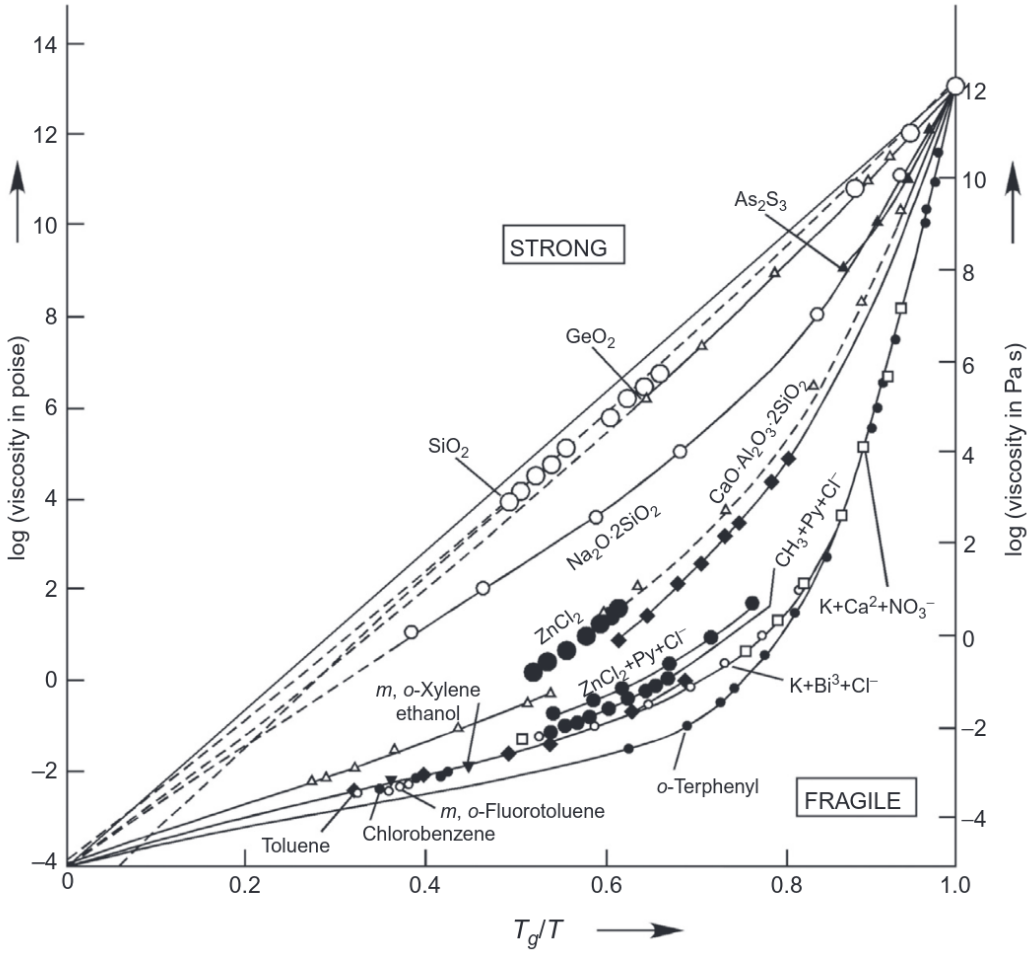

Figure 2.12: An Angell plot, where the viscosity of several glass-forming liquids is displayed against the inverted dimensionless temperature. Reproduced from [46]

To combat this discrepancy at the lower temperatures, there have been a number of alternative equations proposed for calculating the viscosity of glass melts. These are the Avramov-Milchev equation (equation 2.14) [42], Adam and Gibbs equation (equation 2.15) [43], and the Mauro-Yue-Ellison-Gupta-Allan equation (equation 2.16) [44].

$$\log \eta = \log \eta_\infty + \left(\frac{\tau}{T}\right)^\alpha \tag{2.14}$$

$$\log \eta(T) = \log \eta_\infty + \frac{B}{TS_c(T)} \tag{2.15}$$

$$\log \eta(T) = \log \eta_\infty + \frac{K}{T} \exp\left(\frac{C}{T}\right) \tag{2.16}$$

These equations all perform better than the VFT equation in the lower temperature range [44], but fortunately the research describing the viscosity of the composition of a glass melt from CaO rich desert sands result in a T_0 which is far outside of the glass transformation temperature [45], so the VFT equation can be used for this application without being detrimental to the results.

One extremely useful way of visualizing the viscosity is through an Angell plot. In this plot, the dimensionless inverse temperature (T_g/T, where T_g is the glass transition temperature) is plot against the logarithm of the viscosity, as can be seen in figure 2.12. In the plot a material which follows Arrhenius behavior in the temperature dependency of the viscosity, so equation 2.12 or equation 2.13 with the variable T_0 which is close to 0, will exhibit a straight line from $T_g/T = 0$ to $T_g/T = 1$. Alternatively, a material which follows a temperature dependence of the viscosity which would more align with equation 2.13 with a high value of T_0 would exhibit a line which is highly curved [46].

Of particular interest to the glassmaker is the slope of the viscosity curve at the glass transition temperature, so at $T_g/T = 1$. The slope at this point is called the fragility index of the glass, and materials which have a low slope and show an Arrhenius-like temperature dependence are called strong glasses, while glasses which exhibit a strong non-Arrhenius temperature dependence of the viscosity, and thus a high slope at the glass transition temperature, are defined as fragile glasses. The fragility index is defined in equation 2.17, where m is the fragility index, and T_g is the glass transition temperature [46].

$$m \equiv \left.\frac{\delta \log \eta}{\delta \left(T_g/T\right)}\right|_{T=T_g} \tag{2.17}$$

The fragility index, which again is defined as the slope at the glass transition temperature, is a signifier of how fast the viscosity decreases while cooling a glass melt through the glass transition temperature. A higher fragility index signifies a higher rate of change in the viscosity around the glass transition temperature, which results in a narrower temperature range of the glass transition. This in turn means that the glass melt has a lower critical cooling rate, which makes it have a larger GFA.

2.2.4. Glass forming ability/ TTT diagram

As equation 2.6 represents the nucleation rate, and equation 2.10 represents the crystal growth rate, they can be combined to calculate the volume fraction of liquid that is transformed into crystalline structures. This can be calculated using equation 2.18 [47–49], and filling this equation in for different temperatures and a set volume fraction will result in equation 2.19 [50] and a graph that signifies the isothermal heat treatment time to transform a set volume fraction of the melt into crystalline structures.

$$X = \frac{V_X}{V_0} = 1 - \exp\left(-\frac{\pi}{3} I u^3 t^4\right) \approx \frac{\pi}{3} I u^3 t^4 \tag{2.18}$$

$$t = \left(-\frac{3 \ln\left(1 - X\right)}{\pi I u^3}\right)^{1/4} \tag{2.19}$$

This is also known as a Time-Temperature-Transformation (TTT) diagram, an example of which can be seen in figure 2.13. In this TTT diagram, we can see that near the melting temperature of the material, the time required to form a crystal is essentially infinite. This is due to the lack of thermodynamic driving force, which is true for both I and u, as was discussed in section 2.2.1. The same is the case for lower temperatures, where the lack of thermal energy decelerates both the rates of nucleation and crystal growth, and thus also increases the time required to form a crystal. This means that there is a temperature at which the time required to form a crystal is at a minimum, in figure 2.13 it can be seen that this temperature is around 1140 K, and this maximum is commonly called the nose of the graph. For the purpose of glassmaking it is prudent to pass this temperature range expediently in order to prevent excessive crystallisation.

The shape of the TTT diagram is also one of the indicators of the GFA, which specifies how easily a glass can be created out of the melt. There are numerous criteria that are used to determine the GFA,

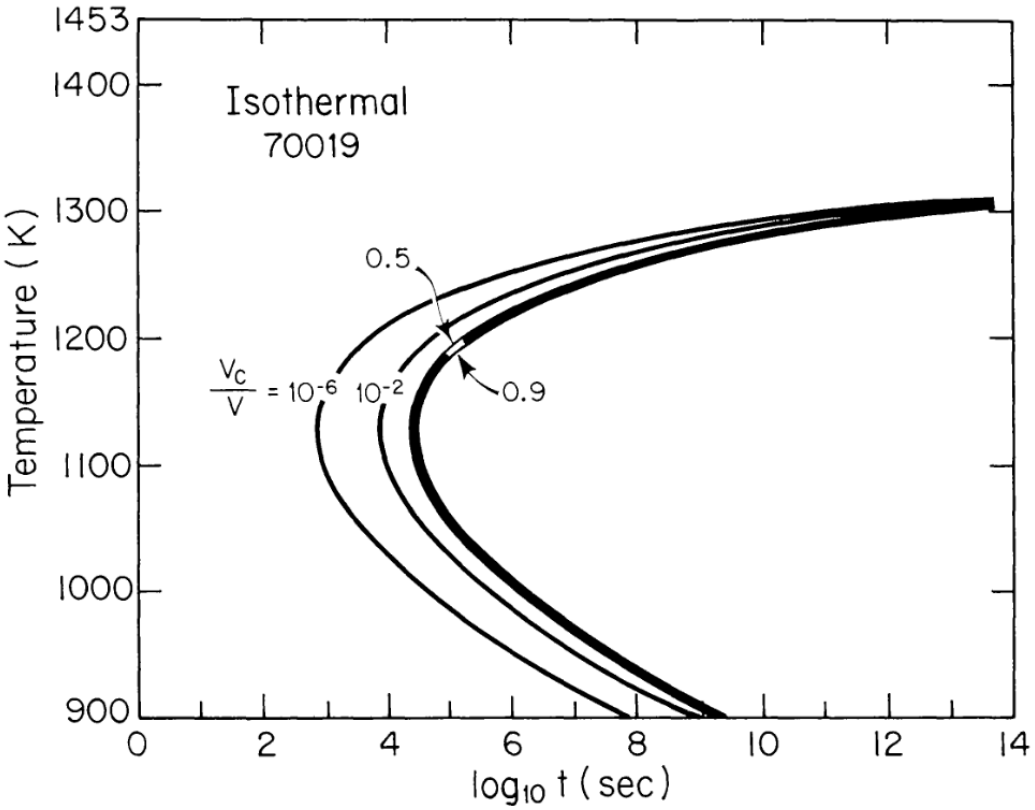

Figure 2.13: TTT curves of lunar soil, NASA apollo 17 sample 70019, with curves representing crystalline volume fractions ranging from 10^{-6} to 0.9 shown. Reproduced from [51]

these include the critical cooling rate, the glass transition temperature, and the fragility index of the glass melt [27]. One of these criteria, the critical cooling rate, can be calculated using the TTT diagram. This can be done by using equation 2.20, where R_c is the critical cooling rate, T_m is the melting temperature at which crystallisation starts, and T_n is the temperature of the 'nose' of the diagram, where the time t_n to reach the graph is at a minimum, as can be seen in figure 2.14 [1, 26, 52].

$$R_c \approx \frac{T_m - T_n}{t_n} \tag{2.20}$$

This TTT diagram is thus extremely helpful in determining a heat treatment of the glass melt that will result in a glass with an acceptable volume fraction of crystalline structures. And as the research question of this review amounts to discovering the relation of the time spend at a specific temperature and the volume fraction of crystalline structures in the glass, a TTT diagram of a melt with the composition as selected by the company Maana Electric is exactly what will help with answering that question. The various methods to create such a TTT diagram will be discussed in section 2.3.

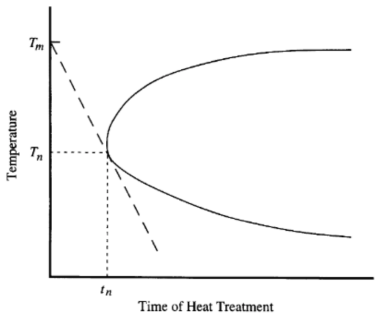

Figure 2.14: A schematic TTT diagram, pictured with the line following the critical cooling rate. Reproduced from [1]

2.3. Determination of TTT diagrams

Ever since the TTT diagram was created by Davenport and Bain in 1930 [53], it has been an extremely useful tool for the designing of heat treatments for all kinds of applications [54, 55]. In the case of glass, it is less about designing the ratio of different phases in the resulting material, but more about preventing those crystalline phases from forming in the first place. Nevertheless, those crystalline phases still form, and in order to design a heat treatment for the production of glasses a TTT diagram is an helpful tool to ensure the crystalline structures remain at an acceptable size.

There are several ways to construct a TTT diagram. The first way that will be discussed is through experimental methods where a TTT diagram is constructed by using the data gained through experiments. Then a more theoretical method is discussed, where the classical nucleation theory is used to predict the nucleation behavior of the glass melt, which will result in a TTT diagram. How the parameters for that theory are obtained also varies. Lastly insight will be given into previous work on the creation of TTT diagrams or comparable tools for glass melt compositions that resemble the composition of the CaO containing desert sands that this review focuses on.

2.3.1. Data gathering for the creation and validation of TTT diagrams

In general, the data necessary to calculate a TTT diagram can be gathered using experiments. These experiments amount to heat treating a material for a specified time at a specified temperature, after which the volume fraction of the different phases is determined using XRD analysis, or for metals even optical microscopy could be used after etching [53]. Subsequently that data can be plot in a TTT graph, and the data points with the same volume fraction can be connected to create a line representing the time at different temperatures to attain that volume fraction, an example of which can be seen in figure 2.15. This data can also be used to validate and rectify a TTT prediction such as those made using the classical nucleation theory and its derivatives.

This heat treatment was originally done for metals by suspending the samples in a bath of molten salts which was kept at a specific temperature, in order to get an uniform heat treatment [53]. Unfortunately, this method is not possible with glasses, as they are liquid in the range where crystalline structures grow and would therefore mix with the molten salts. A way to get around this for samples that you also wish to heat treat under pressure is to put samples of material in a capsule made of a material that is nonreactive with the glass melt, such as gold-palladium. This capsule is welded closed and inserted in a material with a good enough thermal conduction to ensure an uniform temperature during the heat treatment, after which it is pressurised and heated [56]. Recently, a method was developed for use in metallic glasses, called the containerless electrostatic levitation processing technique, where spheres of metallic material is levitated in a vacuum, which allows a heat treatment to be applied [57–59]. However as the CaO containing desert sands are not metallic, this method is not suitable for the determination of its TTT diagram.

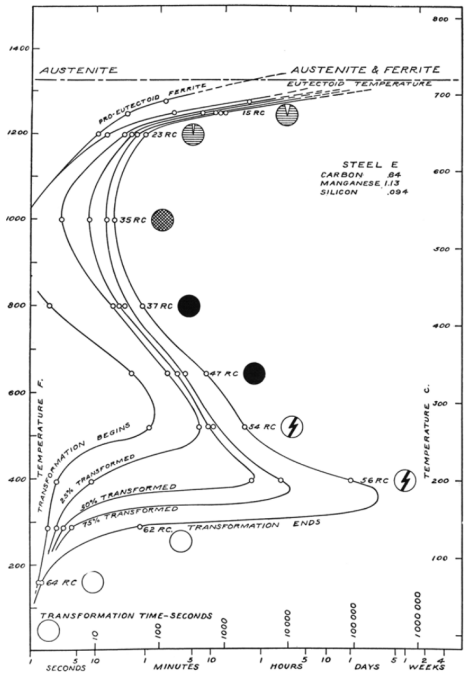

Figure 2.15: Time–temperature-transformation (TTT) diagram for steel, signifying five lines of different percentages of transformation, with the circles representing different crystal compositions. Reproduced from [53]

Another method to attain the data to plot a TTT diagram is through experiments involving differential scanning calorimetry (DSC). This is a technique where a small sample is heated, and the amount of heat introduced into the sample is recorded, as well as the temperature of the sam-

ple. This results in information about the heat capacity of the sample, and phase transitions will show up as discontinuities in the heat capacity of the sample. Using DSC, it is thus possible to pinpoint the time to the onset of crystallisation for different temperatures. A downside of this method is that most DSC machines do not reach the melting temperature of glasses. There are specialized high temperature DSC machines that can reach the temperatures where glasses are molten, which could be used to predict an accurate TTT diagram [50, 60, 61].

2.3.2. Creation of TTT diagram through computational methods

As can be seen in section 2.2.4, it is possible to use the equations of the classical nucleation theory to create a TTT diagram, provided the values of the parameters are known. Attaining these parameters is done through several methods, by using the results of experiments to estimate the values of the parameters of the classical nucleation theory [31, 62, 63], by using first principles to calculate the theoretical values for those parameters [64, 65], or even by using Molecular Dynamics (MD) simulations to extract the values for the parameters [66].

Using the first method, the values of the experiments are essentially fitted using an algorithm, in order to approach parameters for the classical nucleation theory or one of its derivative formulae that are congruent with the experiments. For the second method, a look is taken to the fundamental physics in order to predict the behavior of the atoms, and thus the parameters for the nucleation theories can be calculated. The third method resembles the second method, insofar as it simulates the interaction between atoms and then calculates the parameters for the nucleation theories, but it simulates this interaction using MD simulations, instead of manually calculating the component interactions. The specifics of this method are fully discussed in chapter 2.4.

2.4. Molecular dynamics simulations of glasses

One method of simulating materials such as glasses is through the method of Molecular Dynamics (MD). In this computational method, individual particles are represented as point masses, and the forces between these point masses are calculated using prescribed interaction equations. Using Newton's equations of motion, $a = {}^{m}/_{f}$, the displacements of the particles are calculated for a specific time interval, effectively moving these particles in discrete time intervals or timesteps. In the case of simulating molten oxide glasses, the particles represent individual atoms, and the interaction equations between them are derived from interatomic potentials between the different species of atoms in the simulation [67].

2.4.1. Interatomic potentials

The interatomic potentials are decidedly impactful on the behavior of the simulated material and as such care is to be taken in selecting potentials which will result in simulations with realistic results. This is since there are two methods of determining these interatomic potentials: ab initio calculations of the interactions between the species of atoms through density functional theory, and empirical determination of the potentials by validation with regards to known material characteristics. For this second option it is important to be aware for which characteristics the potentials have been validated, such as crystalline structure, bond orientations, thermodynamic properties, or a combination of those characteristics [68, 69].

Since the potential functions are more complex for the ab initio derived potentials, those potentials are uniquely suited for calculations with a small system size and high required accuracy, as the complex potential functions do not scale well in terms of computation time with an increase in numbers of particles. Conversely the comparatively simpler potential functions that are empirically derived allow for a higher number of particles to be simulated with the same computational capacity, which makes it a better choice for larger system sizes. As the investigation into the crystallisation behavior of glasses will require a combination of a large number of particles and long simulation times, ab initio derived potential functions are disregarded for this application on the basis of computational complexity [70].

One of the earliest practical interatomic potential function is the Lennard-Jones potential function, named after the author of the paper which first introduced the function [71]. Other pair potential functions include the Mie potential [72], Born-Mayer-Huggins potential [73], Morse potential [74], Buckingham potential [75], among others [68]. These pair potential functions describe the potential energy of a pair of particles, and the force between those particles is defined as the negative derivative of the pair potential function. The Lennard-Jones potential function can be viewed in equation 2.21 and figure 2.16, where in the equation U_{ij} represents the potential energy between particles i and j, r_{ij} represents the distance between the particles, ε is the depth of the potential well, and σ is the distance where the potential energy is equal to zero.

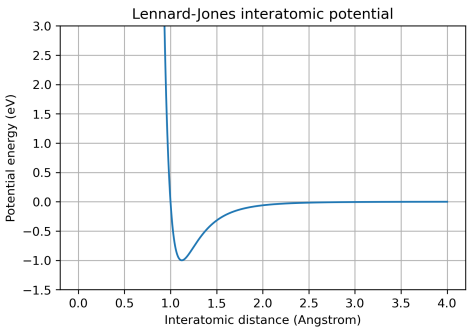

Figure 2.16: A plot of a Lennard-Jones pair potential function with $\varepsilon = 1eV$ and $\sigma = 1$Å.

$$U_{ij}(r_{ij}) = 4\varepsilon \left[\left(\frac{\sigma}{r_{ij}} \right)^{12} - \left(\frac{\sigma}{r_{ij}} \right)^{6} \right] \tag{2.21}$$

Alternatively the Buckingham interatomic potential is represented in equation 2.22, where the parameters A_{ij}, ρ_{ij} and C_{ij} are fitting parameters which do not represent a specific quantity.

$$U_{ij}(r_{ij}) = A_{ij} \cdot \exp\left(-\frac{r_{ij}}{\rho_{ij}}\right) - \frac{C_{ij}}{r_{ij}^6} \tag{2.22}$$

For charged particles there is the added dimension of electrostatic potential. As the physics are not complicated by complex quantum effects such as is the case with the chargeless potential functions, the electrostatic potential or the coulombic potential can be analytically represented by equation 2.23. In this equation C is an energy-conversion constant, q_i and q_j are the charges of particles i and j, and ϵ is the dielectric constant of the material. This electrostatic potential is layered on top of the interatomic potential function in the MD simulation to develop the total potential function of the charged particles [67, 68].

$$U_{ij}(r_{ij}) = \frac{Cq_iq_j}{\epsilon r_{ij}} \tag{2.23}$$

As the empirical interatomic potentials are developed for only a select combination of several atomic species, it is prudent to select a collection of interatomic potentials which describe the interaction between every species present in the sand that is to be used as a base for the glassmaking. One promising collection of interatomic potentials is the set developed by Du on the the basis of the Buckingham potential (equation 2.22)[69]. This set can represent the interactions between the species O, Si, P, Al, Li, Na, K, Ca, Sr, Y, La, Er, Eu, and Ce. The set of parameters for these interactions are represented in table 2.3. This set also uses partial charges instead of full charges, as it was found by Du that this leads to better results. The charges of the species particles are added as a superscript of the species designations [69].

Table 2.3: The interatomic potential parameters of the Buckingham potential function, as found by Du. Reproduced from [69]

Pair	A (eV)	ρ (Å)	C (eV Å^6)
$Si^{2.4} - O^{-1.2}$	13 702.905	0.193 817	54.681
$P^{3.0} - O^{-1.2}$	26 655.472	0.181 968	86.856
$Al^{1.8} - O^{-1.2}$	12 201.417	0.195 628	31.997
$Li^{0.6} - O^{-1.2}$	41 051.938	0.151 160	0.0
$Na^{0.6} - O^{-1.2}$	4383.7555	0.243 838	30.70
$K^{0.6} - O^{-1.2}$	20 526.972	0.233 708	51.489
$Ca^{1.2} - O^{-1.2}$	7747.1834	0.252 623	93.109
$Sr^{1.2} - O^{-1.2}$	14 566.637	0.245 015	81.773
$Y^{1.8} - O^{-1.2}$	29 526.977	0.211 377	50.477
$La^{1.8} - O^{-1.2}$	4369.39	0.2786	60.28
$Er^{1.8} - O^{-1.2}$	58 934.851	0.195 478	47.651
$Eu^{1.8} - O^{-1.2}$	5950.5287	0.253 669	27.818
$Ce^{1.8} - O^{-1.2}$	11 476.9522	0.242 032	46.7604
$Ce^{2.4} - O^{-1.2}$	31 697.724	0.218 36	90.659
$O^{-1.2} - O^{-1.2}$	2029.2204	0.343 645	192.58

2.4.2. MD boundary conditions

For ease of simulation a periodic boundary condition can be enforced, which states that if a particle crosses through the edge of the simulation box, it is reinserted at the opposite edge of the box with its velocity intact. Additionally, for the calculation of the forces on the atoms the opposite part of the simulation box is assumed to be situated beyond the edge of the simulation box. This essentially means that beyond the edges of the simulation box there lie additional images of the simulation box, which influence the forces on the atoms. This is helpful with simulating a collection of atoms which you

assume to be part of a larger homogeneous material, as one can simulate a larger material with vastly reduced computational costs.

When simulating a crystalline structure care is to be taken to ensure the dimensions of the simulation box correspond to a multiple of the unit cell dimensions of that crystal, in order to prevent unrealistic internal stresses from being created. Likewise for the simulation of glasses, the size of the system limits the size of the rings in the glass network, with smaller simulation sizes resulting in higher internal stresses. It has been found that an acceptable trade-off between computational costs and sufficiently relaxed structures is to use between 6000 and 10000 atoms in the simulation [67, 76].

During a simulation different thermodynamical conditions, or ensembles, can be imposed upon the simulation box. The most relevant thermodynamical ensembles for this work are the NVT and the NPT ensembles, where respectively the number of atoms(N), volume(V), and temperature(T), and the number of atoms(N), pressure(P), and temperature(T) are controlled to be constant during the simulation. This is achieved by using a software implementation of a thermostat for both NVT and NPT ensembles, and by using a barostat for the NPT ensemble. The thermostat works by scaling the velocity vectors of the particles crossing the edges of the simulation box after every time step, in order to ensure an average velocity that corresponds to the set temperature. This is conceptually the same as putting the simulation box in a heat bath at a set temperature. The barostat implementation likewise scales the volume of the simulation box to end up at a pressure which corresponds to the set pressure [67].

2.4.3. Approach using Classical Nucleation Theory for calculating TTT diagrams

Directly simulating glass using MD and waiting for a nucleus to form in the simulation box, using the latest simulation hardware, would require more computation time than there is time left in the lifetime of the sun [77]. Therefore an alternative method to determine the nucleation rate is required. One such method is the method that has come to be called 'seeding'. This method is a relatively recent technique [78–81], where a nucleus of a crystal is inserted into a simulated glass-forming liquid. This is then simulated, from which the relationship between the temperature and the critical nucleus radius is determined. This is done by simulating these implanted nuclei at different temperatures and noting at which temperature they grow and at which they shrink, as can be seen in figure 2.17.

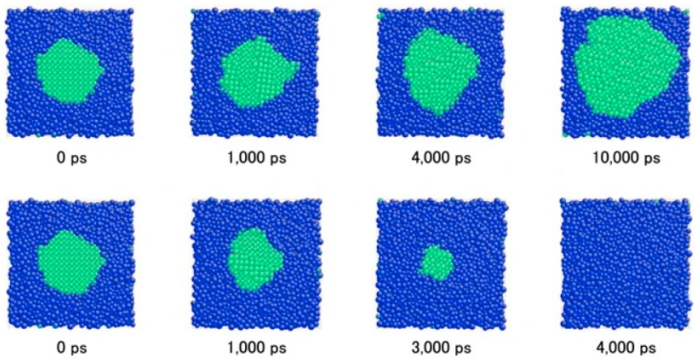

Figure 2.17: Snapshots of crystal nucleus growth and shrink processes of Cu50Zr50 model. The top row represents the growth process at T=1100K, while the bottom row denotes the shrink process at T=1200K. Green atoms represent a crystal phase, while blue represent the liquid phase. Reproduced from [66]

This relationship, $r^*(T)$, can subsequently be used to determine the temperature dependence of the free energy barrier for nucleation or activation energy ΔG^* / W^*. Necessary for this is to calculate the free energy of crystallisation ΔG_x, after which the interfacial free energy σ can be calculated, which is difficult to determine experimentally [81]. Together the interfacial free energy and the free energy of crystallisation determines the energy barrier for nucleation ΔG_*, and thus can be used to predict the nucleation behavior for different temperatures. This calculation is done using the following formulae [66]:

$$\Delta G_x = \Delta H_m \left(1 - \frac{T}{T_m}\right) - \int_T^{T_m} \Delta C_p dT + T \int_T^{T_m} \frac{\Delta C_p}{T} dT \tag{2.24}$$

$$\sigma = \frac{1}{2} r^* \Delta G_x \tag{2.25}$$

$$\Delta G^* = \frac{4}{3} \pi \sigma r^{*2} \tag{2.26}$$

where ΔH_m is the enthalpy difference between the melt and the crystal, and ΔC_p is the isobaric volumetric heat difference between the melt and the crystal.

This ΔG_x, σ and ΔG^* can be used to determine the crystal growth rate and the nucleation rate, which together result in the TTT diagram by use of equation 2.19. One example for this method is the work of Sato et al. [66].

The equation used in the work of Sato et al. for the calculation of the crystal growth rate is adapted from equation 2.10 and Frey et al.[50] by using the relation between the gas constant and the Boltzmann constant $R = N_a k_B$. This equation can be seen in equation 2.27, where ρ is the density of the melt at the specified temperature.

$$u = \frac{k_B}{3\pi a^2} \frac{T}{\eta} \left[1 - \exp\left(\frac{1}{k_B \rho} \frac{\Delta G_x}{T}\right)\right] \tag{2.27}$$

The equation used for the calculation of the nucleation rate can be viewed in equation 2.28 and is the adaptation of Sato et al.[66] of equation 2.7. Here Ω is a specified volume of the melt within the rate is calculated, ρ_m is the density of the melt, Z is the Zeldovich factor and $f^+(n^*)$ is the attachment rate of atoms to the critical nucleus size. The formula for the attachment rate and the Zeldovich factor can be viewed in equations 2.29 and 2.30[66], where $\left\langle \Delta n^{*2}(t) \right\rangle$ is the mean square displacement of atoms attaching to the nucleus in time interval t, and ρ_c^* is the atomic number density of the crystal at the critical nucleus size, and n^* is the number of atoms in the critical nucleus.

$$I = \Omega \rho_m Z f^+(n^*) \exp\left[-\left(\frac{W^*}{k_B T}\right)\right] \tag{2.28}$$

$$f^+(n^*) = \frac{1}{2} \frac{\left\langle \Delta n^{*2}(t) \right\rangle}{t} \tag{2.29}$$

$$Z = \sqrt{-\frac{1}{2\pi k_B T} - \frac{8}{27} \pi \sigma \left(\frac{3}{4\pi \rho_c^*}\right)^{2/3} n^{*-4/3}} \tag{2.30}$$

This approach only results in a description of the homogeneous nucleation behavior. While in some melts the heterogeneous nucleation behavior is dominant, fortunately in pure CaO-SiO_2 melts homogeneous nucleation is dominant [82]. This means that this method should be viable for the use of predicting the nucleation behavior in pure CaO-SiO_2 glass-forming liquids. Whether this remains true for impure mixtures remains to be seen.

2.4.4. Evaluation of crystallinity

An important aspect of the seeding method of determining the parameters of the classical nucleation theory is the evaluation of the size of the nucleus. This involves distinguishing a crystalline structure from the structure of a glass melt, and determining which particles belong to the crystal and which to the melt.

One promising method to attain this is by use of the local order parameter, also known as the Steinhardt order parameter, after the author who first suggested this method [83]. This method essentially uses spherical harmonics to gain information on the bond orientations of the nearest neighbours of a particle, and subsequently compares that to the bond orientations of one of the neighbouring particles. When there is a high correlation between the bond orientations of the two particles, the two particles are assumed to be part of a crystalline structure. This method allows for the distinction of FCC, BCC and HCP crystalline structures in monoatomic simulations [84–87]. Further works expanded this into more arbitrary crystalline structures and non-monoatomic crystals by looking into second neighbour bond orientation or machine learning, however this remains an ongoing field of study [88–91].

One implementation of this seeding method is made by Filion et al. [87]. In their model, the local bond orientational order parameter $q_{l,m}(i)$ of a particle i is calculated as in equation 2.31, where $N_b(i)$ is the number of nearest neighbours of particle i, and $Y_{l,m}$ are the spherical harmonics, $m \in -l, l$, of the polar and azimuthal angles θ and ϕ between particles i and j. The spherical harmonics are calculated as in equation 2.32, where P_m^l are the associated Legendre functions.

$$q_{l,m}(i) = \frac{1}{N_b(i)} \sum_{j=1}^{N_b(i)} Y_{l,m}(\theta_{i,j}, \phi_{i,j}) \tag{2.31}$$

$$Y_{l,m}(\theta, \phi) = \sqrt{\frac{2m+1}{4\pi} \frac{(m-l)!}{(m+l)!}} e^{im\theta} P_m^l\left(\cos\left(\phi\right)\right) \tag{2.32}$$

This is then used in equation 2.33, where the similarity between the bond orientational order parameters of particles i and j is evaluated. If this value exceeds a specific threshold, the bond between the two particles is regarded as solid-like. If a particle has a minimum of N solid-like bonds, the particle is counted as a solid particle and a part of a crystal.

$$q_l(i,j) = \frac{\sum_{m=-l}^{l} Re\left(q_{l,m}(i) q_{l,m}^*(j)\right)}{\sqrt{\sum_{m=-l}^{l} |q_{l,m}(i)|^2} \sqrt{\sum_{m=-l}^{l} |q_{l,m}(j)|^2}} \tag{2.33}$$

2.5. Research gap

In this chapter the current state of the art is explored on the subject of the determination of Time-Temperature-Transformation diagrams for glass. First the background on what constitutes glass is discussed, after which the process of nucleation and crystal growth is explored using the Classical Nucleation Theory. The creation of TTT diagrams is covered, both by physical as numerical methods, after which the intricacies of simulating glasses using numerical methods is explained. A method which is called Seeding is introduced, and it is a method that can be used to determine the parameters for the Classical Nucleation Theory by using numerical simulations of glasses. This method relies on the ability to accurate distinguish a crystal from a melt in a Molecular Dynamics simulation, and the state of the art of the detection methods are explored.

The Seeding method is the clear path towards answering the research question and gaining the information on the non-crystallisation temperature of a glass melt, as well as its critical cooling rate. This method has not yet been applied to a composition similar to the one of interest, nor has it been used on a composition as varied as the chosen one. The challenge of this work, and the research gap that it aims to close, is therefore to adapt the seeding method to be usable for the composition of the feedstock of calcium rich desert sands. The steps to attain this goal are laid out in chapter 3.

3

Methods

In order to answer the research question the Seeding method is applied for the given composition of the desert sands, and in this chapter the methods used are described. The Seeding method is chosen as it is able to supply both the non crystallisation temperature of a glass, and the critical cooling rate of that glass. In addition it is also able to be relatively quickly adapted for a slightly different composition, which is of value for the company as a tool in future research.

In this chapter first the physical experiments will be discussed, which are aimed at the validation of the model, as well as determining the composition of the given feedstock and the crystalline structure that will form initially at crystallisation in this material. Then the numerical methods to determine the TTT diagram are discussed. All the parameters of the numerical model will be discussed, as well as the chosen simulation steps and settings. Lastly the method to create the TTT diagram from the results of the simulation steps will be discussed.

3.1. Physical experiments

The goal for the physical experiments is to validate the results of the numerical experiments. This is achieved by subjecting melts to a specific temperature, and then evaluating whether or not the melt has crystallized, as well as the volumetric proportion of crystallisation. In addition to this, characterisation on the resulting samples of the experiment is done in order to determine the composition of the samples, as well as the crystalline structures that form when the samples crystallize.

The samples used in this project are made from desert sands which were processed by the company. Several batches of this feedstock was made available for the project, and a single batch was chosen for use in the project.

3.1.1. Composition determination

For the validation of the numerical results it is of importance that the composition both in the physical as the numerical experiments are congruent to each other. As it is more practical to adjust the composition in the numerical experiments than in the physical experiments, it was decided to measure the composition of the samples in the physical experiments. One sample of the batch of samples created in the experiments described in section 3.1.3 was examinated using a Panalytical Axios Max WD-XRF spectrometer to determine the composition of this batch of glass.

Figure 3.1: A sample of desert sands which was fully crystallized. This sample has been designated *full* in section 4.1.1.

3.1.2. Crystal determination

For the numerical experiments it is additionally of import to have the information on which crystal structure will form first in the melt, as that is the structure that is inserted in the simulation. This structure can be determined using XRD equipment in the form of a Bruker D8 Advance diffractometer using Bragg-Brentano geometry and a Lynxeye position sensitive detector. As the feedstock is reminiscent of an CaO-SiO_2 binary system, the literature suggest that the expected crystalline structure to form first is that of Wollastonite-1A crystal, which is a mineral that has the chemical formula of $CaO - SiO_2$ or $CaSiO_3$[92–95]. However, as the feedstock differs significantly from a pure CaO-SiO_2 binary system, it is prudent to verify the real crystalline structure that forms initially. To attain this several crystallized samples were subjected to an XRD investigation. Several samples were made available for this project by Maana Electric for this purpose.

One sample results from an earlier experiment with the processed desert sand where it has been left in an oven for over 3 days at 1300 °C, after which it was allowed to cool slowly. These samples were fully crystallized, and as can be seen in figure 3.1 they exhibit banding in distinct colors. This banding can be explained by the presence of two or more different crystalline phases, where the composition does not have the perfect proportions of the components to result in a single phase. This means that one of these phases formed before the other, and that is the one of interest.

Another sample that has been provided is one which is presumed to be only partially crystallized. In this sample, which can be seen in figure 3.2, we can again see banding has occurred. Yet the material in between the bands is not crystallized, and has been cooled into glass. This banding we can again tentatively attribute to the phenomenon of the composition of the bulk changing when crystalline structures are formed. These crystalline structures are then the first that form, and are of interest for this project. The identification of these structures will be done with the XRD analysis.

A third sample has been provided, which is the result of a glass pour by Maana Electric. Some of the remaining glass in the crucible became crystallized, which is a good example of the phenomenon that is to be studied. The sample can be seen in figure 3.3, and the yellow colouring is due to the addition of a few weight percent of Cerium Oxide. This addition could presumably change the preferentially formed crystal, however it is small and if the preferentially formed crystal does not contain cerium one could assume it to have no effects.

(a) The full sample with all its fragments.

(b) A few fragments of the sample on their side, showing the banding inside.

Figure 3.2: A fragmented sample of desert sands which was presumed partially crystallized. This sample has been designated *partial, green* in section 4.1.1.

(a) The alumina crucible with a partially crystallized layer of glass melt.

(b) Closeup of the crystal in the glass.

Figure 3.3: A partially crystallized sample of glass stuck in an alumina crucible. This sample has been designated *partial, yellow* in section 4.1.1.

3.1.3. Crystallisation experiment starting from the solid state

A weight of 500g of feedstock from the selected batch of processed desert sand is placed in an Alumina crucible, and was melted at 1400 °C. This melt is subsequently poured into moulds and annealed in an annealing oven at 750 °C. This results in 18 usable samples, from which more have been created by breaking them in smaller pieces.

A portion of these samples are heated from room temperature to 900 °C, and removed one by one from the oven at set time intervals. This is done to study the crystallisation behavior of this glass when the temperature is approached from low temperatures. The assumption is that nuclei and crystalline structures have no time to form when cooled quickly from 1400 °C, so the glass is assumed to be free of crystalline structures when heated to 900 °C. The experiment is repeated with a different set of samples from the same pour at 950 °C and 1000 °C.

One batch of 6 samples are set in an electric oven and, over a period of 6 hours, warmed up to 750 °C. They have been left at this temperature for one hour, after which the temperature is increased in 15 minutes to 900 °C. After 82 minutes at this temperature the first sample is removed and allowed to cool to room temperature under a ceramic wool insulation blanket. This ceramic wool insulation blanket allows the sample to cool slowly to room temperature, which prevents the sample from breaking due to thermal shock. The remaining samples are removed from the oven in intervals of 59, 70, 70, 65 and 59 minutes.

Several larger samples were broken in smaller pieces to create 15 smaller samples. These samples were set in an electric oven, and heated up to 750 °C in 6 hours. After which the temperature is increased to 950 °C in 36 minutes. Upon reaching the first sample is removed from the oven and left to cool under a composite wool insulation blanket, after which the next samples are respectively removed from the oven in intervals of 30, 33, 30, 27, 44, 31, 33, 28, 31, 29, 29, 33, and 29 minutes.

A batch of 6 samples are set in an electric oven and heated to 750 °C in 6 hours. They are left at this temperature for 45 minutes, after which it is heated to 1000 °C in 44 minutes. After 62 minutes at this temperature the first sample is removed from the oven and allowed to cool under a blanket of ceramic insulation wool material. Due to the results as described in section 4.1.3 the decision was made to allow the remaining samples to cool in the oven.

3.2. Computational experiments

The computational experiments will be conducted in the form of Molecular Dynamics (MD) simulations and the software suite that is used in these simulations is LAMMPS Molecular Dynamics Simulator [96]. The choice of this software is based upon it supporting a wide array of interatomic potentials, as well as having the ability to take advantage of hardware features of the computer such as parallel computation at the hardware level on the CPU and GPU.

The experiments will loosely follow the examples set by Sato et al. [66] and Frey et al. [50], both of which are implementations of the seeding method. A summary of the steps involved is as following:

- A simulation of 8000 atoms is created with the species of the atoms in proportion to a given composition.
- This simulation box is simulated to develop a structure that is analogous to a glass melt.
- A spherical section of this melt is replaced with a crystal structure.
- The whole system is simulated in order to evaluate if this size of crystal nucleus grows or shrinks at that specific temperature in a glass melt.
- After several iterations of collecting simulation results, the data can be used to construct the temperature dependence of the critical nucleus size.
- This result, together with the temperature dependence of the density and enthalpy of both the glass melt and the crystal, and the viscosity of the melt, allows for the construction of the TTT diagram.

A flowchart in which the steps of the main experiment are listed has been created and can be viewed in figure 3.4. The precise content of the steps will be discussed in the following sections.

3.2.1. Setting up pair potentials for MD simulations in LAMMPS software

The calculation of the forces between different atoms is one of the most important aspects to ensure a realistic simulation as described in section 2.4.1. These forces are often described by using pair potential functions, where the force between a pair of atoms of specified species is defined as a function of the interatomic distance. The determination and validation of these pair potential functions are quite involved, so it is best practice to select an appropriate pair potential function from the literature.

A recent overview of the history and state of the art of the various pair potential functions and their parameters for the simulation of oxide glasses has been performed[68], and from this overview a set of pair potential functions and the accompanying parameters is selected[69]. This set of pair potentials is a model that assumes rigid ions, and is selected by virtue of it being the simplest model that is valid for the composition that was provided, in addition to it being supported in the LAMMPS software. The short range interaction of this model is displayed in the form of a Buckingham potential function which can be seen in equation 3.1, which is a modification of equation 2.22, while the interatomic potential parameters that correspond to this function are portrayed in table 3.1. In this function, r_{ij} is the interatomic distance between ions of species i and j in Å, and A_{ij}, ρ_{ij} and C_{ij} are pair potential parameters specific for the interaction between ions of species i and j in eV, Å, and eV Å^6 respectively. In this function only neighbouring ions with a maximum distance of r_{cutoff} will be considered, which is done to limit the computational load of the simulation. The cutoff distance for all potential functions, unless otherwise stated, is set to 8.0Å as beyond that value the potentials are negligible.

$$U_{ij}(r_{ij}) = A_{ij} \cdot \exp\left(-\frac{r_{ij}}{\rho_{ij}}\right) - \frac{C_{ij}}{r_{ij}^6} \qquad r_{ij} < r_{cutoff} \tag{3.1}$$

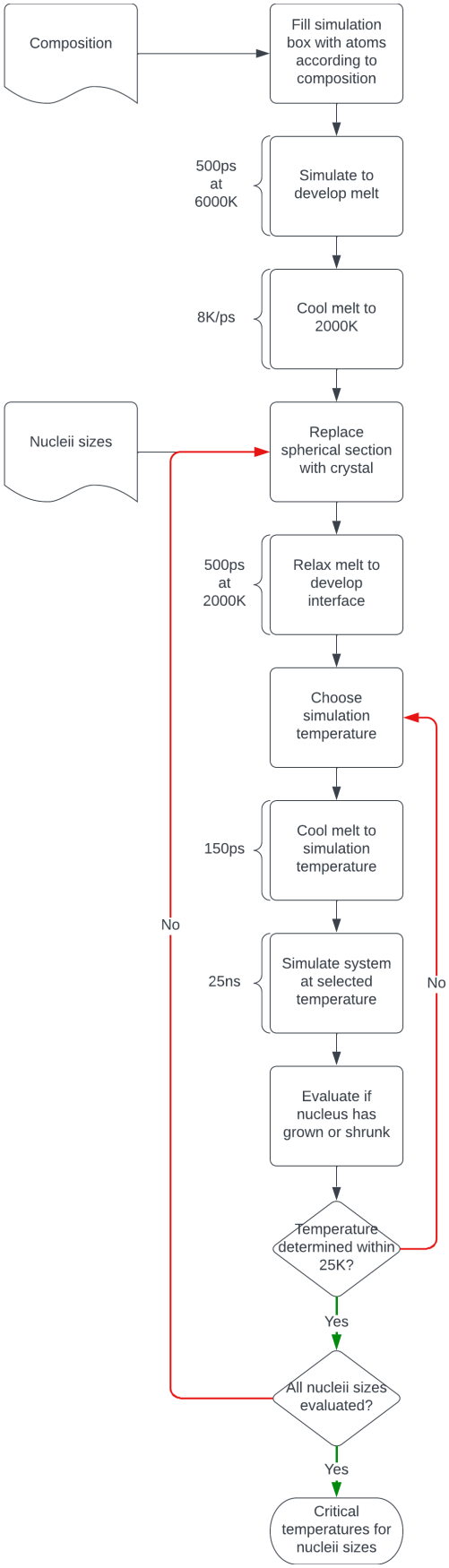

Figure 3.4: Flowchart of the simulation process.

Table 3.1: The interatomic potential parameters that are used in the Buckingam potential function, as used in the LAMMPS simulations. Adapted from [69]

Pair	A (eV)	ρ (Å)	C (eV Å^6)	σ (Å)
$Si^{2.4} - O^{-1.2}$	13 702.905	0.193 817	54.681	1.0
$P^{3.0} - O^{-1.2}$	26 655.472	0.181 968	86.856	1.05
$Al^{1.8} - O^{-1.2}$	12 201.417	0.195 628	31.997	1.0
$Li^{0.6} - O^{-1.2}$	41 051.938	0.151 160	0.0	0.0
$Na^{0.6} - O^{-1.2}$	4383.7555	0.243 838	30.70	1.0
$K^{0.6} - O^{-1.2}$	20 526.972	0.233 708	51.489	0.9
$Ca^{1.2} - O^{-1.2}$	7747.1834	0.252 623	93.109	1.1
$Sr^{1.2} - O^{-1.2}$	14 566.637	0.245 015	81.773	1.0
$Y^{1.8} - O^{-1.2}$	29 526.977	0.211 377	50.477	0.9
$La^{1.8} - O^{-1.2}$	4369.39	0.2786	60.28	1.1
$Er^{1.8} - O^{-1.2}$	58 934.851	0.195 478	47.651	0.8
$Eu^{1.8} - O^{-1.2}$	5950.5287	0.253 669	27.818	1.0
$Ce^{1.8} - O^{-1.2}$	11 476.9522	0.242 032	46.7604	1.0
$Ce^{2.4} - O^{-1.2}$	31 697.724	0.218 36	90.659	1.0
$O^{-1.2} - O^{-1.2}$	2029.2204	0.343 645	192.58	1.55

The Buckingham potential form is unfortunately not realistic at very small interatomic distances. While it is expected that at very small distances the interatomic potential results in an exponentially increasing repulsive force, the Buckingham potential results in an exponentially increasing attractive force for very small distances, as can be seen in figure 3.5. This could result in the fusing of two particles when they come within a certain distance, typically within 1Å. This normally is of little concern as in a typical simulation the particles do not stray into that region, however in this work there is the possibility for this to occur due to the high temperatures involved as well as the high energy initial state as to be discussed in section 3.2.2. To counteract this a second interatomic potential function is overlaid on the Buckingham potential function, with a very small cutoff distance in order to only affect the problematic section and not influence the rest of the potential. This overlaid potential function therefore changes the behavior of the combined potential functions into resulting in repulsive forces for very small distances.

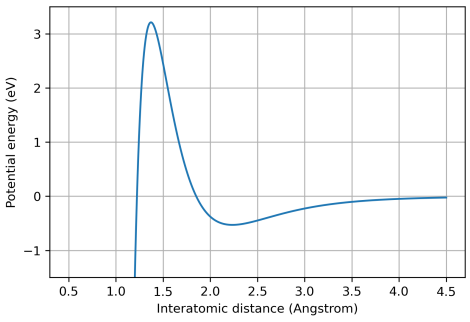

Figure 3.5: A plot of a Buckingham potential function of the interaction between Calcium ions and Oxygen ions for the parameters described in table 3.1.

The potential function chosen for this purpose is of the Lennard-Jones shape, and can be seen in equation 3.2. Here ε represents the depth of the potential well, while σ represents the distance where the function has a potential of zero. In this application the exact value of these coefficients are of little interest. It is important to set the correct cutoff distance, and to ensure continuity it is helpful to set the value of σ to the same value, as this results in a potential of zero at the cutoff distance. The value for ε is chosen as 1.0, while the values for σ and r_{cutoff} are taken to be the same but vary for the different interaction pairs and are given in the rightmost column of table 3.1.

$$U_{ij}(r_{ij}) = 4\varepsilon \left[\left(\frac{\sigma}{r_{ij}} \right)^{12} - \left(\frac{\sigma}{r_{ij}} \right)^{6} \right] \qquad r_{ij} < r_{cutoff} \tag{3.2}$$

The Coulomb force due to the interaction between charged particles is specified as being in the shape

as can be seen in equation 3.3,

$$U_{ij}(r_{ij}) = \frac{Cq_iq_j}{\epsilon r_{ij}} \qquad r_{ij} < r_{cutoff} \tag{3.3}$$

where C is is an energy-conversion constant, q_i and q_j are the charges of the ions, and ϵ is the dielectric constant of the material. The charges for the individual ions are given in table 3.1. And while a cutoff distance is specified in the equation, the long range Coulombic interaction does not cease at this distance. Instead, from this distance the long range Coulombic interaction is calculated in the frequency domain.

There is no interatomic potential function specified between the different anions in table 3.1, the sole forces between these anions result from the coulombic interaction. The lack of specification of a specific interatomic potential function for the anionic interaction is justified as even if there were an interatomic potential specified, its contribution at the typical distances between these particles would be insignificant when compared to the contribution of the Coulombic interaction. Thus it would be acceptable to disregard this component for the simulation of the developed glass melt. There is a concern what the behavior is of anions which have an unrealistic low distance between them. While the electrostatic force alone would prevent two anions from approaching too close, an additional interatomic potential is added with a short cutoff distance to quell these concerns. The chosen potential form is again of the Lennard-Jones shape, as seen in equation 3.2, where the values for ε, σ and r_{cutoff} for all anionic combinations are set to 1.0, 2.5 and 2.5, respectively.

The potential functions of equations 3.1, 3.3 and 3.2 are then combined in the software, and together they form the model of the melt. This model, and their relative impact at different distances, can be seen in figure 3.6 for the example of the interaction between Calcium and Oxygen.

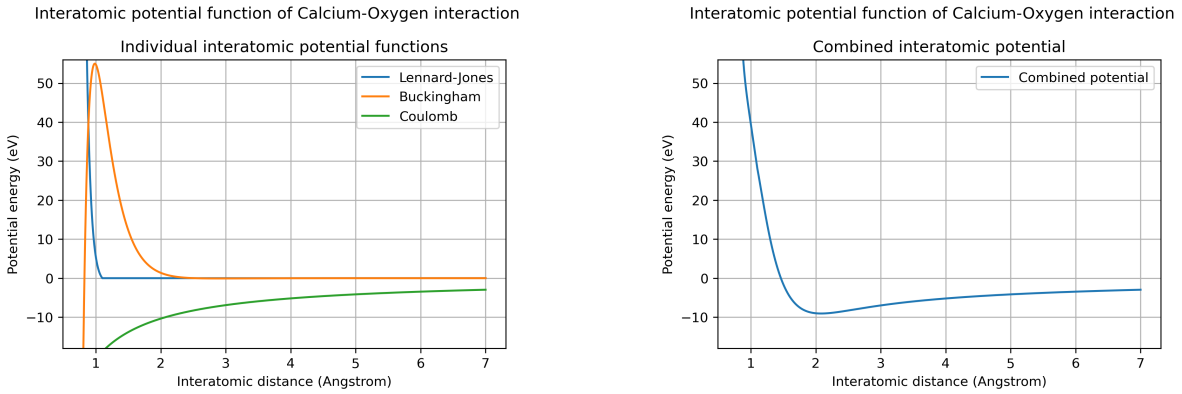

(a) A plot of the constituent potential functions which together represent the Ca-O interatomic potential.

(b) A plot of the total of the potential functions which together represent the Ca-O interatomic potential.

Figure 3.6: The Calcium - Oxygen interatomic potential as implemented in the LAMMPS software.

3.2.2. Generating the initial melt

The simulation box is populated by a collection of 8000 randomly placed atoms, in such a proportion that the amount of atoms of a specific species corresponds to the specified composition of the material. Care is taken in choosing the exact proportions in order to guarantee charge neutrality for the selected number of atoms. During the randomized placement it is ensured that no atoms are within 1.6 Å from each other to prevent excessive initial forces on those atoms. Additionally, the total volume of the simulation box is set to a value so that the average volume per atom is 37.5 Å^3 as that is around the density the simulation settles at during testing. This prevents excessive volume and pressure fluctuations and reduces the time required to stabilize the simulation in the subsequent simulation

steps.

As the atoms are placed randomly in the simulation box, it is almost guaranteed that these atoms are not in their equilibrium position. If this collection of atoms were to be simulated, this would result in very high forces on the atoms, which is something the simulation software cannot handle at a reasonable timestep. As the high forces lead to high displacements the atoms would move out of their potential well during a timestep, leading to a failed simulation. Therefore a minimisation algorithm is executed, wherein every individual atom is moved about slightly and the position with the lowest energy is taken as the new position. This operation essentially moves every atom into their local energy minimum position.

A NPT simulation is then run for 500ps at 6000K to let this randomized collection of atoms self organize into a structure that resembles a molten oxide melt. The first 5ps is simulated at a timestep of 1fs, while the rest of the simulation is run at a timestep value of 4fs. This is to account for the high initial forces and subsequent velocities of the atoms, where a higher timestep value would not be sufficient to capture the high oscillation frequencies of the initial configuration. Subsequently, the melt is cooled from 6000K to 2000K at a cooling rate of 8K/ps at a timestep of 4fs. This is to reduce the computational time required during subsequent steps where the melt with the inserted nucleus is cooled to the relevant temperature. A snapshot of this simulation is saved in order to serve as a starting point for subsequent steps.

3.2.3. Inserting nucleus in the bulk melt

The crystal that is to be inserted, as can be seen in section 4.1.1, has been found to be Wollastonite, a triclinic crystal with space group $P\bar{1}$ and a chemical formula of $CaSiO_3$. The relative locations of the atoms in the unit cell of the Wollastonite crystal has been found in the literature[97], as well as the temperature dependence of the lattice parameters[98]. Unfortunately the formulae for the temperature dependence of the lattice parameters were only given for a temperature range of room temperature up until 962 $^\circ$C. In addition, testing of the atom locations in the simulation has shown that these values are slightly off for the interatomic potentials used in this work. Therefore several simulations have been performed in order to discover the correct lattice parameters and atom locations for the Wollastonite crystal in the simulation. This resulted in a scaling factor of 1.072 for the lattice parameters as given from the formulae from the literature in the range 1200K - 1800K, as well as the atom locations relative to the lattice vectors as given in table 3.2.

Given this lattice, the atoms in a spherical region of a certain radius are deleted from the developed melt. These atoms are then replaced with atoms in the configuration of the defined lattice. During this insertion care is taken to ensure the charge neutrality of the system. Before the deletion of the atoms in the spherical region the net charge of the remaining atoms is calculated, and the location of the spherical region is varied in order to ensure a net neutral charge in the remaining melt. Likewise, the net charge of the to be inserted Wollastonite crystal is calculated, and the crystal lattice is rotated in discrete steps until the charge of the to be inserted nucleus is neutral. The net linear momentum of the remaining melt is also set to 0 in order to prevent the system moving in relation to the simulation box.

As the inserted nucleus is almost guaranteed to not be properly connected to the rest of the melt, it is important to ensure it is. Therefore an energy minimisation step is done on the atoms of the melt while leaving the atoms of the nucleus fixed, in order to prevent the worst of the initial velocity effects from happening. This is especially important, as in contrast to the unrealistic initial state of the melt there has been no provision made to ensure at least a distance of 1.6 Å between the atoms. This would make it possible for atoms with a like charge to be practically on top of each other, leading to extremely high velocities on the first simulation steps. And this is to be avoided.

As with the initial melt, the atoms of the melt excluding the nucleus are simulated for 500ps at 2000K. The atoms of the nucleus are considered for the forces on the atoms of the melt, but are not moved themselves. Again the initial 5ps are simulated utilizing a timestep of 1fs, while the remaining 495ps are simulating with a 4ps timestep value. This will allow the atoms in the melt to orientate themselves

Table 3.2: Atom locations in the Wollastonite crystal lattice unit cell, relative to the lattice vectors. As the lattice has $P\bar{1}$ symmetry, only half of the atom locations are given.

	x	y	z
Ca_1	0.2123	0.4213	0.7507
Ca_2	0.2082	0.9360	0.7535
Ca_3	0.5033	0.2509	0.4846
Si_1	0.1821	0.3848	0.2487
Si_2	0.1825	0.9567	0.2513
Si_3	0.3933	0.7238	0.0458
O_1	0.4371	0.2316	0.8146
O_2	0.4159	0.7321	0.8288
O_3	0.2947	0.4525	0.4423
O_4	0.2944	0.9457	0.4455
O_5	0.0138	0.6157	0.7473
O_6	0.0138	0.1387	0.7416
O_7	0.2770	0.5194	0.0904
O_8	0.2727	0.8666	0.0914
O_9	0.1904	0.1723	0.2111

properly with regards to the atoms in the nucleus, which creates a realistic starting configuration for the simulation.

After this creation of an interface layer the melt is at the volume of 2000K, while the nucleus is at the volume of the inserted temperature, which is given by the scaled formula for the temperature dependence of the lattice parameters. Thus it is prudent to let the melt cool down so its volume corresponds to the desired temperature before beginning the full simulation. This cooling is achieved by simulating under a NPT ensemble for 150ps with a timestep of 3fs, where the setpoint of the thermostat decreases linearly from 2000K to the desired temperature. An additional NPT simulation of 45ps with a timestep of 3fs at the desired temperature is run to allow the material to settle at that temperature.

It was found that when a simulation was started from this situation, the temperature in the simulation would plummet in the first few femtoseconds, which is undesirable for this kind of simulation as it is unrealistic and increases the time to equilibrium. The culprit was assumed to be the random velocity vectors attributed to the atoms of the Wollastonite crystal, of which a portion would presumably cancel out during the first simulation steps, decreasing the temperature. A workaround for this problem was constructed by setting the temperature of the atoms in the nucleus a factor 2.05 higher than the desired temperature. This would mitigate the initial temperature drop and would let the temperature stabilize in around 100fs as opposed to over 1000fs, as can be seen in figure 3.7. To implement this a NVT simulation is run on only the atoms in the nucleus for 800fs with a timestep of 4fs. This allows the nucleus atoms in the simulation to develop more realistic velocity vectors.

3.2.4. Simulate the melts with inserted nuclei at different temperatures

The melt with inserted nucleus from section 3.2.3 is subsequently simulated at several temperatures. The temperatures are chosen in order to narrow down on the critical temperature for the chosen nucleus size, a temperature which is the dividing line between an unstable or stable nucleus of that size. For a chosen nucleus size and temperature, a simulation in the NPT ensemble is run for 100ps at a timestep of 4fs. The result of this simulation is then evaluated for the size of the nucleus, the method of which is described in section 3.2.5. After this evaluation the simulation is continued for another 100ps. After 250 iterations a linear fit is performed on the data on the size of the nucleus throughout the total 25ns simulation, and this allows the determination whether the nucleus has grown or shrunk during the simulation. Subsequently, a new simulation is run at a different temperature for the same nucleus size.

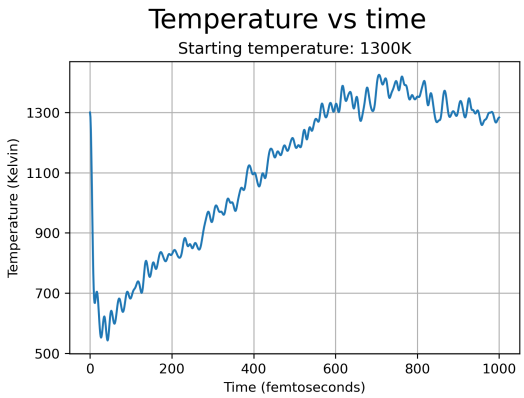

(a) Temperature-time plot of a simulated crystal of Wollastonite during an NVT simulation with a thermostat set to 1300K, after insertion at 1300K.

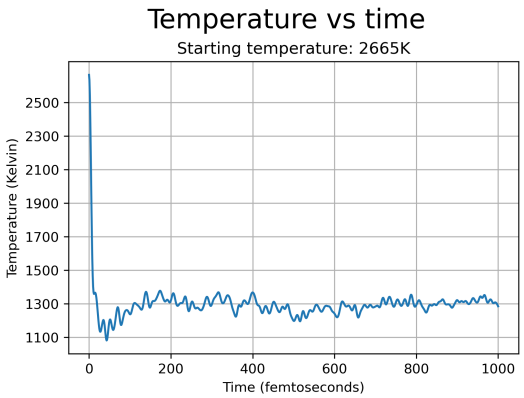

(b) Temperature-time plot of a simulated crystal of Wollastonite during an NVT simulation with a thermostat set to 1300K, after insertion at 2665K.

Figure 3.7: Comparison of the effects of the starting temperature of the randomized velocity vectors of the simulated Wollastonite atoms on the time it takes to settle at the desired thermostat temperature.

This information about the temperature at which the nucleus is stable or unstable is used to inform the subsequent temperature at which the simulation is run. The relevant piece of information is the temperature interval in which the critical temperature is situated, and as such subsequent simulations are used to narrow that interval to within 25°C. This interval is chosen as a compromise between simulation time and precision.

The result of this investigation is the interval in which the critical temperature for that size nucleus lies. This investigation, from the insertion of the nucleus to the determination of the temperature interval, is carried out for the selection of nucleus sizes as given in table 3.3. These sizes are chosen as to provide for a broad range of datapoints in the relation between the critical temperature and the nucleus size. In addition to this the sizes are small enough to not require an excessive amount of atoms in the simulation to ensure realistic results, limiting the required computational capacity.

Table 3.3: The radii of the nucleii of which the critical temperature is to be investigated.

Nucleus sizes			
1.9nm	1.6nm	1.3nm	1.1nm

3.2.5. Evaluating the crystallinity of the melt

In order to determine the size of the nucleus in the melt during the simulations the amount of atoms in the nucleus have to be calculated. This involves distinguishing atoms which belong to the crystalline nucleus from atoms that are part of the melt. No method to reliably differentiate between Wollastonite crystal and a glass melt has been found in the literature, so a variation on the method as described by Filion et al.[87] has been created.

The method used by Filion et al. is effective in a system with like particles, but is ineffective in a system with multiple species since the bond orientational order of nearest neighbours are compared, where in an ionic crystal the nearest neighbours do not correspond to identical positions in the unit cell. After careful inspection of the Wollastonite crystal, it was decided to only compare the local bond orientational order of Calcium atoms in the melt with their nearest neighbouring Calcium atoms, while computing the local bond orientational order of the Calcium atom in relation to their nearest neighbouring Oxygen atoms.

This means that in equation 2.31 (repeated as equation 3.4) the local bond orientational order $q_{l,m}(i)$

is calculated only for the Calcium particles i, while the nearest neighbours j which are evaluated are generally Oxygen particles. The 6 nearest neighbours are selected by taking the 6 particles with the lowest distance to the Calcium particle.

$$q_{l,m}(i) = \frac{1}{N_b(i)} \sum_{j=1}^{N_b(i)} Y_{l,m}(\theta_{i,j}, \phi_{i,j}) \tag{3.4}$$

The degree of the spherical harmonic function l is taken as 4 since the orbitals of that degree closely resembles the bond directions of the nearest neighbouring Oxygen particles of the Calcium particles in the Wollastonite crystal. A quick verification confirms degree 4 to be superior to degree 6 in regards to the detection of Wollastonite crystal.

The nearest neighbouring Calcium particles designated by the subscript j in equation 2.33 (repeated as equation 3.5) are those Calcium atoms which lie within 6.0Å of the center Calcium atom i. The local bond orientational order $q_{l,m}(i)$ and $q_{l,m}(j)$ is, as previously stated, the bond orientational order of the 6 nearest neighbouring (oxygen) particles around the Calcium particles i and j.

$$q_l(i,j) = \frac{\sum_{m=-l}^{l} Re\left(q_{l,m}(i) q^*_{l,m}(j)\right)}{\sqrt{\sum_{m=-l}^{l} |q_{l,m}(i)|^2} \sqrt{\sum_{m=-l}^{l} |q_{l,m}(j)|^2}} \tag{3.5}$$

The threshold for $q_l(i,j)$ to be considered solid-like is set to 0.29, while a particle is considered solid and part of the crystal if it has at least 6 solid-like bonds. To make the detection algorithm more robust additional steps are taken. The particles which share a solid-like bond with a solid particle but are not recognized as a solid particle themselves, for example particles at the edge of the nucleus, are added to the group of solid particles. Additionally only the largest cluster of solid particles is counted in order to disregard incidental false-positives.

3.2.6. Creating TTT diagrams

As is clear from equations 2.18 and 2.19, the crystal growth rate and the nucleation rate is necessary to construct a TTT diagram. Both can be constructed with data derived from the previous described numerical experiments, the viscosity as predicted by Giordano[45], and further numerical experiments described in this section.

In order to calculate the crystalline growth rate of equation 2.27 and the nucleation rate of equation 2.28, equations 2.24, 2.25 and 2.26 are used. For this the temperature dependence of the critical nucleus size r^*, the density and enthalpy temperature dependence of both the melt and the crystal, the viscosity of the melt, and the nuclear attachment rate are to be determined. The volumetric heat difference ΔC_p is taken as the derivative of the enthalpy difference.

Using a linear regression the critical nucleus sizes from section 3.2.4 are used to fit the relation between $1/r^*$ and the temperature. To calculate the density and the enthalpy of the melt at different temperatures the melt as described in section 3.2.2 is taken and simulated at several different temperatures while calculating the temperature and the enthalpy of the melt. The temperatures are taken to from 1100K with intervals of 50K up until the projected melting temperature. The melt as created in section 3.2.2 is taken and cooled from 2000K to the highest temperature to be investigated in 60ps at a timestep of 3fs. All subsequent simulations are done at a timestep of 3fs. At this temperature it is simulated for 45ps to measure the average atomic density and enthalpy, after which the melt is cooled to the

next temperature in 30ps and investigated at that temperature for 36ps. This is repeated for all to be investigated temperatures.

The determination of the density and the enthalpy of the crystal follows the same procedure, except for first creating a simulation system containing 7 by 7 by 7 Wollastonite unit cells. This is the amount of unit cells that result in around 10000 particles in the simulation, which leads to a relatively stable system in terms of density and enthalpy. This system is created using the coordinates and lattice parameters as described in section 3.2.3, and the temperature is taken for the first temperature which is to be investigated. This system is then simulated at this first temperature for 30ps in order to let it settle in equilibrium, after which it is simulated at this same temperature for 45ps in order to determine the average density and enthalpy. The rest of the procedure is identical to the case of the melt as described in the previous paragraph, which means that it is cooled to the next temperatures in 30ps and investigated for 36ps.

This results in a set of points for both the density and the enthalpy of the melt and the crystal. The density is fitted linearly, while the enthalpy received a polynominal fit in the form of $H(T) = aT^2 + bT + c$ as those are roughly the scaling factors with the temperature for those properties[66].

The attachment rate is calculated by simulating a system with an inserted nucleus of a certain size at the critical temperature for that size nucleus, and subsequently calculating the attachment rate during this simulation. The reasoning behind this is that at this temperature, both the attachment rate as well as the detachment rate are equal to each other, making it possible to calculate the attachment rate separately.

Three simulation systems are created with a nucleus sizes of 2.0, 1.4, and 1.0nm using the method as described in section 3.2.3. These systems are simulated 20 times for 10ps with a timestep of 4fs, where in between every iteration the nucleus size is evaluated using the method as described in section 3.2.5. This data is then used to compute the average mean square displacement of the nucleus size, leading to the attachment rate by means of equation 2.29. Do note that the nucleus sizes are multiplied by a factor of 5 in order to attain the true number of atoms in the nucleus, as the method in section 3.2.5 only returns the amount of Calcium atoms.

4

Results

4.1. Physical experiments

Several physical experiments were conducted in order to attain information relevant for the use in the numerical experiments, or in order to validate the results of the numerical experiments. Their results are described in this section.

4.1.1. Determination of crystalline structure

Of interest of the samples in figure 3.1 and 3.3 is that the crystalline structures appear to be in the form of needle-like grains. The implication of this is that the crystalline structures have a preferential growth in a single dimension, resulting in rods. This is opposed to a preferential growth in two dimensions that would result in platelets, or three dimensional preferential growth that would result in crystals resembling the unit cell shape. This one dimensional preferential growth has implications for the crystal growth aspects of the nucleation theories, and as such this is valuable information for the proper prediction of nucleation and crystal growth behavior.

The XRD analysis has been conducted on all three samples, and the results can be seen in table 4.1. It can be concluded that the first crystalline structure that forms is indeed Wollastonite-1A. This was the sole crystalline structure in the sample from figure 3.3, while the other phases apart from Wollastonite that formed in the sample from figure 3.1 are Augite and Anorthite. There does not appear to be any crystalline fraction in sample 3.2. The full XRD measuring report can be found in appendix 6.1.

Table 4.1: The results of the XRD investigation into the crystal species.

Sample	Compound	
Full	Wollastonite-1A, Fe+2-bearing	(Ca2.87Fe0.13)(SiO3)3
	Augite	Ca(Mg,Fe)Si2O6
	Anorthite, Na-bearing	(Ca2.133Na1.867)(Si10.003Al5.987)O32
Partial, green	amorphous	
Partial, yellow	Wollastonite-1A, Fe+2-bearing	(Ca2.87Fe0.13)(SiO3)3

4.1.2. Determination of composition

One sample of the experiment as described in section 3.1.3 and 4.1.3 is analyzed using XRF, and this yields the composition as described in table 4.2. The full XRF report can be found in appendix 6.1.

Table 4.2: The composition of the samples as found by the XRF investigation.

Compound Name	Concentration (wt%)	Absolute Error (wt%)
SiO_2	56.121	0.1
CaO	33.139	0.1
Al_2O_3	4.839	0.06
MgO	2.308	0.05
Fe_2O_3	1.329	0.03
K_2O	0.909	0.03
Na_2O	0.894	0.03
TiO_2	0.145	0.01
SrO	0.07	0.008
P_2O_5	0.061	0.007
Cr_2O_3	0.046	0.006
MnO	0.036	0.006
BaO	0.025	0.005
SO_3	0.025	0.005
ZrO_2	0.019	0.004
NiO	0.019	0.004
Cl	0.014	0.004
Rb_2O	0.002	0.001

4.1.3. Crystallisation starting from the solid state

A batch of benificiated sand is molten at 1400 °C and poured into 18 samples. One of these samples is used for composition determination as described in section 4.1.2.

The resulting samples from the experiments at 900 °C can be viewed in figure 4.1. While the surface has changed during the experiments, there has not taken place any optically noticeable crystallisation in the samples during the experiment.

The samples from the experiments at 950 °C can be viewed in figure 4.2.

Two of the samples from the experiments at 1000 °C can be viewed in figure 4.3. The first sample out of the oven was fully crystallized on the outside, so the other samples were allowed to cool to room temperature in the oven.

Figure 4.1: Six samples which have been subjected to 900 °C for differing durations

Figure 4.2: The samples which have been subjected to 950 °C for differing durations.

Figure 4.3: Some of the samples which have been subjected to 1000 °C for differing durations. One of the samples has split open and it can be seen that only the outer shell has fully crystallized, while the core remains glass.

4.2. Numerical experiments

The numerical experiments are conducted with the composition as seen in table 4.3 as an input to the simulation. This composition is chosen by translating the composition from table 4.2 to atomic percentages, removing those small contributions which would result in less than 2 atoms in a 8000 atom simulation, and regrettably also removing the elements for which there are no interatomic potentials given. As these elements are relatively scarce in the composition, and both Magnesium and Iron should act as network formers in this composition, it was deemed acceptable to discard their contribution.

Table 4.3: The composition of the samples as used in the simulation.

Species Name	Concentration (at%)	(rel. at%)
Si	21.67	55.82
Ca	13.71	35.32
Al	2.19	5.65
K	0.45	1.15
Na	0.68	1.72
O	60.92	156.9

The main numerical experiments as described in section 3.2 result in a scatterplot of recognized nucleus sizes during the simulation for each individual simulation. One such scatterplot can be viewed in figure 4.4, where a trend line has been added using linear regression techniques. This image is an indicative example of an inserted nucleus which shrinks in size during the simulation. Do note that the number of atoms referred to in this figure are the amount of Calcium particles which are determined to be 'solid' as described in section 3.2.5. The total amount of atoms in the nucleus is a factor 5 higher than this number.

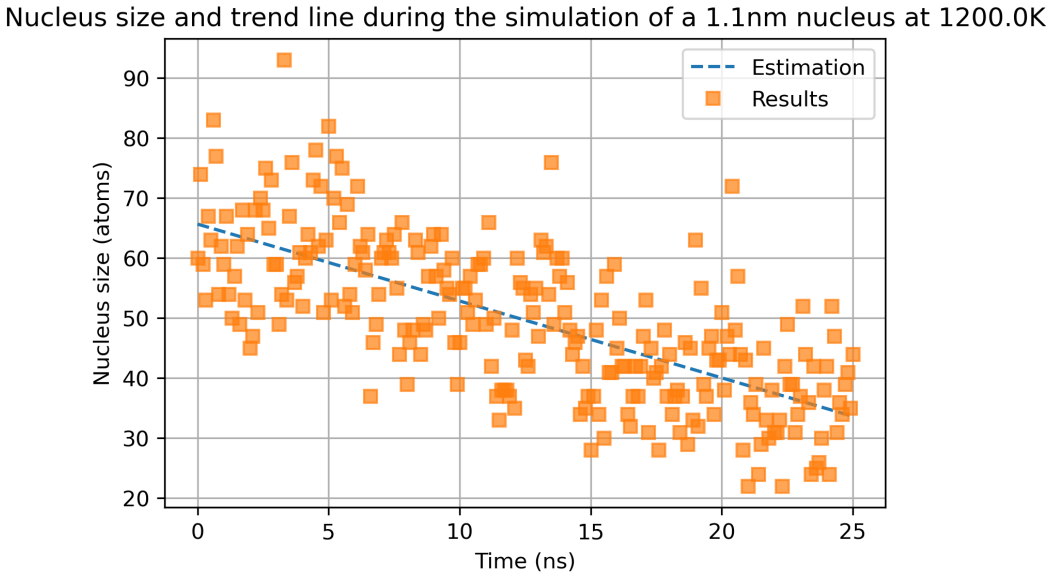

Figure 4.4: A scatterplot of all the sampled nucleus sizes during the simulation of an inserted nucleus of 1.1nm at 1200K. A trend line has been added, and it is clear that the trend is downwards.

The full collection of all scatterplots created during the numerical experiments can be viewed in appendix 6.1. Together these results narrow down the critical temperature of the investigated nucleus sizes within a specific range. The ranges found for the different nucleus sizes can be viewed in table 4.4. A linear regression has been made for these values and this results in the graph in figure 4.5. This graph delineates the temperatures at which a nucleus of a certain size is stable, below the line, and unstable,

Table 4.4: The temperature range in which the critical temperature for the nucleus size lies.

Nucleus size	Temperature range
1.9nm	1325K - 1375K
1.6nm	1250K - 1275K
1.3nm	1225K - 1250K
1.1nm	< 1200K

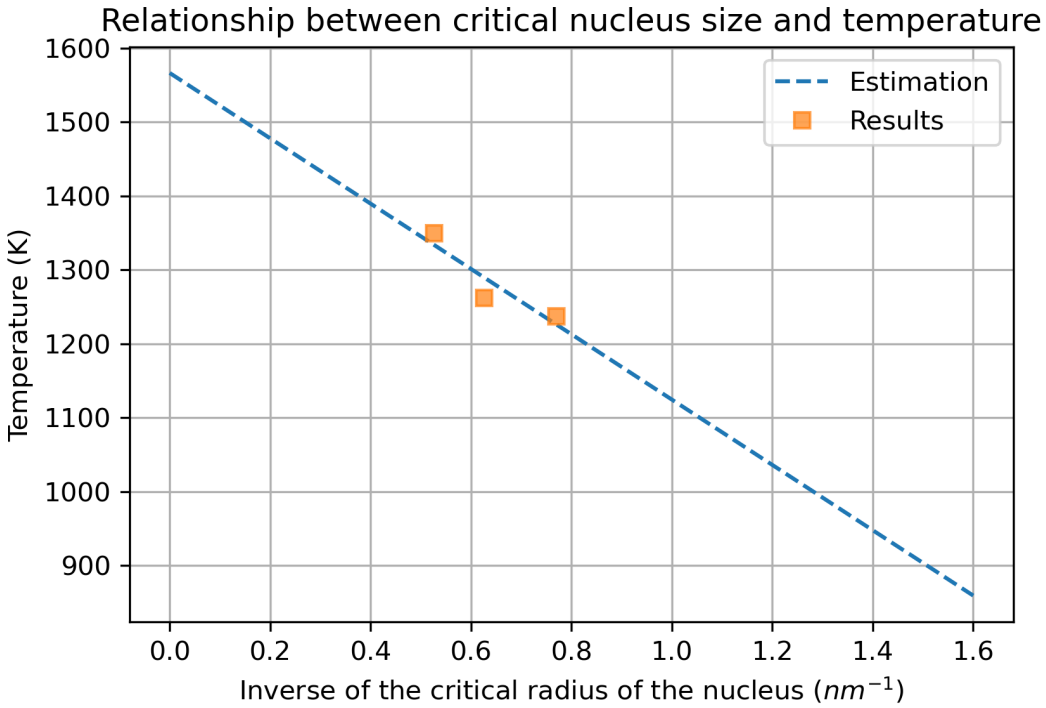

Figure 4.5: The relationship between the temperature and the critical nucleus size, as obtained from the simulations.

above the line. As the line begins at 1293 °C for an inverse radius of 0.0, which means an infinite nucleus size, this means that the melting point for the crystal is 1293 °C. Do note that due to the uncertainty in the critical temperatures for the investigated nucleus sizes this value is also subject to a fair amount of uncertainty.

In order to formulate the TTT diagram, the temperature dependence of the densities and enthalpies of the melt and crystal have been determined. These can be viewed in figures 4.6, 4.7, 4.8 and 4.9. These values, using equation 2.25 and 2.26, are used to obtain the free energy of the melt-crystal interface, and the free energy barrier of the formation of a nucleus of a critical size. This can be viewed in figures 4.10 and 4.11. The attachment rate is calculated using simulations and is shown in figure 4.12, while the nucleation rate, crystal growth rate and the Time-Temperature-Transformation diagram are shown in figures 4.13, 4.14 and 4.15, respectively.

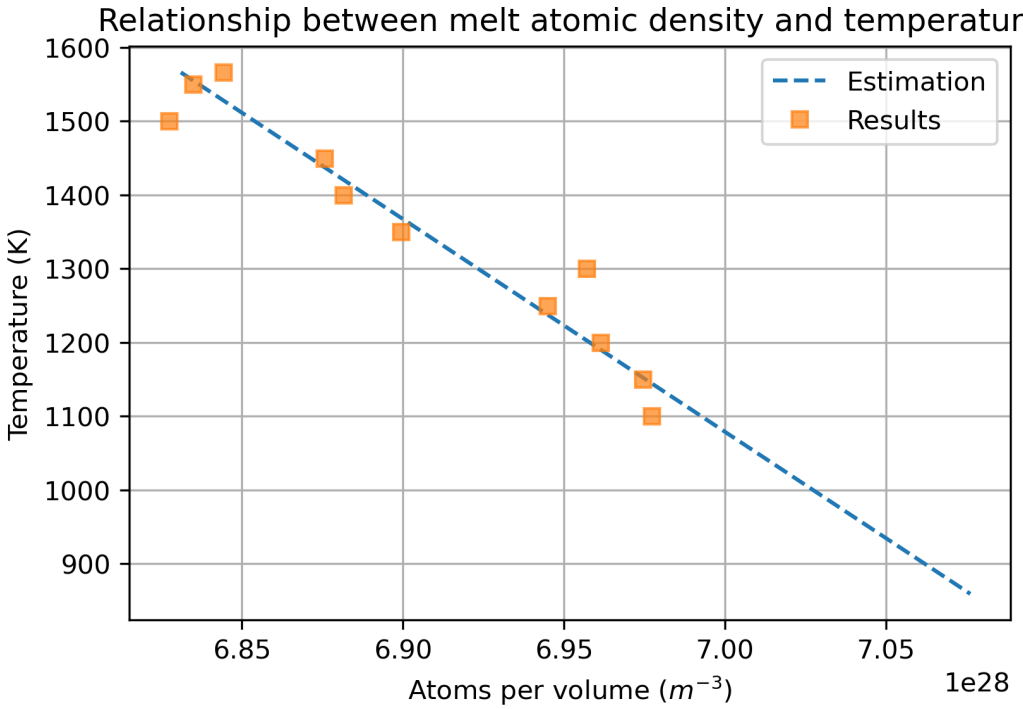

Figure 4.6: The relationship between the temperature and the density of the melt, as obtained from the simulations.

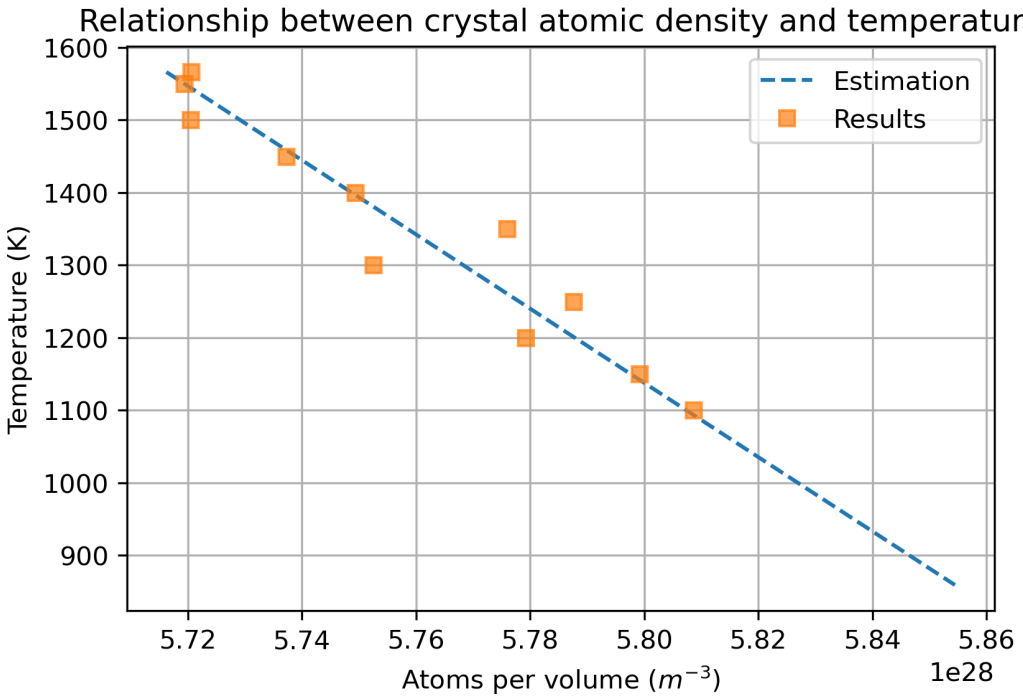

Figure 4.7: The relationship between the temperature and the density of the crystal, as obtained from the simulations.

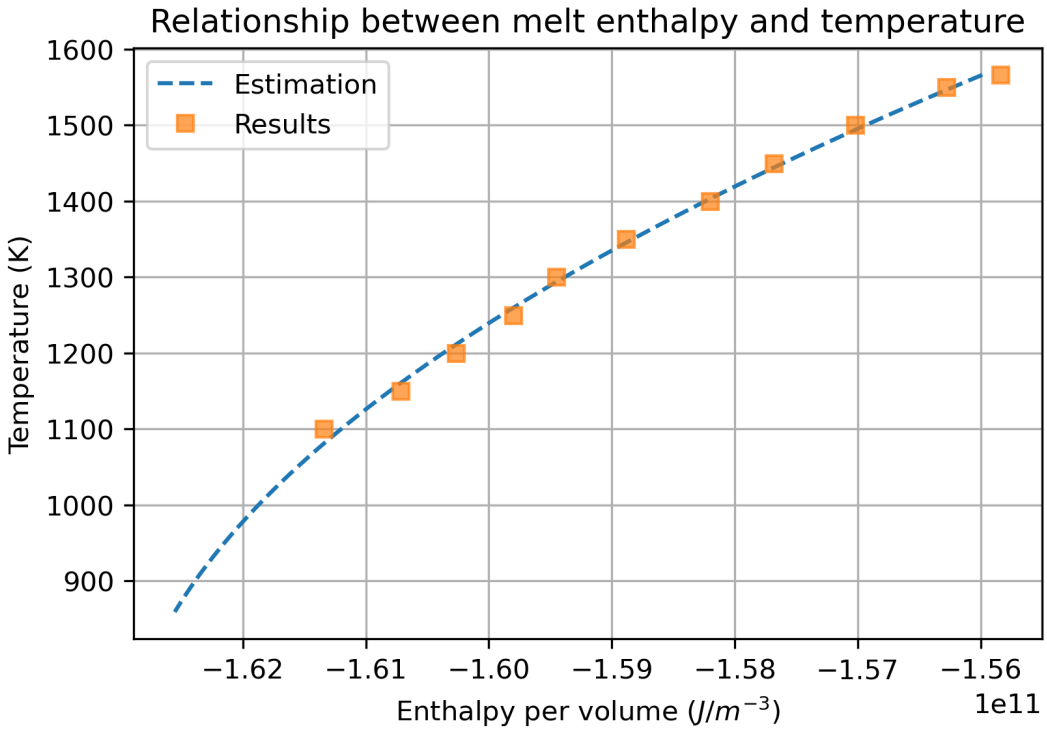

Figure 4.8: The relationship between the temperature and the enthalpy of the melt, as obtained from the simulations.

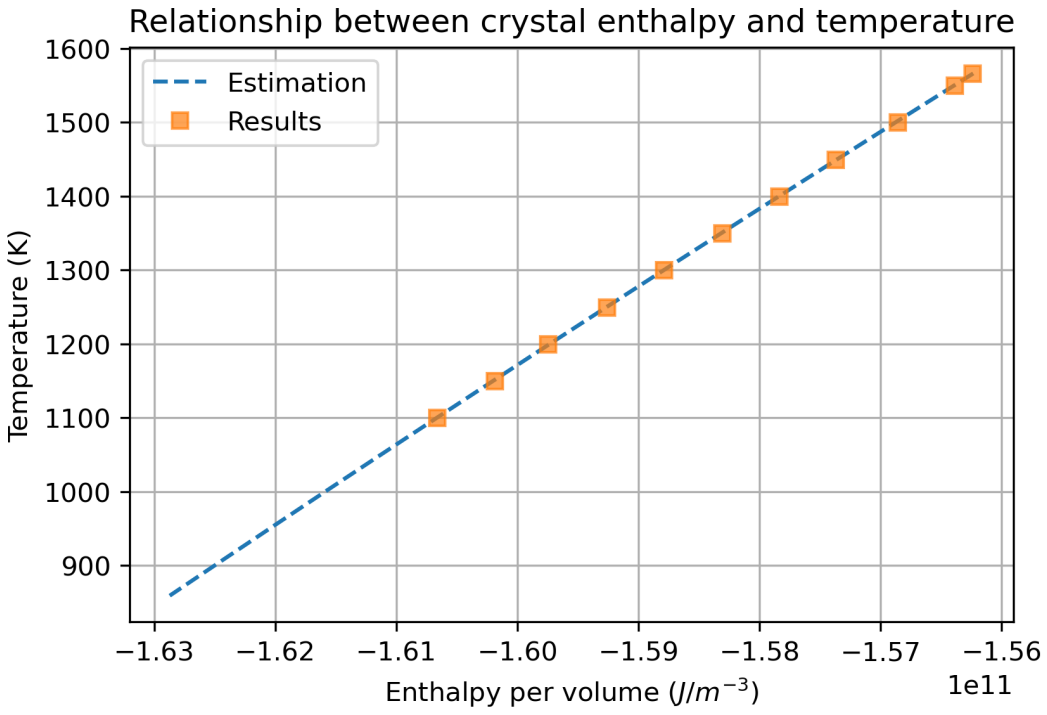

Figure 4.9: The relationship between the temperature and the enthalpy of the crystal, as obtained from the simulations.

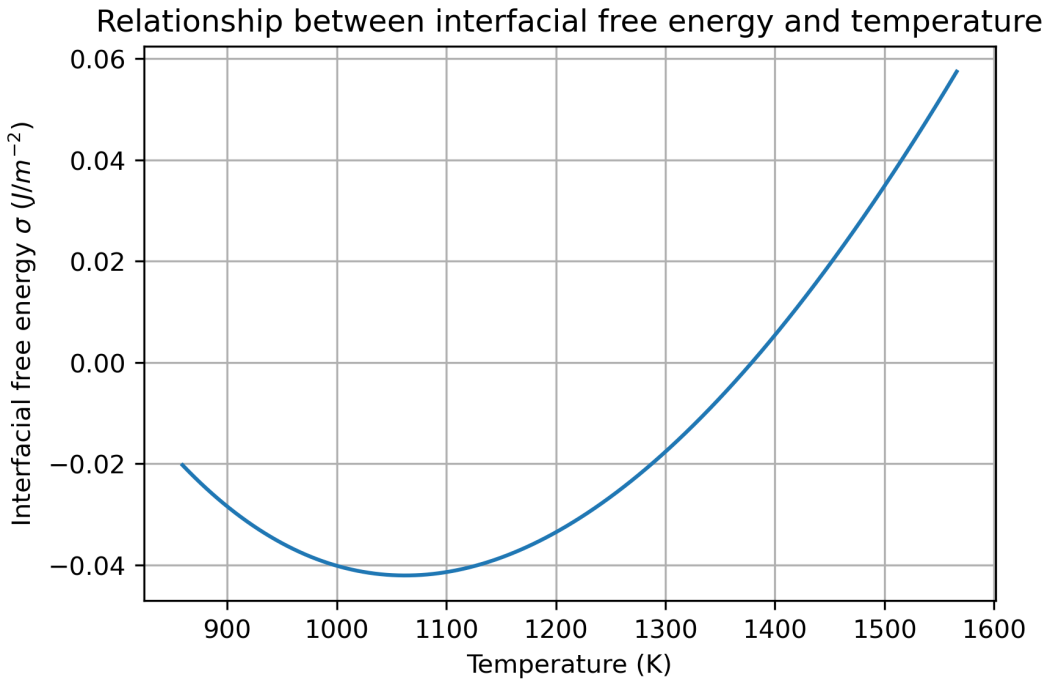

Figure 4.10: The relationship between the temperature and the free energy of the melt-crystal interface, as obtained from the simulations.

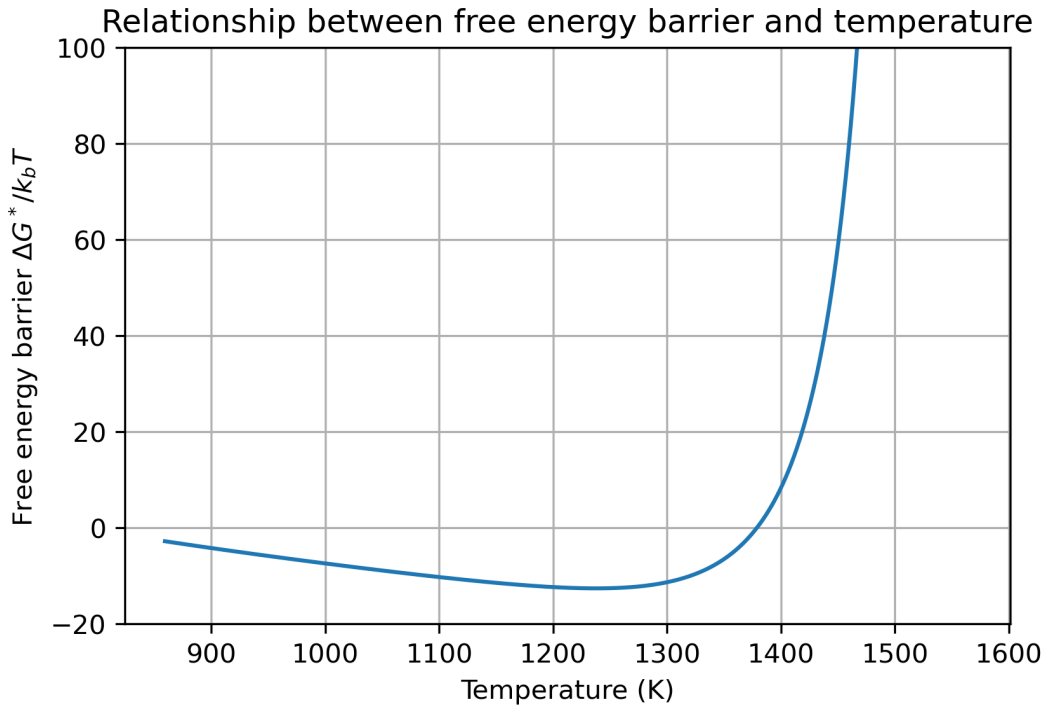

Figure 4.11: The relationship between the temperature and energy barrier for the formation of a nucleus of a critical size, as obtained from the simulations.

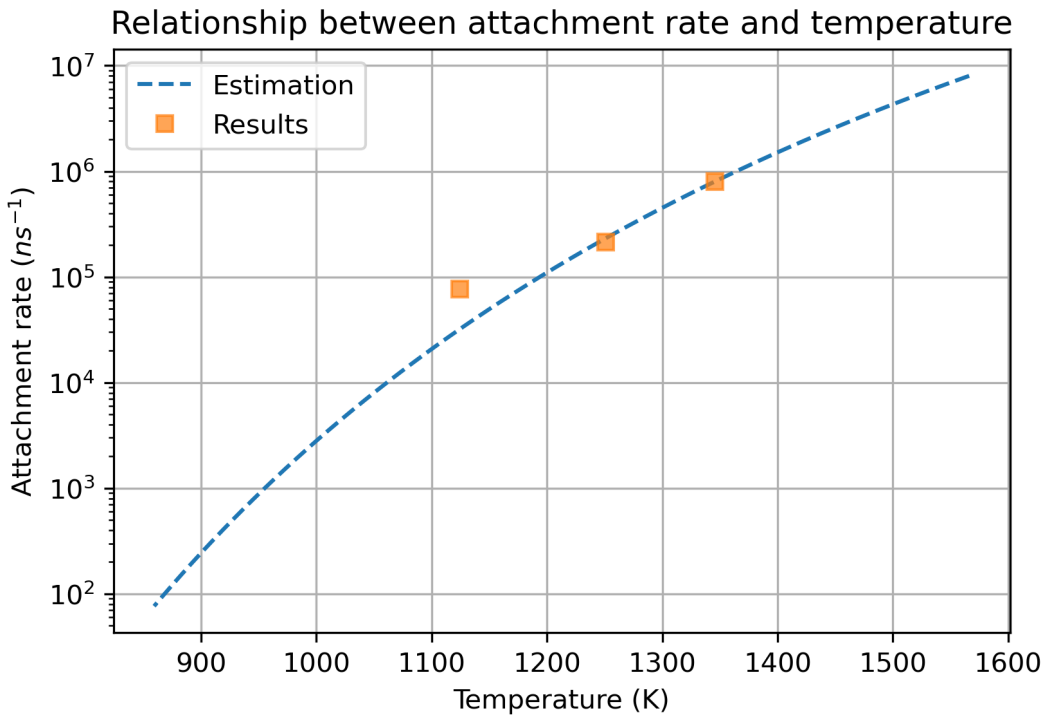

Figure 4.12: The relationship between the temperature and attachment rate of the individual particles, as obtained from the simulations.

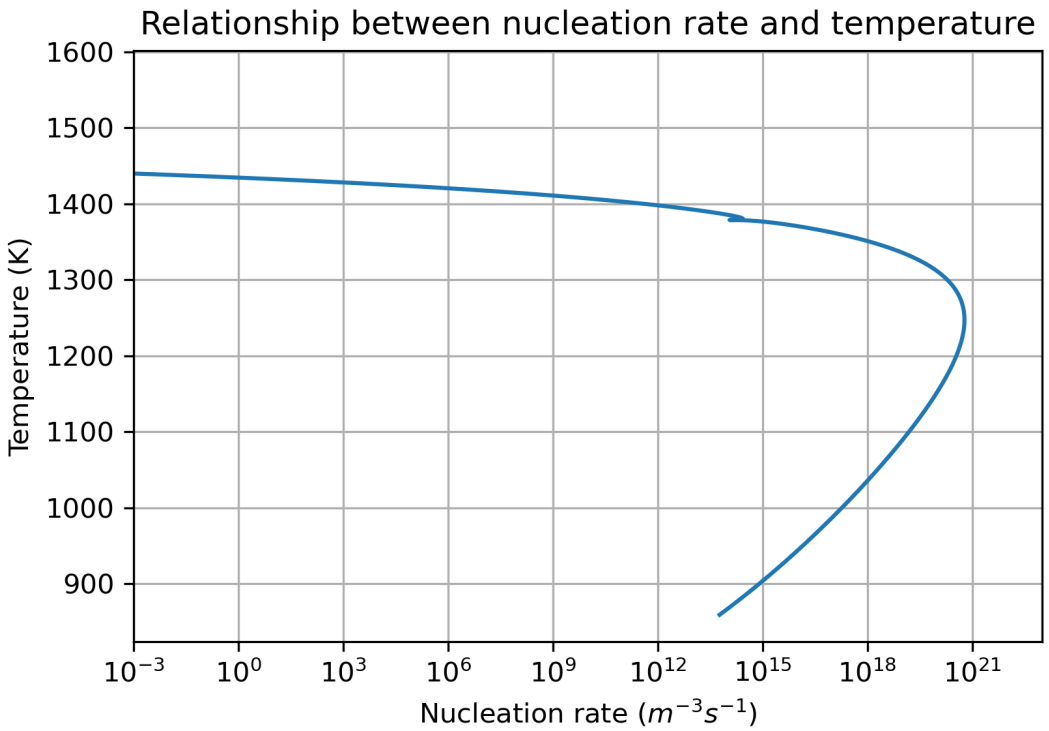

Figure 4.13: The relationship between the temperature and nucleation rate, as obtained from the simulations.

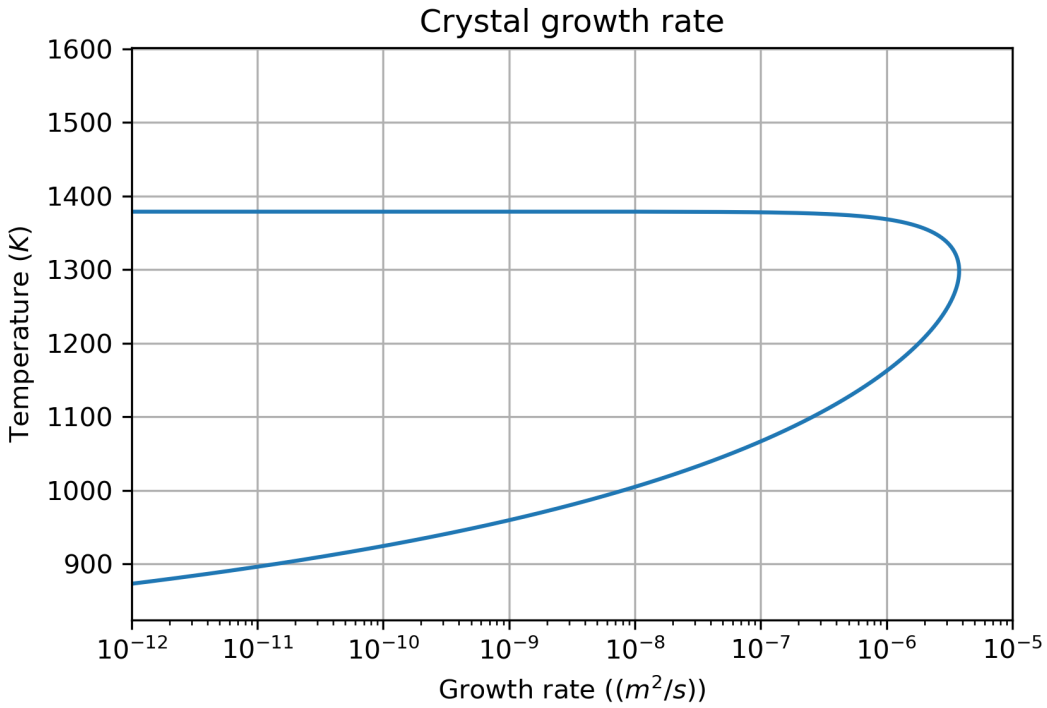

Figure 4.14: The relationship between the temperature and crystalline growth rate, as obtained from the simulations.

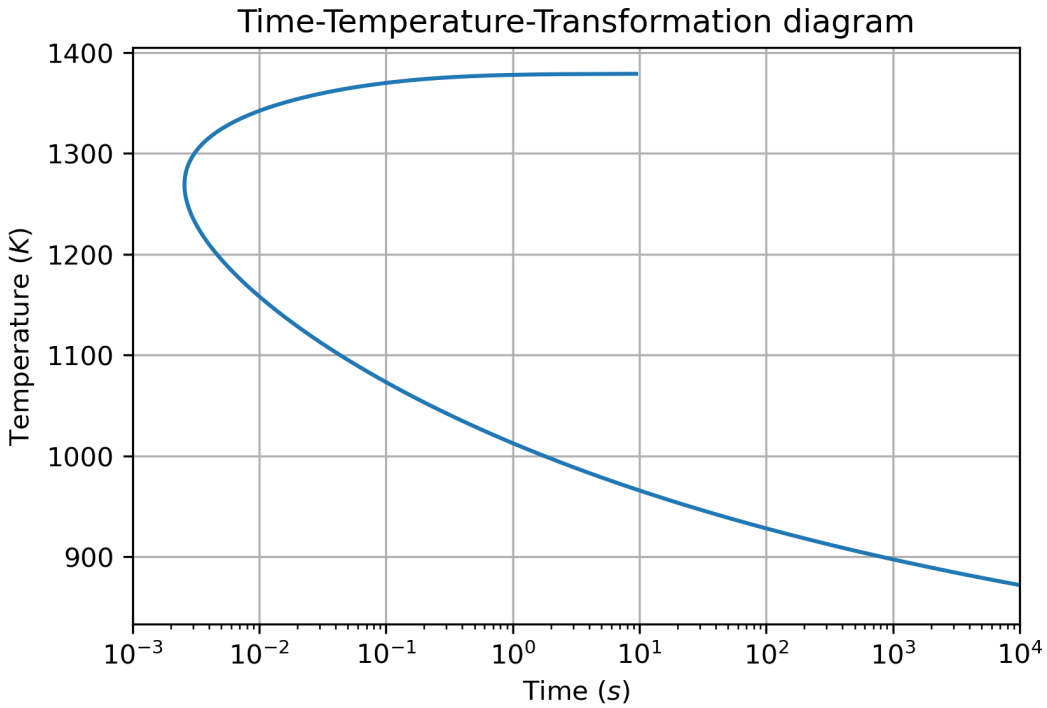

Figure 4.15: The Time-Temperature-Transformation diagram, as obtained from the simulations. The line represents the time until a volume fraction of 1×10^{-6} V/V_0 is crystallized.

5

Discussion

Using the method of molecular dynamics the relationship between the critical nucleus size and the temperature in a glass melt of a specific composition was determined. This could then, in addition with further simulations and information about the viscosity of the melt, be used to construct the temperature dependence of the crystalline growth rate and the nucleation rate. Both of these relations are subsequently used to construct a TTT diagram of the crystallisation of this melt. This TTT diagram has its minimum time to crystallisation, or the 'nose' of the diagram, at 995 °C, which corresponds to a critical cooling rate of 116064 °C/s. The maximum crystalline growth rate is at 1025 °C, while the maximum nucleation rate is at 974 °C.

These diagrams are extremely helpful for the goal of glassmaking from desert sands, as the TTT diagram in particular allows the glassmaker to design for a critical cooling rate in order to prevent crystallisation in the bulk of the glass. However, it is prudent to recognize that these diagrams are the result of a model, and thus it is of great value to determine the uncertainty of these results. The critical cooling rate for example is extremely high and deemed not realistic due to experience with the creation of the samples used in this work. Therefore the several steps in the creation of these diagrams are to be discussed.

The heart of the MD simulations are the interatomic potential functions between the different species. These determine the behavior of the species, and thus are vital to the validity of the results. The chosen set of potential functions[69] include a wide gamut of elements, however they do not include every element that is present in the feedstock which composition can be viewed in table 4.2. The major elements which are not able to be represented in the simulation are Magnesium and Iron, in addition to the minor elements such as Titanium, Chromium and Manganese. The simulated composition (table 4.3) is thus slightly different than the reference material. The assumption is made that the major missing species act in this composition as network formers, and their impact on the homogeneous crystallisation behavior is therefore negligible as these species do not have a profound impact on the viscosity. The difference between the homogeneous crystallisation behavior of the composition used in the simulations and in the physical experiments are thus insignificant.

The determination of the size of the nucleus during the simulation is, as seen in figure 4.4, not exact. There is a significant variation in the exact determination of the size of the nucleus during the simulation. This necessitates a longer simulation time in order to extract a trend from the noise in the determination. This noise is to be expected as the Wollastonite crystal has a unit cell containing 30 individual atoms, and has the limited symmetry of the P-1 space group. The current state of the art in recognizing crystalline structures is limited to cubic, BCC, FCC and HCP crystalline structures, with only recently foraying into ionic materials (see section 2.4.4). In this context it is commending that the method as described in this work functions as well as it does. This thus has the drawback of necessitating a

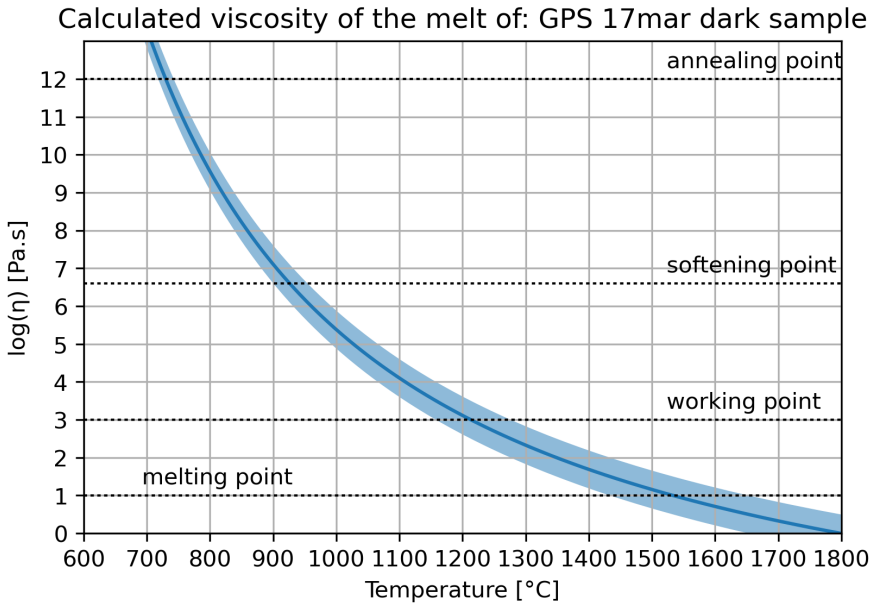

Figure 5.1: The viscosity of the material, as calculated by the method of Giordano[45].

longer simulation time in order to determine the trend of the size change of the nucleus. However, the size recognition algorithm is also used in the determination of the attachment rate, which due to the way this algorithm is used makes the resulting attachment rate highly suspect. The attachment rate is subsequently used to determine the nucleation rate, which as an extension also makes the nucleation rate suspect. The attachment rate is therefore a major contributor to the extremely high critical cooling rate.

Another factor which increases the simulation time is the viscosity of the melt. As can be seen in figure 5.1, the softening point is around 930 °C, which means that below that temperature the growth or shrinkage of the nucleus is severely hampered by the viscosity. As a result of this, if the critical temperature of a certain size nucleus lies below this temperature, it will become impractical to use determine the trend of the size of the nucleus due to the hampered diffusion. Therefore, when looking at fig 4.5, it is only practical to determine the critical temperatures of nucleus sizes 1.2nm and up. This made it impossible to determine the critical temperature of the nucleus size of 1.1nm. Larger nucleus sizes naturally require larger simulation boxes and thus a larger amount of particles, which will increase the computational load required to determine these critical temperatures. It is not possible to determine the minimum practical to be investigated nucleus size in advance, thus it is important to adjust the to be investigated sizes during the simulations.

A curious result, which can best be seen in figure 5.2, is that there appears to be some kind of oscillation present in the simulation which affect the crystalline detection algorithm. As there is a time factor involved in this phenomenon, its cause must lie within the simulation itself as opposed to in the external nucleus size detection algorithm. The direct cause is unclear at this moment. No corresponding oscillation in the system volume, temperature or pressure has been detected. One hypothesis that it could be attributed to the nucleus crossing the boundary of the (periodic) simulation box has been disproven. When visualizing the Calcium particles using a snapshot taken during a peak and a through of the oscillation the Calcium particles do not appear to be in a significantly different position which explains the difference in recognition. It is assumed that phonon interactions influence the detection algorithm by changing the structure of the surrounding oxygen atoms. As of writing no explanation has been verified for this problem. Regardless, this oscillation necessitates extended simulations as the initial direction of the graph is not a sufficient indication for the overall trend for the size of the nucleus.

The lead phenomenon simulated in the numerical experiments is the homogeneous nucleation in the

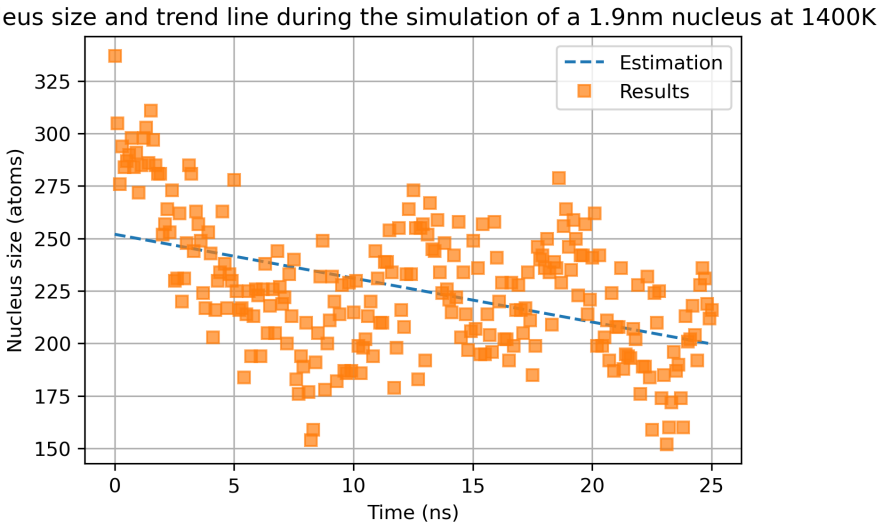

Figure 5.2: A scatterplot of all the sampled nucleus sizes during the simulation of an inserted nucleus of 1.9nm at 1400K. A trend line has been added, and it is clear that the trend is downwards. A kind of oscillation is visible in the data.

glass melt. And while the literature indicated that the homogeneous nucleation was dominant for a pure CaO-SiO_2 melt[82], it is clear that this is not the case for the composition of the feedstock that is used in the physical experiments. In figures 3.3, 4.2 and 4.3 it can be seen that the crystallisation of these samples start at the surface of the samples and grow outwards. This is more pronounced in figure 3.3, but is still observable in the other samples. The heterogeneous nucleation at the surface of the sample is thus dominant in melts of this composition as opposed to heterogeneous nucleation which was assumed at the beginning of the project. The implications of this is that the values of the nucleation rate as obtained from the simulations are not indicative of the real-life behavior of crystallisation in the glass melt of this composition. This, in addition to the suspect nature of the data for the attachment rate, makes that the nucleation rate and by extension the TTT diagram resultant from this project should only be used to gain a qualitative understanding of the nucleation behavior as opposed to a quantitative understanding. If the attachment rate were to be reliable then only a constant has to be determined in order to attain the heterogeneous nucleation rate. This is since in the classical nucleation theory the heterogeneous nucleation rate is exactly a factor C higher than the homogeneous nucleation rate. However with the uncertainty around the attachment rate this determination becomes impossible as the attachment rate is dependent on the temperature and not a simple constant. This makes the nucleation rate resultant from this work not indicative of the real world process. In contrast, the crystalline growth rate resultant from this work does not have these limitations and should be a quantitative indication of the real world crystallisation behavior.

The physical experiments as described in section 4.1.3 result in the the information that the peak of the crystalline growth rate is above 950 °C. Looking at sample 9 in figure 4.2, the lower left edge without much crystallisation is the edge that was previously internal material, as larger samples were broken into smaller pieces in order to generate a higher number of samples. During the experiment, the material sagged and in this particular sample the edge which was thus previously internal to the material was pushed outwards. This edge has a lower density of crystallized material, which means that the samples had pre-existing crystal nucleii on the surface when starting this experiment. It is thus only possible to evaluate the crystalline growth rate using these experiments, as the nucleation rate is skewed due to the pre-existing nucleii. Nonetheless, as the crystalline growth rate is higher at 950 °C as opposed to 900 °C, and it is higher at 1000 °C as opposed to 950 °C, it can be concluded that the peak of the crystalline growth rate is higher than 950 °C, as it is uncertain whether 1000 °C is above or below the peak.

Overall the method described in this work is an attractive method for obtaining information on the region of largest crystal growth in a glass melt. Unfortunately only qualitative data on the total process is

obtainable, due to heterogeneous nucleation taking place and the large uncertainty in the attachment rate. Nevertheless this work can be a valuable tool in a R&D department for feasibility studies into glassmaking recipes.

6

Conclusion

Using a glass composition gained from an XRF investigation, in addition to knowledge into the dominant crystalline phase first formed at that composition, it is possible to obtain qualitative information about the crystallisation behavior of the Calcium rich glass. This work results in the temperature dependence of the crystalline growth rate, the nucleation rate, and the total crystallisation rate in the form of a Time-Temperature-Transformation diagram. The non-crystallisation temperature for $Si_{0.217}Ca_{0.137}Al_{0.022}K_{0.004}Na_{0.007}O_{0.609}$ is 1293 °C and the critical cooling rate is 116064 °C/s.

Unfortunately due to challenges in the process of discerning the dominant crystalline phase for the researched composition, Wollastonite, from the glass melt, only the data on the growth rate of the crystalline phase can be used quantitatively. In addition to the challenge in differentiating between melt and crystal, the applied seeding method results in predictions which are valid for homogeneous nucleation. Physical experiments have shown that in fact heterogeneous nucleation is valid for the composition of the glass melt of the given composition. The result of this is that the resultant nucleation rate and the Time-Temperature-Transformation diagram can only be used to gain a qualitative understanding of the crystallisation behavior of the glass of the given composition.

6.1. Suggestions for future research

The following recommendations can be made when continuing this work:

- Investigate the source of the oscillations in the detected nucleus sizes
- Continue this work with larger inserted nucleus sizes
- Improve the Wollastonite detection algorithm
- Repeat this work with a composition with a simpler primary crystalline phase
- Repeat this work with a composition for which nucleation and crystal growth data are known

When continuing this work in the direction of the same or similar compositions, it is recommended to investigate the source of the oscillations happening in the size detection during the simulation. If found and accounted for, the computational load for the project can be decreased, as less simulation time will be needed in order to positively determine the trend in the size of the nucleus. It could also be valuable to research if the attachment rate could be inferred using an alternative method, perhaps even one which is dependent on the viscosity of the melt.

In addition to this, larger nucleus sizes could be investigated in order to gain a more robust prediction of the critical temperature - nucleus size relationship. This is in order to more positively limit the range of the slope of the temperature-critical radius graph, as spacing the values far apart would result in a predicted slope with a lower angular uncertainty than values spaced close together. This increases the computational load since the larger nucleii would necessitate larger system sizes, however this might be offset due to a lower viscosity at the higher temperatures lowering the simulation time required for attaining a conclusive result in terms of the trend of the nucleus size.

An additional avenue of research is to improve the detection algorithm of the Wollastonite crystal. It has been shown that the described method is somewhat successful at detecting the majority of the Calcium atoms within the inserted nucleus. However, this method had no information on the full Wollastonite crystalline structure. It could be that a method based on 3d pattern matching could work when supplied with the structure of a Wollastonite crystal. If successful and performant, this could subsequently be a more general basis for compositions with different crystalline phases that form. Alternatively, the current approach of Steinhardt order parameters of nearest neighbours could be extended to second and third nearest neighbours, and subsequently trained on recognizing the Wollastonite crystal by using machine learning algorithms. Nevertheless, this work would be enhanced by an improvement in the crystal size detection algorithm.

If this work is continued in a direction of different compositions, it would be valuable to continue it in the direction of a composition where there are preexisting physical experiments which have resulted in a TTT diagram. This is very valuable in the validation of the results of such a work. If it is remotely possible, a composition with a primary crystalline phase that has a higher symmetry of the crystal, and perhaps a lower amount of atoms in the unit cell, could be beneficial to a more accurate detection algorithm in comparison to the one in this work.

References

[1] J. E. Shelby, *Introduction to Glass Science and Technology* (EngineeringPro collection). Royal Society of Chemistry, 2005, ISBN: 9780854046393.

[2] J. F. Stebbins, "Short-range structure and order in oxide glasses," in *Encyclopedia of Glass Science, Technology, History, and Culture*. John Wiley & Sons, Ltd, 2021, ch. 2.4, pp. 173–181, ISBN: 9781118801017. DOI: 10.1002/9781118801017.ch2.4.

[3] Isaac Newton, *Opticks, or A treatise of the Reflections, Refractions, Inflexions and Colours of Light*, First edition. The Royal Society of London for Improving Natural Knowledge, 1704.

[4] C. Kurkjian and W. Prindle, "Perspectives on the history of glass composition," *Journal of the American Ceramic Society*, vol. 81, pp. 795–813, Jan. 2005. DOI: 10.1111/j.1151-2916.1998.tb02415.x.

[5] O. Schott, *Glasschmelzerei für optische und andere wissenschaftliche Zwecke*. Glastechnisches Laboratorium Schott & Genossen, Jena, Jul. 1886.

[6] J. T. Randall, H. P. Rooksby, and B. S. Cooper, "X-ray diffraction and the structure of vitreous solids," *Zeitschrift für Kristallographie - Crystalline Materials*, vol. 75, no. 1, pp. 196–214, 1930. DOI: 10.1515/zkri-1930-0114.

[7] H. Jeffreys, "On the structure of liquids and vitreous solids," *Mathematical Proceedings of the Cambridge Philosophical Society*, vol. 24, no. 1, pp. 19–31, 1928. DOI: 10.1017/S0305004100011804.

[8] W. H. Zachariasen, "The atomic arrangement in glass," *Journal of the American Chemical Society*, vol. 54, no. 10, pp. 3841–3851, 1932. DOI: 10.1021/ja01349a006.

[9] B. E. Warren, "X-ray diffraction of vitreous silica," *Zeitschrift für Kristallographie - Crystalline Materials*, vol. 86, no. 1-6, pp. 349–358, 1933. DOI: 10.1524/zkri.1933.86.1.349.

[10] B. E. Warren and J. Biscce, "The structure of silica glass by x-ray diffraction studies *," *Journal of the American Ceramic Society*, vol. 21, no. 2, pp. 49–54, 1938. DOI: 10.1111/j.1151-2916.1938.tb15742.x.

[11] L. Lichtenstein, M. Heyde, and H.-J. Freund, "Atomic arrangement in two-dimensional silica: From crystalline to vitreous structures," *The Journal of Physical Chemistry C*, vol. 116, pp. 20 426–20 432, Sep. 2012. DOI: 10.1021/jp3062866.

[12] L. Lichtenstein, M. Heyde, and H.-J. Freund, "Crystalline-vitreous interface in two dimensional silica," *Phys. Rev. Lett.*, vol. 109, p. 106 101, 10 Sep. 2012. DOI: 10.1103/PhysRevLett.109.106101.

[13] D. L. Evans and S. V. King, "Random network model of vitreous silica," *Nature*, vol. 212, no. 5068, pp. 1353–1354, Dec. 1966, ISSN: 1476-4687. DOI: 10.1038/2121353a0.

[14] J. Rino, I. Ebbsjö, R. Kalia, A. Nakano, and P. Vashishta, "Structure of rings in vitreous sio2," *Phys. Rev. B*, vol. 47, Feb. 1993. DOI: 10.1103/PhysRevB.47.3053.

[15] H. Jabraoui, E. Achhal, A. Hasnaoui, J.-L. Garden, Y. Vaills, and S. Ouaskit, "Molecular dynamics simulation of thermodynamic and structural properties of silicate glass: Effect of the alkali oxide modifiers," *Journal of Non-Crystalline Solids*, vol. 448, p. 16, Jun. 2016. DOI: 10.1016/j.jnoncrysol.2016.06.030.

[16] B. M. Al-Hasni and G. Mountjoy, "A molecular dynamics study of the atomic structure of x(mgo) 100−x(sio2)," *Journal of Non-Crystalline Solids*, vol. 400, pp. 33–44, 2014. DOI: 10.1016/j.jnoncrysol.2013.11.011.

[17] B. E. Warren, “Summary of work on atomic arrangement in glass,” *Journal of the American Ceramic Society*, vol. 24, no. 8, pp. 256–261, 1941. DOI: 10.1111/j.1151-2916.1941.tb14858.x.

[18] A. Lebedev, “On the polymorphism and annealing of glass,” *Trudy Gos. Opt. Inst*, vol. 2, pp. 1–20, 1921.

[19] N. Valenkov and E. Poray-Koshitz, “X-ray investigation of the glassy state,” *Zeitschrift für Kristallographie - Crystalline Materials*, vol. 95, no. 1-6, pp. 195–229, 1936. DOI: 10.1524/zkri.1936.95.1.195.

[20] Z.-H. Jiang and Q.-Y. Zhang, “The structure of glass: A phase equilibrium diagram approach,” *Progress in Materials Science*, vol. 61, pp. 144–215, 2014, ISSN: 0079-6425. DOI: 10.1016/j.pmatsci.2013.12.001.

[21] V. M. Goldschmidt, *Geochemische Verteilungsgesetze der Elemente* (Mathematisk- naturvidenskabelig 137). Skrifter Norske Videnskaps Akademi i Oslo, 1926, vol. 8.

[22] A. Dietzel, “Die kationenfeldstärken und ihre beziehungen zu entglasungsvorgängen, zur verbindungsbildung und zu den schmelzpunkten von silicaten,” *Zeitschrift für Elektrochemie und angewandte physikalische Chemie*, vol. 48, no. 1, pp. 9–23, 1942. DOI: 10.1002/bbpc.19420480104.

[23] W. Vogel, “The development of the classical structure theories,” in *Structure and Crystallization of Glasses*, W. VOGEL, Ed., Pergamon, 1971, pp. 14–20. DOI: 10.1016/B978-0-08-006998-2.50005-0.

[24] “Chapter 4 - melt and glass structure: Basic concepts,” in *Silicate Glasses and Melts*, ser. Developments in Geochemistry, B. Mysen and P. Richet, Eds., vol. 10, Elsevier, 2005, pp. 101–129. DOI: 10.1016/S0921-3198(05)80024-9.

[25] B. H. W. S. De Jong, C. M. Schramm, and V. E. Parziale, “Silicon-29 magic angle spinning nmr study on local silicon environments in amorphous and crystalline lithium silicates,” *Journal of the American Chemical Society*, vol. 106, no. 16, pp. 4396–4402, 1984. DOI: 10.1021/ja00328a018.

[26] A. K. Varshneya and J. C. Mauro, “Glass formation principles,” in *Fundamentals of Inorganic Glasses (Third Edition)*, A. K. Varshneya and J. C. Mauro, Eds., Third Edition, Elsevier, 2019, pp. 37–69, ISBN: 978-0-12-816225-5. DOI: 10.1016/B978-0-12-816225-5.00003-1.

[27] C. Chattopadhyay, K. S. N. S. Idury, J. Bhatt, K. Mondal, and B. S. Murty, “Critical evaluation of glass forming ability criteria,” *Materials Science and Technology*, vol. 32, no. 4, pp. 380–400, 2016. DOI: 10.1179/1743284715Y.0000000104.

[28] J. Dantzig and M. Rappaz, *Solidification* (Engineering sciences). Taylor & Francis Group, 2009, ISBN: 9782940222179.

[29] D. Turnbull and M. D. Cohen, “Modern aspects of the vitreous state,” in J. D. Mackenzie, Ed., vol. 1st, Butterworths, London, 1960, pp. 38–62.

[30] L. Gránásy and D. M. Herlach, “Diffuse interface approach to crystal nucleation in glasses,” *Journal of Non-Crystalline Solids*, vol. 192-193, pp. 470–473, 1995, Structure of Non-Crystalline Materials 6, ISSN: 0022-3093. DOI: 10.1016/0022-3093(95)00430-0.

[31] L. Gránásy and P. James, “Nucleation in oxide glasses: Comparison of theory and experiment,” *Proceedings of The Royal Society A: Mathematical, Physical and Engineering Sciences*, vol. 454, pp. 1745–1766, Jun. 1998. DOI: 10.1098/rspa.1998.0230.

[32] M. Kowalski, P. J. Spencer, and D. Neuschütz, “Phase diagrams,” in *Slag Atlas*, Verein Deutscher Eisenhüttenleute, Ed., 2nd edition, Verlag Stahleisen, 1995, ch. 3, p. 63, ISBN: 3-514-00457-9.

[33] S. G. Brush, “Theories of liquid viscosity.,” *Chemical Reviews*, vol. 62, no. 6, pp. 513–548, 1962. DOI: 10.1021/cr60220a002.

[34] D. S. Viswanath, T. Ghosh, D. Prasad, N. Dutt, and K. Y. Rani, *Viscosity of Liquids: Theory, Estimation, Experiment, and Data*. Springer Dordrecht, Jan. 2007, pp. 163–176. DOI: 10.1007/978-1-4020-5482-2.

[35] R. Barrer, “The viscosity of pure liquids. ii. polymerised ionic melts,” *Transactions of the Faraday Society*, vol. 39, pp. 59–67, 1943.

[36] P. Hrma, “Arrhenius model for high-temperature glass-viscosity with a constant pre-exponential factor,” *Journal of Non-Crystalline Solids*, vol. 354, no. 18, pp. 1962–1968, 2008, ISSN: 0022-3093. DOI: 10.1016/j.jnoncrysol.2007.11.016.

[37] C. T. Moynihan and S. Cantor, “Viscosity and its temperature dependence in molten bef2,” *The Journal of Chemical Physics*, vol. 48, no. 1, pp. 115–119, 1968. DOI: 10.1063/1.1664455.

[38] H. Vogel, “Das temperaturabhaengigkeitsgesetz der viskositaet von fluessigkeiten,” *Physikalische Zeitschrift*, vol. 22, p. 645, 1921.

[39] G. S. Fulcher, “Analysis of recent measurements of the viscosity of glasses,” *Journal of the American Ceramic Society*, vol. 8, no. 6, pp. 339–355, 1925. DOI: 10.1111/j.1151-2916.1925.tb16731.x.

[40] G. Tammann and W. Hesse, “Die abhängigkeit der viscosität von der temperatur bie unterkühlten flüssigkeiten,” *Zeitschrift für anorganische und allgemeine Chemie*, vol. 156, no. 1, pp. 245–257, 1926. DOI: 10.1002/zaac.19261560121.

[41] P. Hrma and A. A. Kruger, “High-temperature viscosity of many-component glass melts,” *Journal of Non-Crystalline Solids*, vol. 437, pp. 17–25, 2016, ISSN: 0022-3093. DOI: 10.1016/j.jnoncrysol.2016.01.007.

[42] I. Avramov and A. Milchev, “Effect of disorder on diffusion and viscosity in condensed systems,” *Journal of Non-Crystalline Solids*, vol. 104, no. 2, pp. 253–260, 1988, ISSN: 0022-3093. DOI: 10.1016/0022-3093(88)90396-1.

[43] G. Adam and J. H. Gibbs, “On the temperature dependence of cooperative relaxation properties in glass-forming liquids,” *The Journal of Chemical Physics*, vol. 43, no. 1, pp. 139–146, 1965. DOI: 10.1063/1.1696442.

[44] J. C. Mauro, Y. Yue, A. J. Ellison, P. K. Gupta, and D. C. Allan, “Viscosity of glass-forming liquids,” *Proceedings of the National Academy of Sciences*, vol. 106, no. 47, pp. 19 780–19 784, 2009. DOI: 10.1073/pnas.0911705106.

[45] D. Giordano, J. K. Russell, and D. B. Dingwell, “Viscosity of magmatic liquids: A model,” *Earth and Planetary Science Letters*, vol. 271, no. 1, pp. 123–134, 2008, ISSN: 0012-821X. DOI: 10.1016/j.epsl.2008.03.038.

[46] C. Angell, “Spectroscopy simulation and scattering, and the medium range order problem in glass,” *Journal of Non-Crystalline Solids*, vol. 73, no. 1, pp. 1–17, 1985, Glass Science and Technology Problems and Prospects for 2004, ISSN: 0022-3093. DOI: 10.1016/0022-3093(85)90334-5.

[47] W. A. Johnson and K. E. Mehl, “Reaction kinetics in processes of nucleation and growth,” *ransactions of the American Institute of Mining, Metallurgical and Petroleum Engineers*, no. 135, p. 416, 1939.

[48] M. Avrami, “Kinetics of phase change. i general theory,” *The Journal of Chemical Physics*, vol. 7, no. 12, pp. 1103–1112, 1939. DOI: 10.1063/1.1750380.

[49] M. Avrami, “Granulation, phase change, and microstructure kinetics of phase change. iii,” *The Journal of Chemical Physics*, vol. 9, no. 2, pp. 177–184, 1941. DOI: 10.1063/1.1750872.

[50] M. Frey *et al.*, “Determining and modelling a complete time-temperature-transformation diagram for a pt-based metallic glass former through combination of conventional and fast scanning calorimetry,” *Scripta Materialia*, vol. 215, p. 114 710, 2022, ISSN: 1359-6462. DOI: 10.1016/j.scriptamat.2022.114710.

[51] D. R. Uhlmann, P. I. K. Onorato, and G. W. Scherer, “A simplified model for glass formation.,” *Lunar and Planetary Science Conference Proceedings*, vol. 1, pp. 375–381, Jan. 1979.

[52] B. Karmakar, “Chapter 1 - fundamentals of glass and glass nanocomposites,” in *Glass Nanocomposites*, B. Karmakar, K. Rademann, and A. L. Stepanov, Eds., Boston: William Andrew Publishing, 2016, pp. 3–53, ISBN: 978-0-323-39309-6. DOI: 10.1016/B978-0-323-39309-6.00001-8.

[53] E. Davenport and E. Bain, “Transformation of austenite at constant subcritical temperatures,” *American Institute of Mining & Metallurgical Engineers*, vol. 348, 1930.

[54] M. Hillert, “Discussion of “a personal commentary on transformation of austenite at constant subcritical temperatures”,” *Metallurgical and Materials Transactions*, vol. 42, no. 3, pp. 541–542, Mar. 2011, ISSN: 1543-1940. DOI: 10.1007/s11661-010-0586-7.

[55] H. W. Paxton and J. B. Austin, “Historical account of the contributions of E. C. Bain,” *Metallurgical Transactions*, vol. 3, pp. 1035–1042, 1972.

[56] M. Rusiecka, M. Bilodeau, and D. Baker, “Quantification of nucleation delay in magmatic systems: Experimental and theoretical approach,” *Contributions to Mineralogy and Petrology*, vol. 175, Apr. 2020. DOI: 10.1007/s00410-020-01682-4.

[57] W.-K. Rhim *et al.*, “An electrostatic levitator for high-temperature containerless materials processing in 1-g,” *Review of Scientific Instruments*, vol. 64, no. 10, pp. 2961–2970, 1993. DOI: 10.1063/1.1144475.

[58] Y. J. Kim, R. Busch, W. L. Johnson, A. J. Rulison, and W. K. Rhim, “Experimental determination of a time–temperature-transformation diagram of the undercooled zr41.2ti13.8cu12.5ni10.0be22.5 alloy using the containerless electrostatic levitation processing technique,” *Applied Physics Letters*, vol. 68, no. 8, pp. 1057–1059, 1996. DOI: 10.1063/1.116247.

[59] C. C. Hays *et al.*, “Vitrification and determination of the crystallization time scales of the bulk-metallic-glass-forming liquid zr58.5nb2.8cu15.6ni12.8al10.3,” *Applied Physics Letters*, vol. 79, no. 11, pp. 1605–1607, 2001. DOI: 10.1063/1.1398605.

[60] Rigaku Corporation. “High-temperature dsc.” (2022), [Online]. Available: https://www.rigaku.com/products/thermal/ht-dsc (visited on Oct. 3, 2022).

[61] Linseis Messgeraete GmbH. “Linseis dsc pt 1600: Differential scanning calorimeter.” (2022), [Online]. Available: https://www.linseis.com/en/products/differential-scanning-calorimeter-dsc/dsc-pt-1600/ (visited on Oct. 3, 2022).

[62] E. D. Zanotto and P. F. James, “Experimental tests of the classical nucleation theory for glasses,” *Journal of Non-Crystalline Solids*, vol. 74, no. 2, pp. 373–394, 1985, ISSN: 0022-3093. DOI: 10.1016/0022-3093(85)90080-8.

[63] L. Cormier, “Nucleation in glasses – new experimental findings and recent theories,” *Procedia Materials Science*, vol. 7, pp. 60–71, 2014, 2nd International Summer School on Nuclear Glass Wasteform: Structure, Properties and Long-Term Behavior, SumGLASS 2013, ISSN: 2211-8128. DOI: 10.1016/j.mspro.2014.10.009.

[64] P. Harrowell and D. W. Oxtoby, “A molecular theory of crystal nucleation from the melt,” *The Journal of Chemical Physics*, vol. 80, no. 4, pp. 1639–1646, 1984. DOI: 10.1063/1.446864.

[65] M. Iwamatsu and K. Horii, “A one order parameter theory of crystal-melt nucleation of spherical clusters,” *Journal of the Physical Society of Japan*, vol. 65, no. 7, pp. 2311–2316, 1996. DOI: 10.1143/JPSJ.65.2311.

[66] Y. Sato, C. Nakai, M. Wakeda, and S. Ogata, “Predictive modeling of time-temperature-transformation diagram of metallic glasses based on atomistically-informed classical nucleation theory,” *Scientific Reports*, vol. 7, Dec. 2017. DOI: 10.1038/s41598-017-06482-8.

[67] R. LeSar, *Introduction to Computational Materials Science: Fundamentals to Applications*. Cambridge University Press, 2013. DOI: 10.1017/CBO9781139033398.

[68] A. Pedone, M. Bertani, L. Brugnoli, and A. Pallini, “Interatomic potentials for oxide glasses: Past, present, and future,” *Journal of Non-Crystalline Solids: X*, vol. 15, p. 100 115, 2022, ISSN: 2590-1591. DOI: 10.1016/j.nocx.2022.100115.

[69] J. Du, “Challenges in molecular dynamics simulations of multicomponent oxide glasses,” in *Molecular Dynamics Simulations of Disordered Materials: From Network Glasses to Phase-Change Memory Alloys*, C. Massobrio, J. Du, M. Bernasconi, and P. S. Salmon, Eds. Cham: Springer International Publishing, 2015, pp. 157–180, ISBN: 978-3-319-15675-0. DOI: 10.1007/978-3-319-15675-0_7.

[70] R. Thapa and D. A. Drabold, “Ab initio simulation of amorphous materials,” in *Atomistic Simulations of Glasses*. John Wiley & Sons, Ltd, 2022, ch. 2, pp. 30–59, ISBN: 9781118939079. DOI: 10.1002/9781118939079.ch2.

[71] J. E. Lennard-Jones, “Wave functions of many-electron atoms,” *Mathematical Proceedings of the Cambridge Philosophical Society*, vol. 27, no. 3, pp. 469–480, 1931. DOI: 10.1017/S0305004100010057.

[72] G. Mie, “Zur kinetischen theorie der einatomigen körper,” *Annalen der Physik*, vol. 316, no. 8, pp. 657–697, 1903. DOI: 10.1002/andp.19033160802.

[73] M. L. Huggins and J. E. Mayer, “Interatomic Distances in Crystals of the Alkali Halides,” *The Journal of Chemical Physics*, vol. 1, no. 9, pp. 643–646, Nov. 1933. DOI: 10.1063/1.1749344.

[74] P. M. Morse, “Diatomic molecules according to the wave mechanics. ii. vibrational levels,” *Phys. Rev.*, vol. 34, pp. 57–64, 1 Jul. 1929. DOI: 10.1103/PhysRev.34.57.

[75] R. A. Buckingham and J. E. Lennard-Jones, “The classical equation of state of gaseous helium, neon and argon,” *Proceedings of the Royal Society of London. Series A. Mathematical and Physical Sciences*, vol. 168, no. 933, pp. 264–283, 1938. DOI: 10.1098/rspa.1938.0173.

[76] A. N. Cormack, “Classical simulation methods,” in *Atomistic Simulations of Glasses*. John Wiley & Sons, Ltd, 2022, ch. 1, pp. 1–29, ISBN: 9781118939079. DOI: 10.1002/9781118939079.ch1.

[77] S. Auer and D. Frenkel, “Numerical prediction of absolute crystallization rates in hard-sphere colloids,” *The Journal of Chemical Physics*, vol. 120, no. 6, pp. 3015–3029, Feb. 2004. DOI: 10.1063/1.1638740.

[78] X.-M. Bai and M. Li, “Calculation of solid-liquid interfacial free energy: A classical nucleation theory based approach,” *The Journal of Chemical Physics*, vol. 124, no. 12, p. 124 707, 2006. DOI: 10.1063/1.2184315.

[79] J. R. Espinosa, C. Vega, C. Valeriani, and E. Sanz, “Seeding approach to crystal nucleation,” *The Journal of Chemical Physics*, vol. 144, no. 3, p. 034 501, 2016. DOI: 10.1063/1.4939641.

[80] S. C. C. Prado, J. P. Rino, and E. D. Zanotto, “Successful test of the classical nucleation theory by molecular dynamic simulations of bas,” *Computational Materials Science*, vol. 161, pp. 99–106, 2019, ISSN: 0927-0256. DOI: 10.1016/j.commatsci.2019.01.023.

[81] L. Separdar, J. P. Rino, and E. D. Zanotto, “Molecular dynamics simulations of spontaneous and seeded nucleation and theoretical calculations for zinc selenide,” *Computational Materials Science*, vol. 187, p. 110 124, 2021, ISSN: 0927-0256. DOI: 10.1016/j.commatsci.2020.110124.

[82] E. D. Zanotto, “Isothermal and adiabatic nucleation in glass,” *Journal of Non-Crystalline Solids*, vol. 89, no. 3, pp. 361–370, 1987, ISSN: 0022-3093. DOI: 10.1016/S0022-3093(87)80278-8.

[83] P. J. Steinhardt, D. R. Nelson, and M. Ronchetti, “Bond-orientational order in liquids and glasses,” *Phys. Rev. B*, vol. 28, pp. 784–805, 2 Jul. 1983. DOI: 10.1103/PhysRevB.28.784. [Online]. Available: https://link.aps.org/doi/10.1103/PhysRevB.28.784.

[84] W. Mickel, S. C. Kapfer, G. E. Schröder-Turk, and K. Mecke, “Shortcomings of the bond orientational order parameters for the analysis of disordered particulate matter,” *The Journal of Chemical Physics*, vol. 138, no. 4, Jan. 2013. DOI: 10.1063/1.4774084.

[85] H. Eslami, P. Sedaghat, and F. Müller-Plathe, “Local bond order parameters for accurate determination of crystal structures in two and three dimensions,” *Phys. Chem. Chem. Phys.*, vol. 20, pp. 27 059–27 068, 42 2018. DOI: 10.1039/C8CP05248D.

[86] W. Lechner and C. Dellago, “Accurate determination of crystal structures based on averaged local bond order parameters,” *The Journal of chemical physics*, vol. 129, p. 114 707, Oct. 2008. DOI: 10.1063/1.2977970.

[87] L. Filion, M. Hermes, R. Ni, and M. Dijkstra, “Crystal nucleation of hard spheres using molecular dynamics, umbrella sampling, and forward flux sampling: A comparison of simulation techniques,” *The Journal of Chemical Physics*, vol. 133, no. 24, Dec. 2010. DOI: 10.1063/1.3506838.

[88] A. Radhi and K. Behdinan, “Identification of crystal structures in atomistic simulation by predominant common neighborhood analysis,” *Computational Materials Science*, vol. 126, pp. 182–190, 2017, ISSN: 0927-0256. DOI: 10.1016/j.commatsci.2016.09.035.

[89] H. Doi, K. Z. Takahashi, and T. Aoyagi, “Mining of effective local order parameters for classifying crystal structures: A machine learning study,” *The Journal of Chemical Physics*, vol. 152, no. 21, Jun. 2020. DOI: 10.1063/5.0005228.

[90] K. Z. Takahashi, “Molecular cluster analysis using local order parameters selected by machine learning,” *Phys. Chem. Chem. Phys.*, vol. 25, pp. 658–672, 1 2023. DOI: 10.1039/D2CP03696G.

[91] A. Radhi, V. Iacobellis, and K. Behdinan, “Parametric crystalline characterization of anatase/rutile polymorphic ceramic,” *Applied Physics A*, vol. 129, Mar. 2023. DOI: 10.1007/s00339-023-06562-9.

[92] L. Gránásy, T. Wang, and P. F. James, “Kinetics of wollastonite nucleation in cao□sio2 glass,” *The Journal of Chemical Physics*, vol. 108, no. 17, pp. 7317–7326, 1998. DOI: 10.1063/1.476150.

[93] E. Mazzucato and A. F. Gualtieri, “Wollastonite polytypes in the cao-sio2 system.,” *Physics and Chemistry of Minerals*, vol. 27, no. 8, pp. 565–574, Sep. 2000, ISSN: 1432-2021. DOI: 10.1007/s002690000095.

[94] J. Taylor and A. Dinsdale, “Thermodynamic and phase diagram data for the cao-sio2 system,” *Calphad*, vol. 14, no. 1, pp. 71–88, 1990, ISSN: 0364-5916. DOI: 10.1016/0364-5916(90)90041-W.

[95] G. W. Morey, *Data of Geochemistry. Chapter L. Phase-Equilibrium Relations of the Common Rock-Forming Oxides Except Water*, Sixth Edition. United States government printing office, Washington, 1964. DOI: 10.1021/ja00949a073.

[96] A. P. Thompson *et al.*, “LAMMPS - a flexible simulation tool for particle-based materials modeling at the atomic, meso, and continuum scales,” *Comp. Phys. Comm.*, vol. 271, p. 108 171, 2022. DOI: 10.1016/j.cpc.2021.108171.

[97] M. J. Buerger and C. T. Prewitt, “The crystal structures of wollastonite and pectolite,” *Proceedings of the National Academy of Sciences*, vol. 47, no. 12, pp. 1884–1888, 1961. DOI: 10.1073/pnas.47.12.1884.

[98] V. Swamy, L. S. Dubrovinsky, and F. Tutti, “High-temperature raman spectra and thermal expansion of wollastonite,” *Journal of the American Ceramic Society*, vol. 80, no. 9, pp. 2237–2247, 1997. DOI: https://doi-org.tudelft.idm.oclc.org/10.1111/j.1151-2916.1997.tb03113.x.

Determination of crystal structure

X-RAY FACILITIES GROUP

Dr. Amarante Böttger *A.J.Bottger@tudelft.nl*
phone +31(0)1527·82243
Dhr. Ruud Hendrikx *R.W.A.Hendrikx@tudelft.nl*
Drs. Richard Huizenga *R.M.Huizenga@tudelft.nl*

Delft University of Technology, Faculty of 3mE
Department of Materials Science and Engineering
Mekelweg 2, NL-2628 CD Delft, the Netherlands, phone +31(0)1527·82255/89459

XRD study of glass samples

Author	:	Ruud Hendrikx
Date	:	03 nov 2022
Researcher	:	Wouter Nederstigt, Maana Electric
Research question	:	Phase identification

Samples
"Het zijn 3 samples, van glas in verschillende state van kristallisatie. Ik ben dan vooral geinteresseerd in de structuur van het kristal, welke kristalfase als eerste vormt."

Specimen
As can be seen in bottom picture in figure 1, of sample "Wadi" the smooth and shiny flat surface is measured. Parts of the other two samples were powdered in with pestle and mortar. The powders were deposited as a thin layer on a Si510 zero-background wafer.

Experimental
Instrument: Bruker D8 Advance diffractometer Bragg-Brentano geometry and Lynxeye position sensitive detector. Cu Kα radiation. Divergence slit V12, scatter screen height 5 mm, 45 kV 40 mA. Sample spinning. Detector settings LL 0.11 W 0.14.

Measurements
Coupled θ -2θ scan 5° - 110°, step size 0.030 ° 2θ, counting time per step 1 s.

Data evaluation
Bruker software DiffracSuite.EVA vs 6.0

Results
Figures 2 - 4 show the measured XRD patterns in black, after background subtraction and small displacement correction. The colored sticks give the peak positions and intensities of the possibly present crystalline phases, using the ICDD pdf4 database, see table 1. Some small peaks could not be identified.

sample	*compound*	
Yellow	Wollastonite-1A, Fe+2-bearing	(Ca2.87Fe0.13)(SiO3)3
Chunk	Wollastonite-1A, Fe+2-bearing	(Ca2.87Fe0.13)(SiO3)3
	Augite	Ca(Mg,Fe)Si2O6
	Anorthite, Na-bearing	(Ca2.133Na1.867)(Si10.003Al5.987)O32
Wadi	amorphous	

Table 1.

If the analysis is a significant part of a publication, a co-authorship is preferred.

In any case, it is useful to involve us in the preparation of any presentation to ensure optimum and correct use of the analysis results!

Whenever used in a publication, an acknowledgement will be appreciated, e.g.: "personX at the Department of Materials Science and Engineering of the Delft University of Technology is acknowledged for the X-ray analysis".

Figures

sample "Yellow"

sample "Crunch"

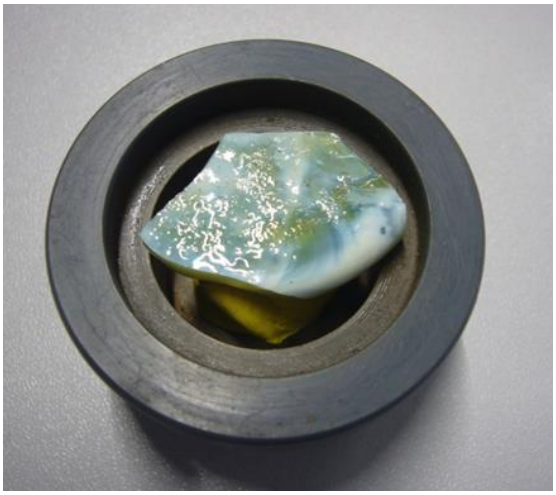

sample "Wadi" in sample holder

Figure 1 samples

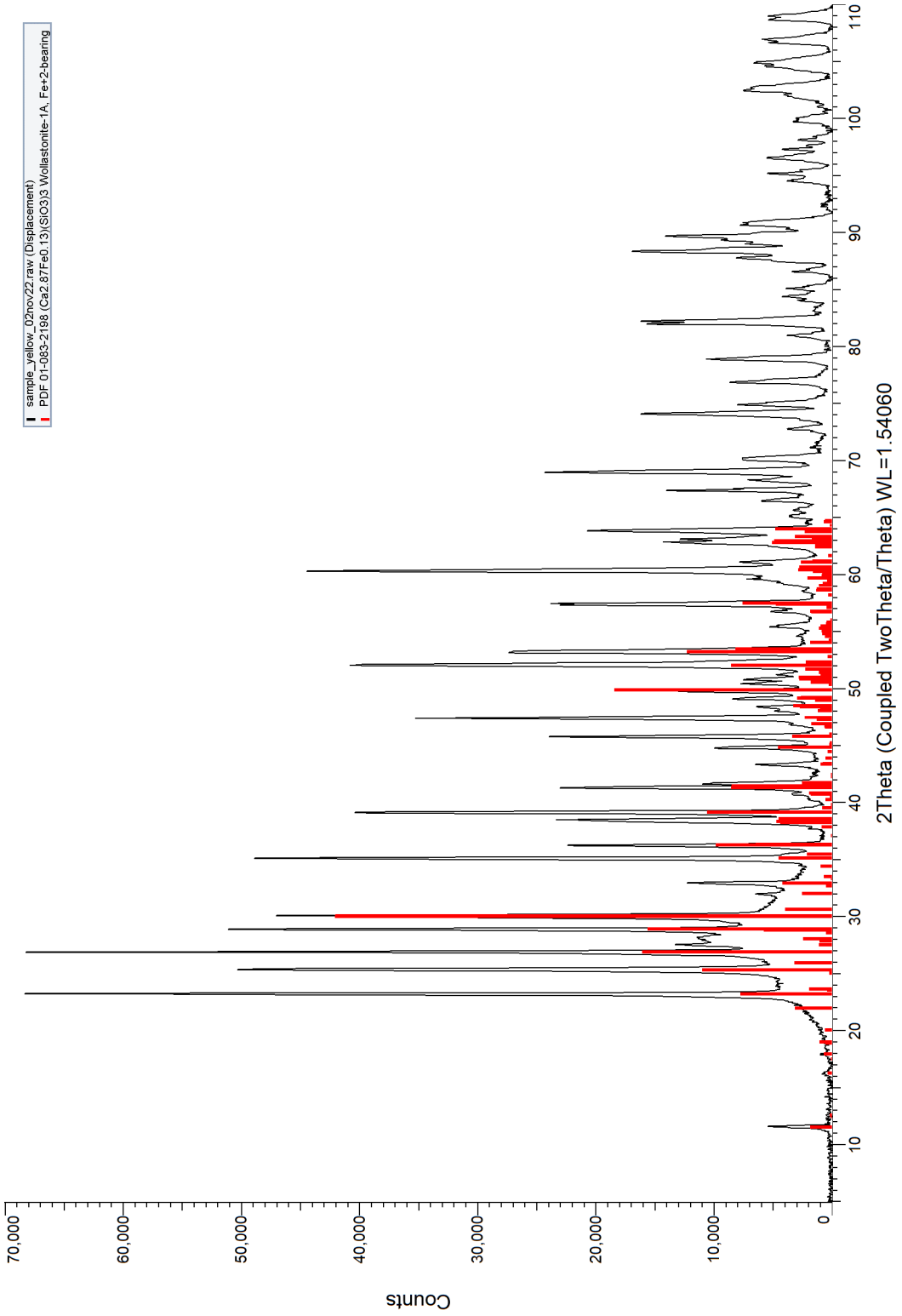

Figure 2 XRD pattern sample " Yellow "

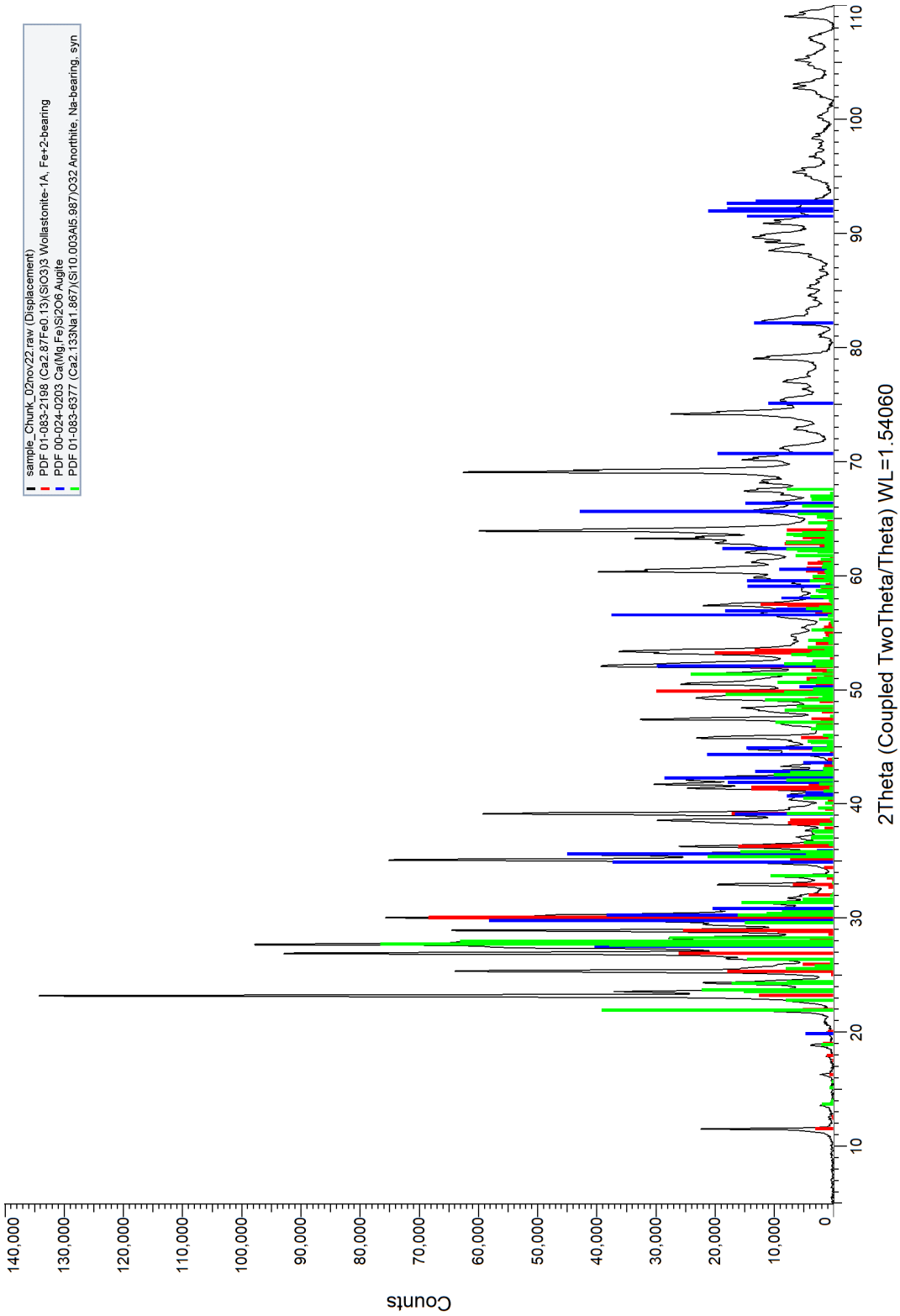

Figure 3 XRD pattern sample "Chunk "

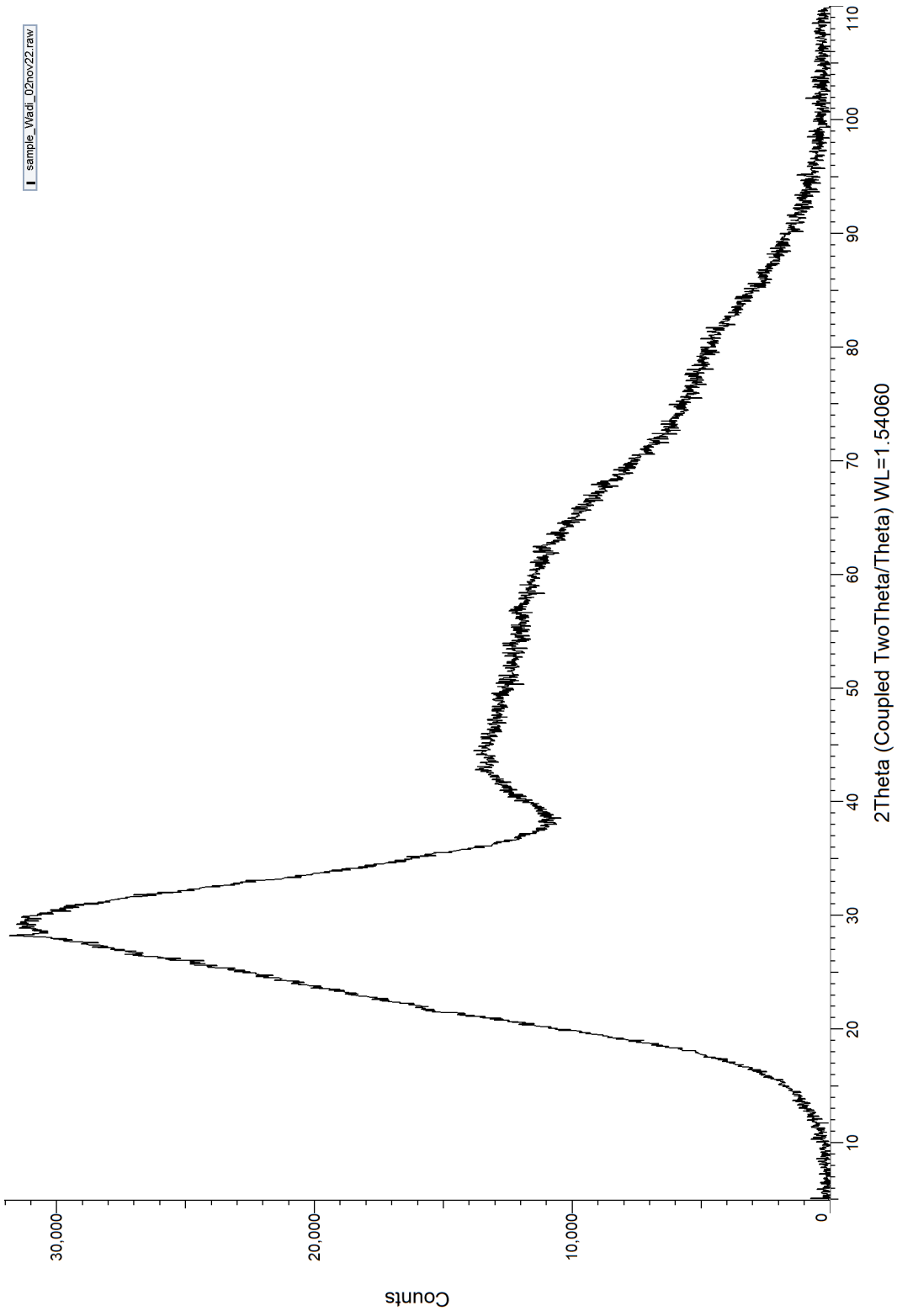

Figure 4 XRD pattern sample "Wadi "

Determination of composition

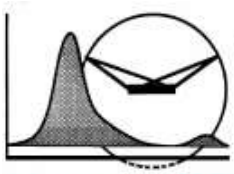

Materials Science and Engineering
TUDelft, Faculty of 3mE
Mekelweg 2
2628 CD Delft, The Netherlands
Tel:015-2789459
Email: R.W.A.Hendrikx@tudelft.nl

X- ray diffraction facilities

Experimental conditions:

For XRF analysis the measurements were performed with a Panalytical Axios Max WD-XRF spectrometer and data evaluation was done with SuperQ5.0i/Omnian software. 18/12/2015 09:37:03

3/17/2023 3:46:12 PM

PANalytical

Quantification of sample W. Nederstigt, sample "GPS 17mar23

Sum before normalization: 100.5 wt%

Normalised to: 100.0 wt%

Sample type: Solid

Correction applied for medium: No

Correction applied for film: No

Used Compound list: Oxides

Results database: omnian 4kw 20mm

Results database in: c:\panalytical\superq\userdata

	Compound Name	Conc. (wt%)	Absolute Error (wt%)
1	SiO2	56.121	0.1
2	CaO	33.139	0.1
3	Al2O3	4.839	0.06
4	MgO	2.308	0.05
5	Fe2O3	1.329	0.03
6	K2O	0.909	0.03
7	Na2O	0.894	0.03
8	TiO2	0.145	0.01
9	SrO	0.07	0.008
10	P2O5	0.061	0.007
11	Cr2O3	0.046	0.006
12	MnO	0.036	0.006
13	BaO	0.025	0.005
14	SO3	0.025	0.005
15	ZrO2	0.019	0.004
16	NiO	0.019	0.004
17	Cl	0.014	0.004
18	Rb2O	0.002	0.001

Use of our XRD or XRF analysis:
In a publication: 'PersonX at the Department of Materials Science and Engineering of the Delft University of Technology is acknowledged for the X-ray analysis. If it is an important part of the publication: a co-authorship is preferred. It is useful to involve us in the preparation of any presentation!

Results of the simulations

Investigation into the critical temperature of a 1.9nm nucleus

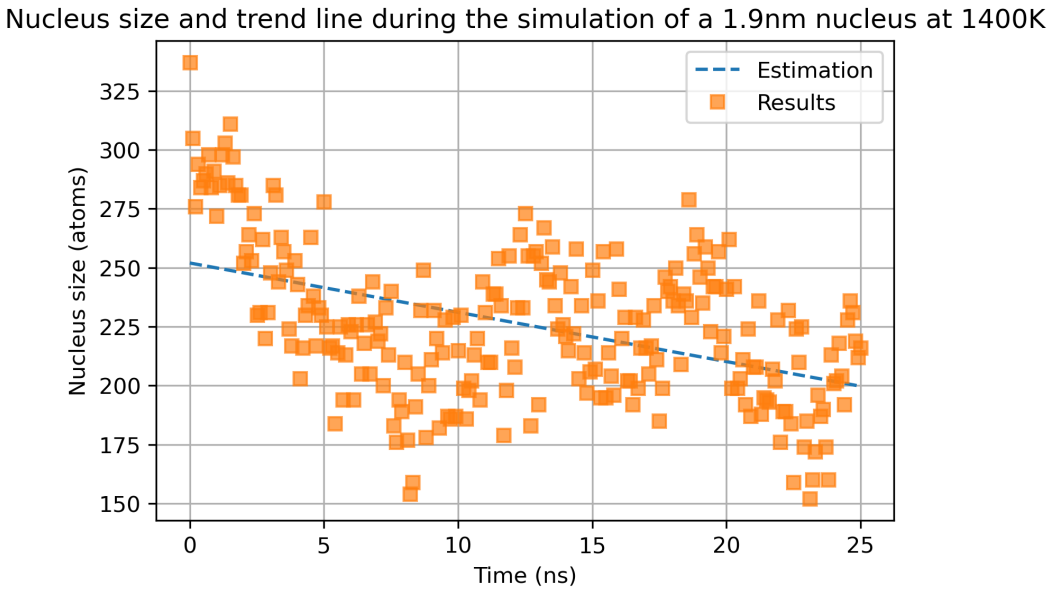

Figure 1: A scatterplot of all the sampled nucleus sizes during the simulation of an inserted nucleus of 1.9nm at 1400K.

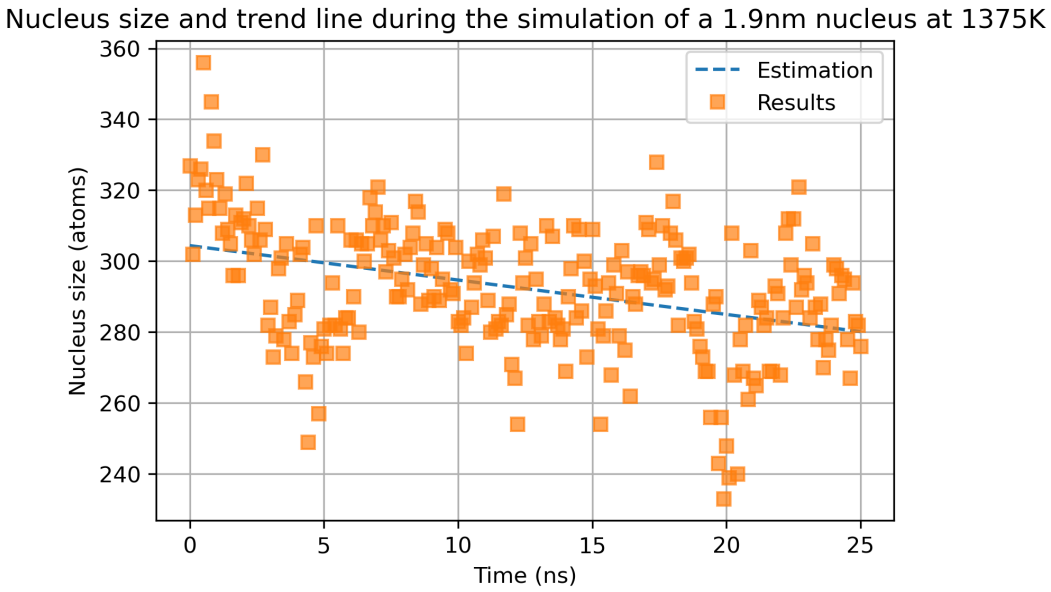

Figure 2: A scatterplot of all the sampled nucleus sizes during the simulation of an inserted nucleus of 1.9nm at 1375K.

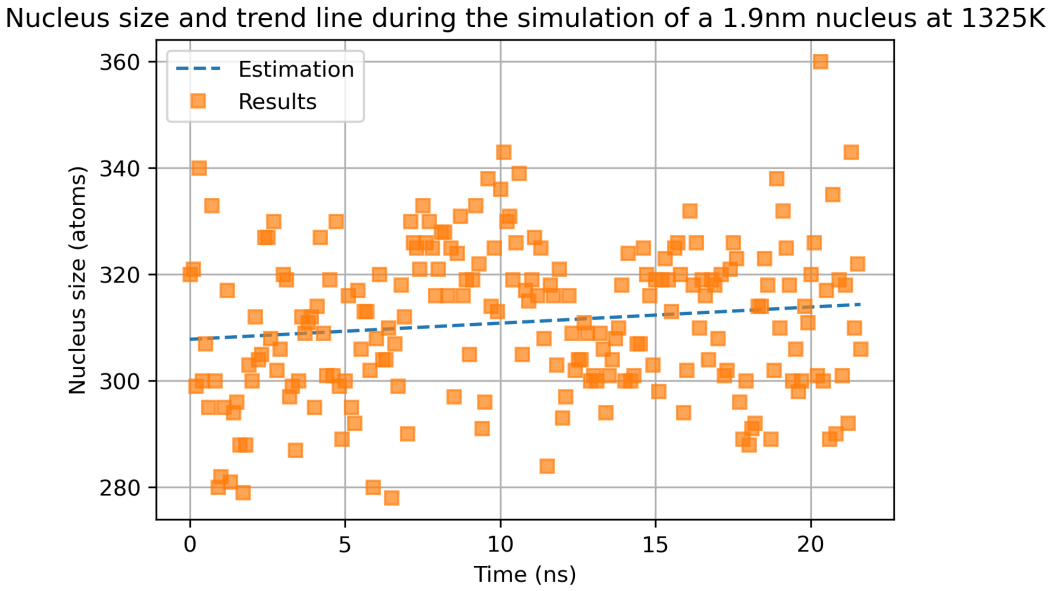

Figure 3: A scatterplot of all the sampled nucleus sizes during the simulation of an inserted nucleus of 1.9nm at 1325K.

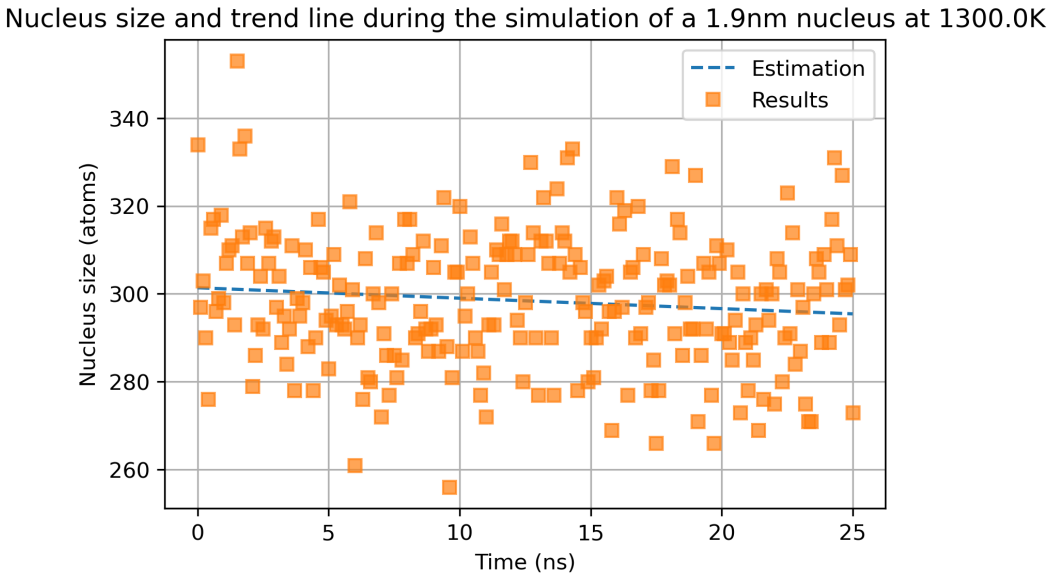

Figure 4: A scatterplot of all the sampled nucleus sizes during the simulation of an inserted nucleus of 1.9nm at 1300K.

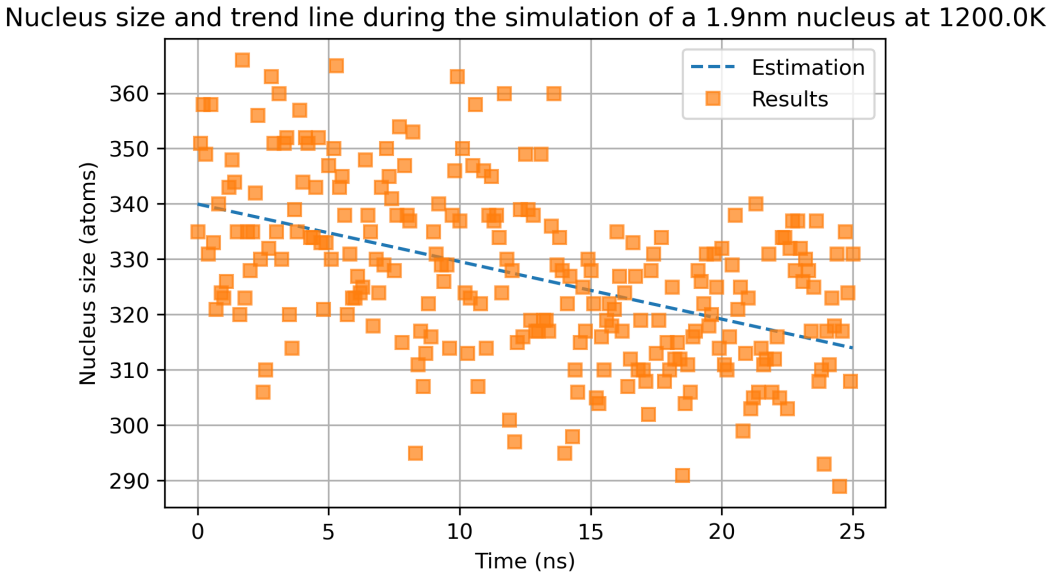

Figure 5: A scatterplot of all the sampled nucleus sizes during the simulation of an inserted nucleus of 1.9nm at 1200K.

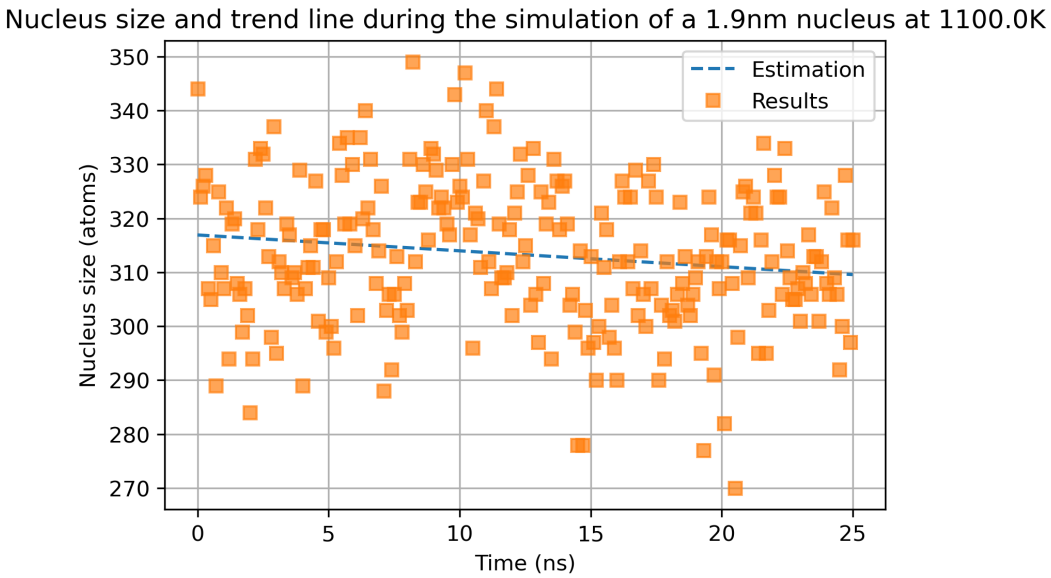

Figure 6: A scatterplot of all the sampled nucleus sizes during the simulation of an inserted nucleus of 1.9nm at 1100K.

Investigation into the critical temperature of a 1.6nm nucleus

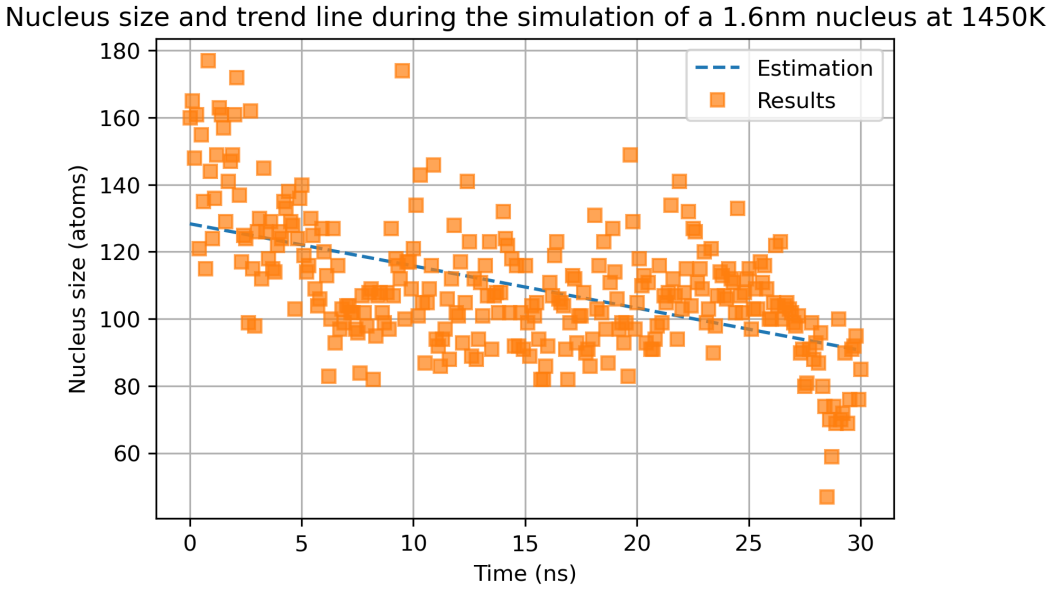

Figure 7: A scatterplot of all the sampled nucleus sizes during the simulation of an inserted nucleus of 1.6nm at 1450K.

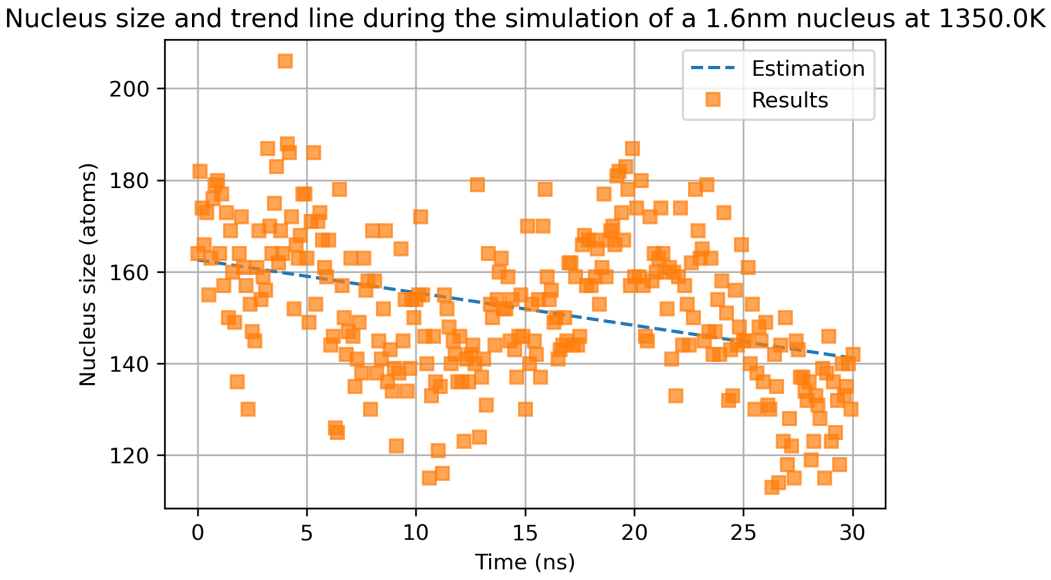

Figure 8: A scatterplot of all the sampled nucleus sizes during the simulation of an inserted nucleus of 1.6nm at 1350K.

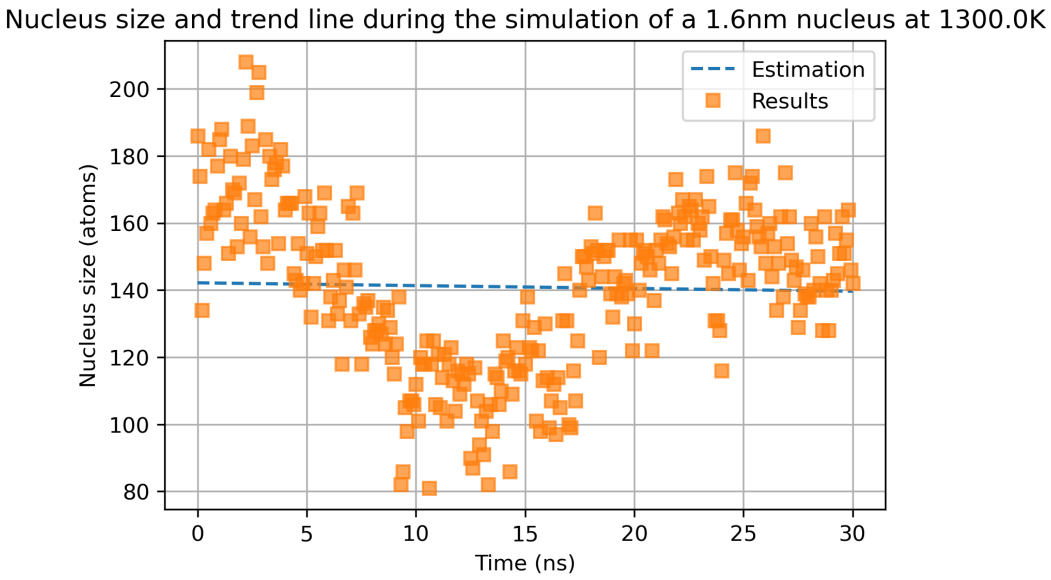

Figure 9: A scatterplot of all the sampled nucleus sizes during the simulation of an inserted nucleus of 1.6nm at 1300K.

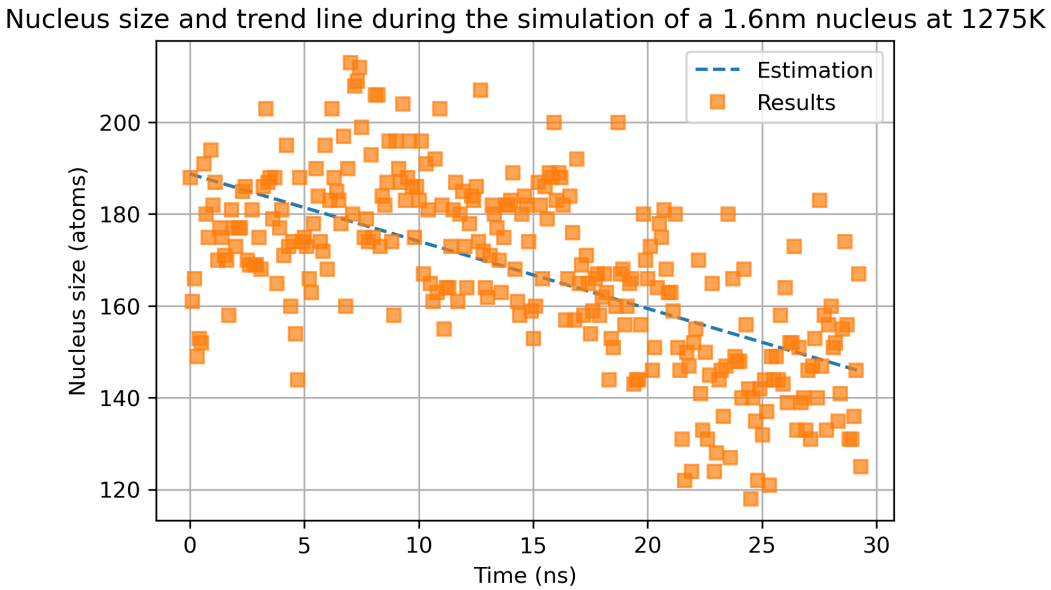

Figure 10: A scatterplot of all the sampled nucleus sizes during the simulation of an inserted nucleus of 1.6nm at 1275K.

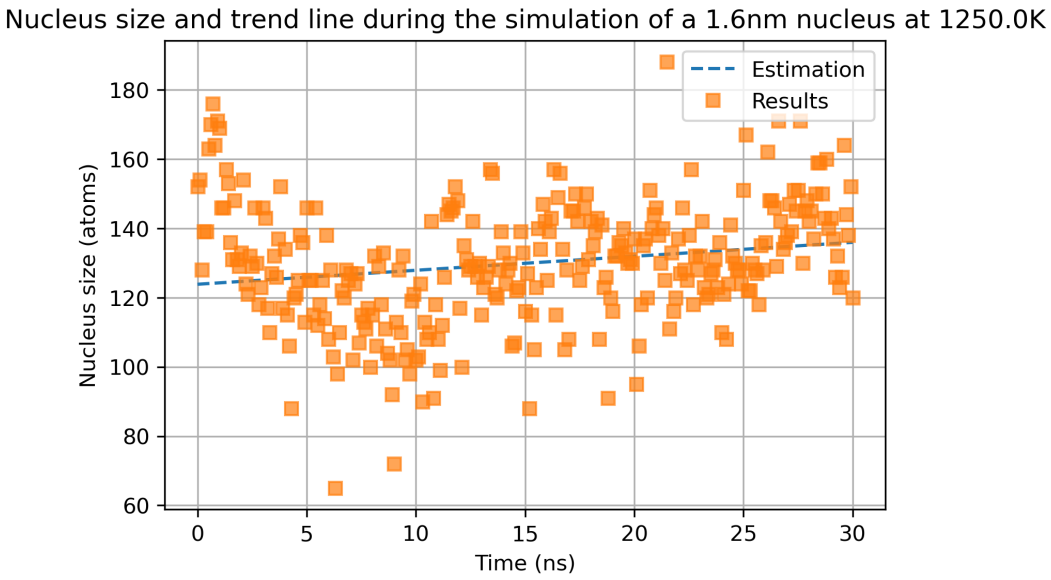

Figure 11: A scatterplot of all the sampled nucleus sizes during the simulation of an inserted nucleus of 1.6nm at 1250K.

Investigation into the critical temperature of a 1.3nm nucleus

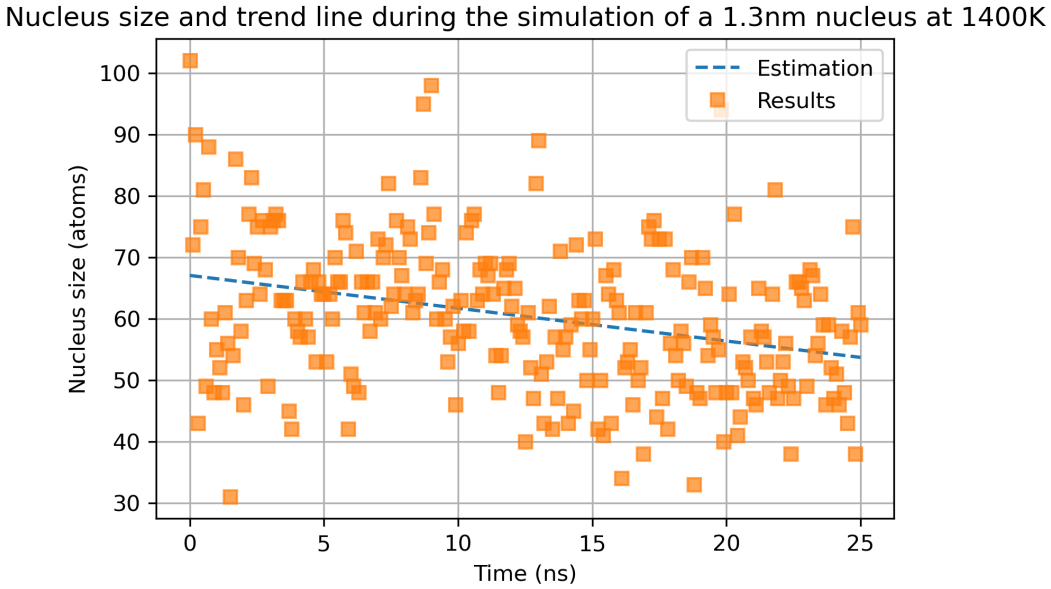

Figure 12: A scatterplot of all the sampled nucleus sizes during the simulation of an inserted nucleus of 1.3nm at 1400K.

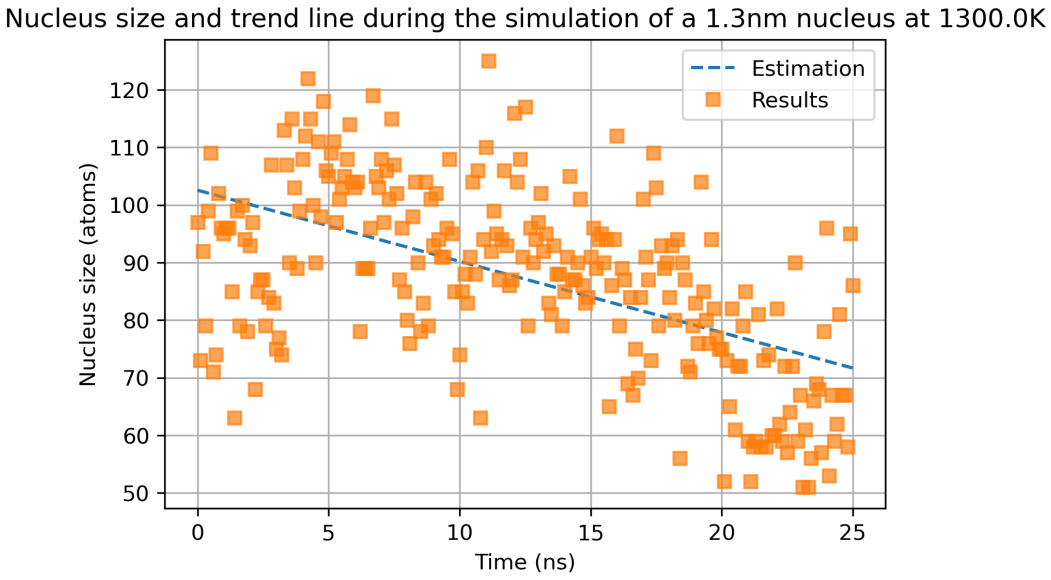

Figure 13: A scatterplot of all the sampled nucleus sizes during the simulation of an inserted nucleus of 1.3nm at 1300K.

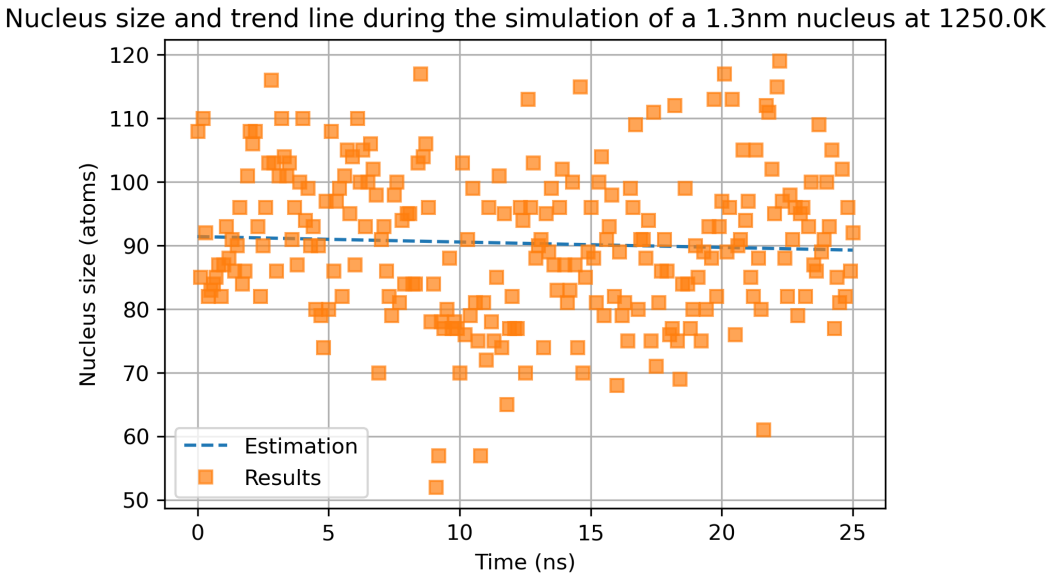

Figure 14: A scatterplot of all the sampled nucleus sizes during the simulation of an inserted nucleus of 1.3nm at 1250K.

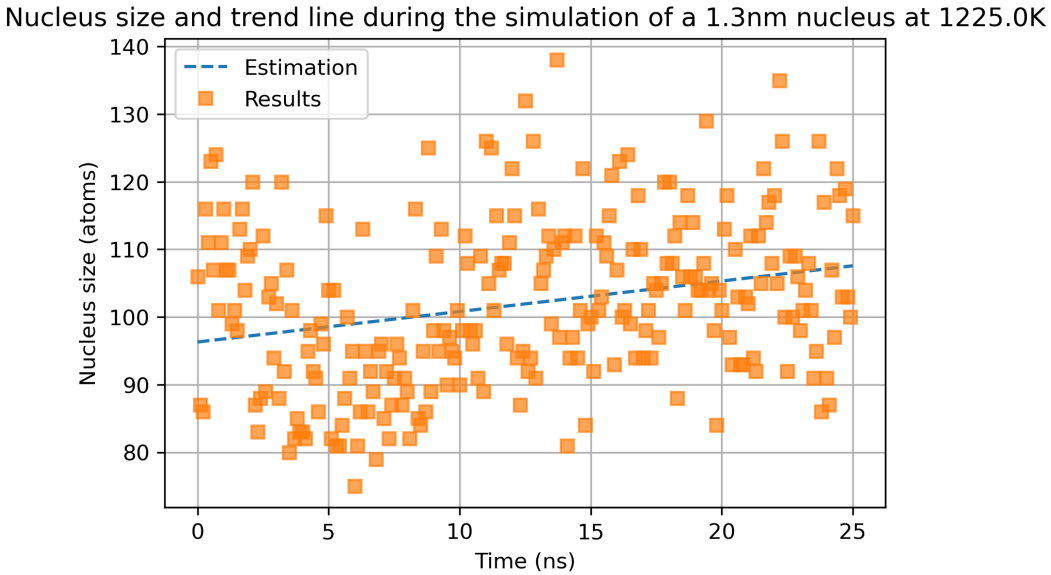

Figure 15: A scatterplot of all the sampled nucleus sizes during the simulation of an inserted nucleus of 1.3nm at 1225K.

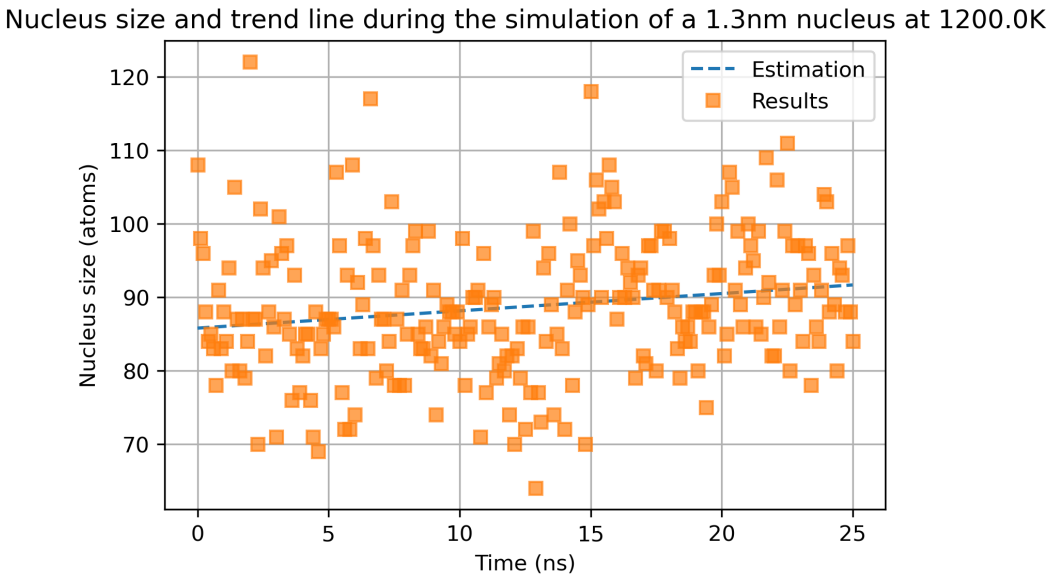

Figure 16: A scatterplot of all the sampled nucleus sizes during the simulation of an inserted nucleus of 1.3nm at 1200K.

Investigation into the critical temperature of a 1.1nm nucleus

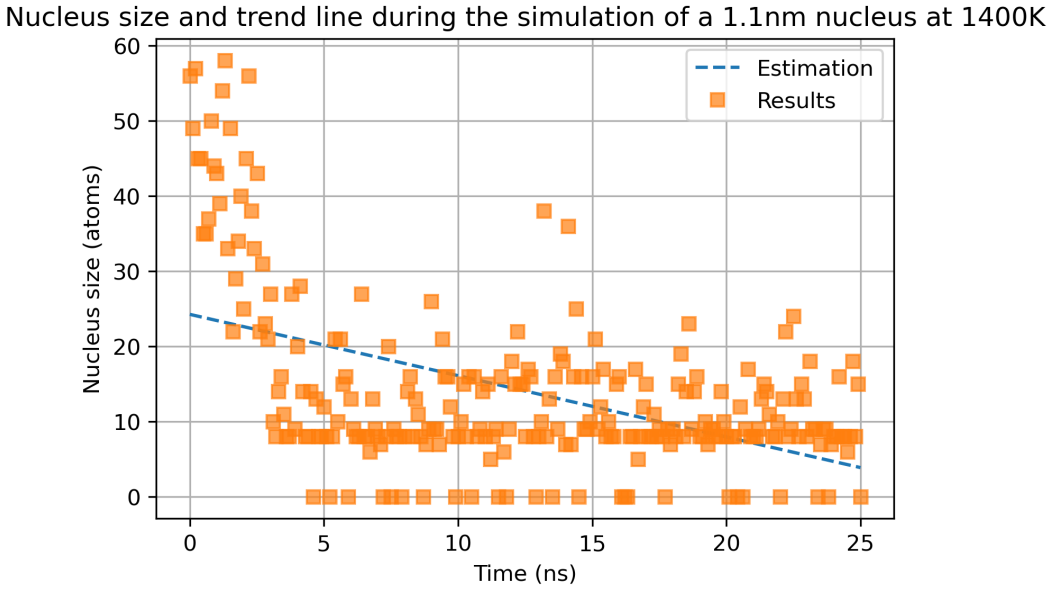

Figure 17: A scatterplot of all the sampled nucleus sizes during the simulation of an inserted nucleus of 1.1nm at 1400K.

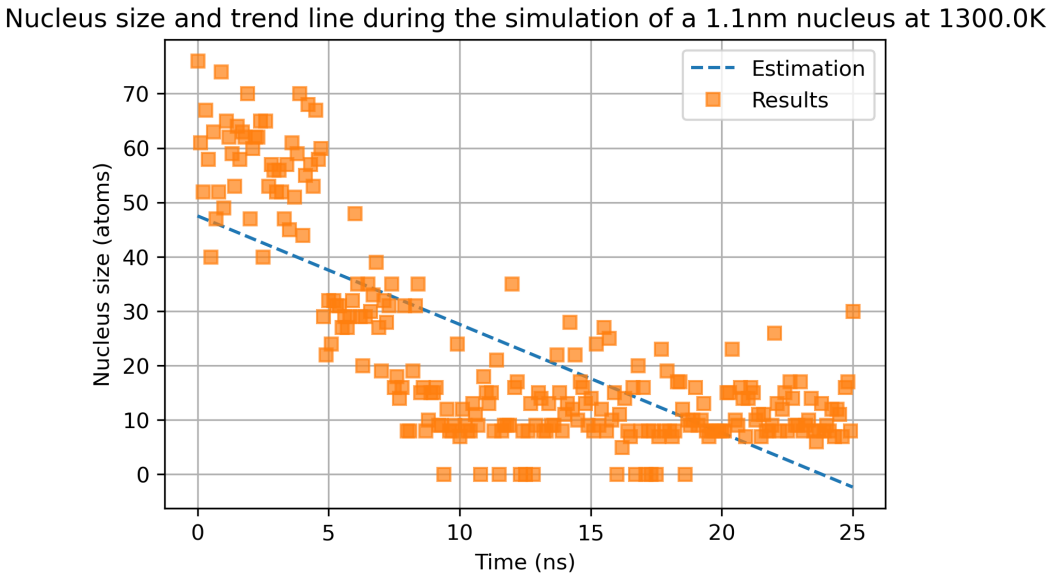

Figure 18: A scatterplot of all the sampled nucleus sizes during the simulation of an inserted nucleus of 1.1nm at 1300K.

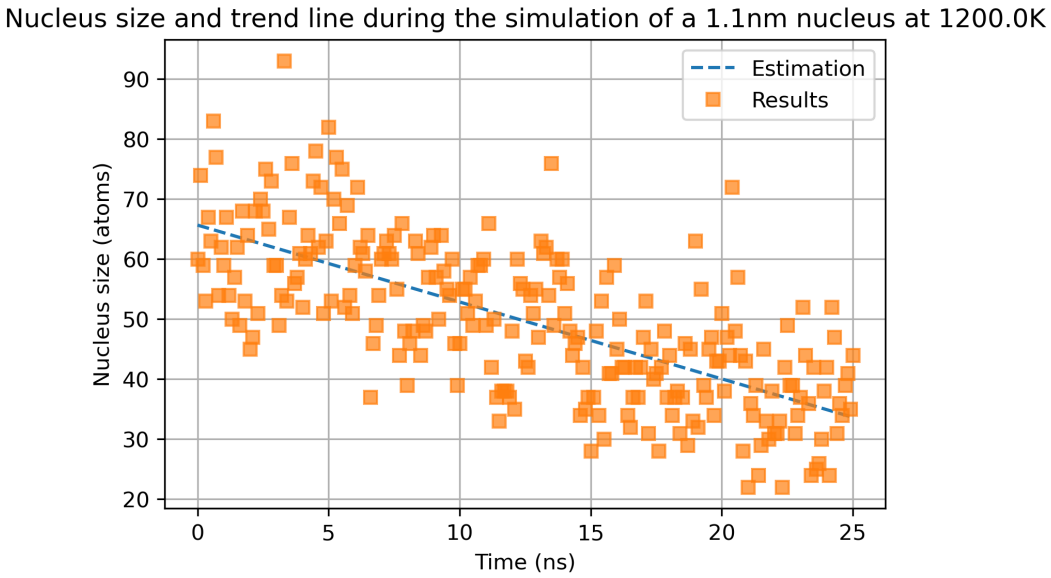

Figure 19: A scatterplot of all the sampled nucleus sizes during the simulation of an inserted nucleus of 1.1nm at 1200K.

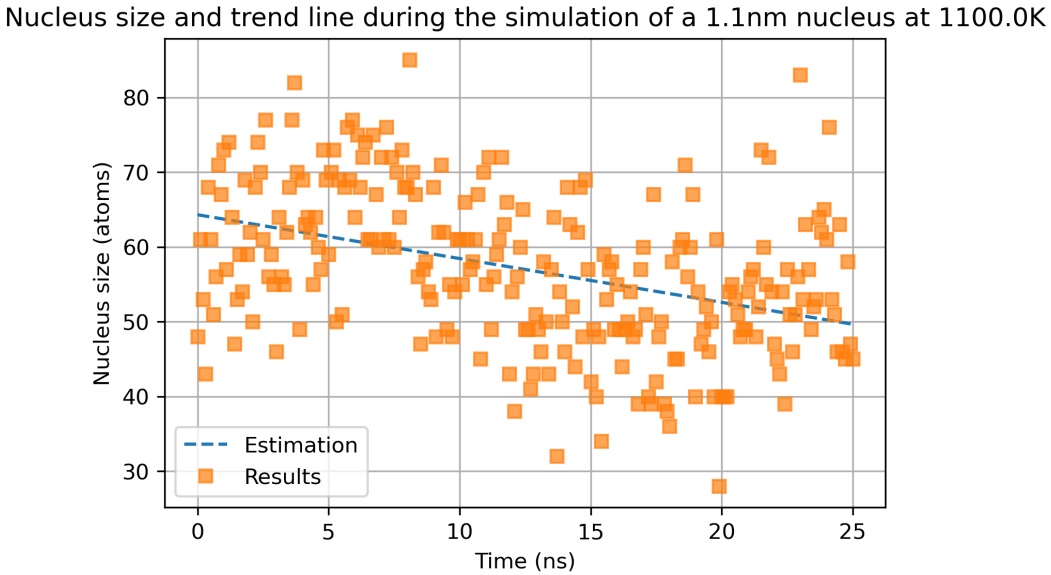

Figure 20: A scatterplot of all the sampled nucleus sizes during the simulation of an inserted nucleus of 1.1nm at 1100K.

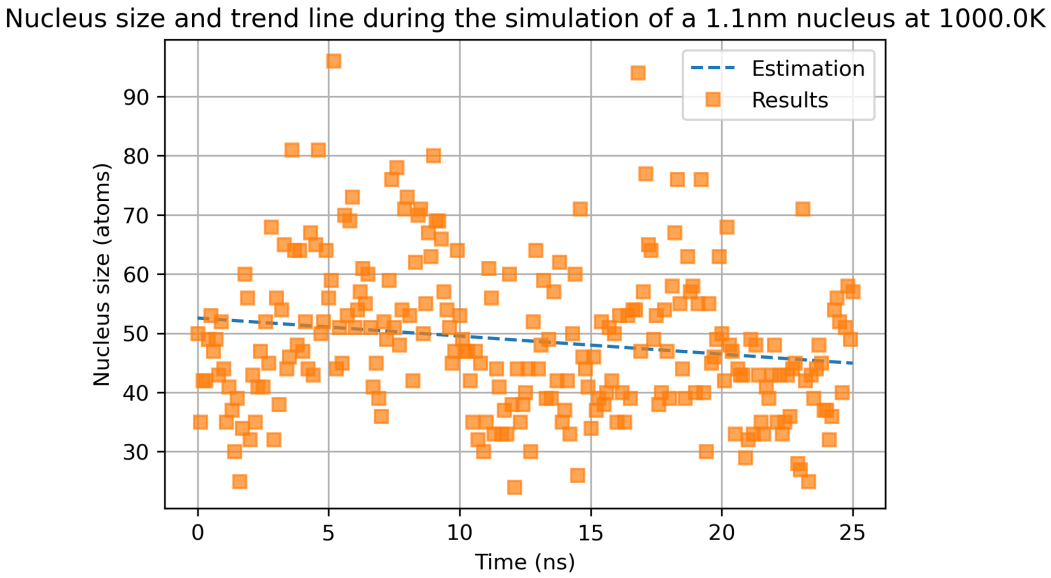

Figure 21: A scatterplot of all the sampled nucleus sizes during the simulation of an inserted nucleus of 1.1nm at 1000K.

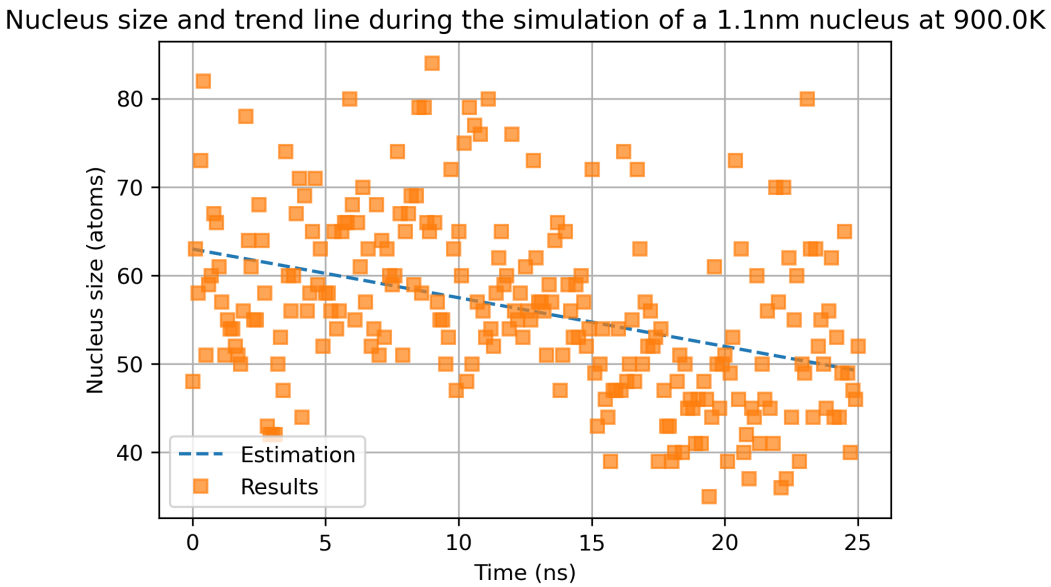

Figure 22: A scatterplot of all the sampled nucleus sizes during the simulation of an inserted nucleus of 1.1nm at 900K.